

DOCTORAL THESIS

Crustal structure of the Eratosthenes
Seamount, Cyprus and S. Turkey from an
amphibian wide-angle seismic profile

Author:

M.Sc. Christian FELD

Supervisor:

Prof. Dr. Michael WEBER

Dr. James MECHIE

Dissertation submitted to the Faculty of Mathematics and Natural Sciences at
the

University of Potsdam, Germany

to acquire the academic degree of

Doctor of Natural Sciences (Dr. rer. nat.)

in Geophysics

Potsdam,

October 24, 2014

Advisor / Reviewer 1
Prof. Dr. Michael Weber, Universität Potsdam

Reviewer 2
Prof. Dr. Magdalena Scheck-Wenderoth, RWTH Aachen

Reviewer 3
Prof. Dr. Wilfried Jokat, Universität Bremen

The study was funded by the Deutsches GeoForschungsZentrum - GFZ and the DFG.

Written by Christian Feld

Published online at the
Institutional Repository of the University of Potsdam:
URN urn:nbn:de:kobv:517-opus4-73479
<http://nbn-resolving.de/urn:nbn:de:kobv:517-opus4-73479>

Danksagung

An dieser Stelle möchte ich mich bei all denjenigen bedanken, die mich während der Promotionsphase und bei der Anfertigung dieser Dissertation unterstützt und geholfen haben.

Mein besonderer Danke gilt Jim Mechie für die außerordentlich gute Betreuung während der gesamten Promotionsphase, für die zahlreichen, stets hilfreichen und konstruktiven Tipps, Ideen und Diskussionen. Ich bedanke mich für die Unterstützung sowohl bei inhaltlichen als auch organisatorischen Dingen rund um die Promotion und für das zügige Korrekturlesen. Ich bedanke mich außerdem bei meinem Betreuer Prof. Michael Weber für die Möglichkeit diese Studie als Doktorand am GFZ durchzuführen und bearbeiten zu können und die Ergebnisse auf der AGU 2013 und anderen Konferenzen vorstellen zu dürfen. Ich bedanke mich für den stetigen Einsatz als Sektionsleiter und für die guten Arbeitsbedingungen in der Sektion.

Ich bedanke mich bei allen Teilnehmern der Expedition in die Türkei und Zypern für die Datenerhebung und den Kollegen der Schiffsexpedition MSM 14/3. Ich bedanke mich bei dem Geophysikalischen Gerätepool Potsdam (GIPP) für die Bereitstellung der Instrumente.

Ich möchte mich bei Klaus Bauer für die Anregung und Unterstützung bei der Erstellung der Line-Drawing Migration bedanken, die wertvolle Inhalte zu den Ergebnissen dieser Arbeit beigetragen haben.

Ich bedanke mich bei Anke Lerch für die Unterstützung rund um organisatorische Angelegenheiten und für das stetige Versorgen mit Büromaterialien.

Ich möchte mich außerdem bei den IT Administratoren Christof Lendl und Matthias Wanjek und für deren Unterstützung bei PC Problemen jeglicher Art bedanken.

Ich bedanke mich bei der gesamten Sektion 2.2 für die Unterstützung, konstruktive Diskussionen, Ideen, Anregungen und für die tolle Zeit.

Für die persönliche Unterstützung und Motivation während der Promotionszeit möchte mich auch bei meinen Eltern und Geschwistern bedanken.

Ein besonderes und ganz herzliches Dankeschön geht an Michèle Ickrath für das ständige Verständnis, für die moralische als auch fachliche Hilfe, für die vielen und hilfreichen Tipps, für das Zuhören und Diskutieren und natürlich auch für das Korrekturlesen.

Abstract

Crustal structure of the Eratosthenes Seamount, Cyprus and S. Turkey from an amphibian wide-angle seismic profile

by M.Sc. Christian FELD

In March 2010, the project CoCoCo (incipient COntinent-COntinent COLLision) recorded a 650 *km* long amphibian N-S wide-angle seismic profile, extending from the Eratosthenes Seamount (ESM) across Cyprus and southern Turkey to the Anatolian plateau. The aim of the project is to reveal the impact of the transition from subduction to continent-continent collision of the African plate with the Cyprus-Anatolian plate. A visual quality check, frequency analysis and filtering were applied to the seismic data and reveal a good data quality. Subsequent first break picking, finite-differences ray tracing and inversion of the offshore wide-angle data leads to a first-arrival tomographic model. This model reveals (1) P-wave velocities lower than 6.5 *km/s* in the crust, (2) a variable crustal thickness of about 28 – 37 *km* and (3) an upper crustal reflection at 5 *km* depth beneath the ESM. Two land shots on Turkey, also recorded on Cyprus, airgun shots south of Cyprus and geological and previous seismic investigations provide the information to derive a layered velocity model beneath the Anatolian plateau and for the ophiolite complex on Cyprus. The analysis of the reflections provides evidence for a north-dipping plate subducting beneath Cyprus. The main features of this layered velocity model are (1) an upper and lower crust with large lateral changes of the velocity structure and thickness, (2) a Moho depth of about 38 – 45 *km* beneath the Anatolian plateau, (3) a shallow north-dipping subducting plate below Cyprus with an increasing dip and (4) a typical ophiolite sequence on Cyprus with a total thickness of about 12 *km*. The offshore-onshore seismic data complete and improve the information about the velocity structure beneath Cyprus and the deeper part of the offshore tomographic model. Thus, the wide-angle seismic data provide detailed insights into the 2-D geometry and velocity structures of the uplifted and overriding Cyprus-Anatolian plate. Subsequent gravity modelling confirms and extends the crustal P-wave velocity model. The deeper part of the subducting plate is constrained by the gravity data and has a dip angle of $\sim 28^\circ$. Finally, an integrated analysis of the geophysical and geological information allows a comprehensive interpretation of the crustal structure related to the collision process.

Zusammenfassung

Die Krustenstruktur von dem Eratosthenes Seeberg, Zypern und der Süd-Türkei anhand eines amphibischen seismischen Weitwinkel Profils

von M.Sc. Christian FELD

Im März 2010 wurden im Rahmen des "CoCoCo"-Projektes ein 650km langes amphibisches, seismisches Weitwinkel Profil aufgenommen. Dieses erstreckte sich von dem Eratosthenes Seeberg (ESM) über Zypern und der Süd-Türkei bis zum anatolischen Plateau. Das Hauptziel des Projektes ist es, den Einfluss zu untersuchen, der von dem Übergang eines Subduktion Prozesses hin zu einer Kontinent-Kontinent Kollision der afrikanischen Platte mit der zyprisch-anatolischen Platte hervorgerufen wird. Die seismischen Daten wurden einer visuellen Qualitätsüberprüfung, Frequenz-Analyse und Filterung unterzogen und zeigten eine gute Qualität. Das darauf folgende Picken der Ersteinströme, eine Finite-Differenzen Raytracing und eine Inversion der offshore Weitwinkel Daten, führte zu einem Laufzeit Tomographie Modell. Das Modell zeigt (1) P-Wellengeschwindigkeiten kleiner als 6.5 km/s in der Kruste, (2) eine variable Krustenmächtigkeit von $28 - 37 \text{ km}$ und (3) eine obere Krustenreflektion in 5 km Tiefe unter dem ESM. Zwei Landschüsse in der Türkei, ebenfalls aufgenommen auf Zypern, Luftkanonen-Schüsse südlich von Zypern und vorausgegangene geologische und seismische Untersuchungen lieferten die Grundlage, um ein geschichtetes Geschwindigkeitsmodell für das anatolische Plateau und für den Ophiolith-Komplex auf Zypern abzuleiten. Die Analyse der Reflexionen liefern den Beweis für eine nach Norden einfallende Platte welche unter Zypern subduziert. Die Hauptkennzeichen dieses geschichteten Geschwindigkeitsmodelles sind (1) eine obere und untere Kruste mit starken lateralen Änderungen in Geschwindigkeit und Mächtigkeit, (2) eine Mohotiefe in $38 - 45 \text{ km}$ unter dem anatolischen Plateau, (3) eine flach nach Norden einfallende Platte unter Zypern mit ansteigendem Einfallswinkel und (4) eine typische Ophiolith Sequenz auf Zypern mit einer Gesamtmächtigkeit von 12 km . Die seismischen offshore / onshore Daten komplettieren und verbessern die bisherigen Kenntnisse über die Geschwindigkeitsstruktur unter Zypern und des tieferen Bereiches der offshore Tomographie. Damit liefert die Weitwinkel Seismik detaillierte Einblicke in die 2-D Geometrie und die Geschwindigkeitsstrukturen der angehobenen und überlagerten zyprisch-anatolischen Platte. Die darauf folgende Gravimetrie Modellierung bestätigt und erweitert das P-Wellen Krusten-Geschwindigkeits Modell. Der tiefere Teil der subduzierten Platte, welche einen Einfallswinkel von $\sim 28^\circ$ hat, wurde durch die Gravimetrie Daten belegt. Letztlich erlaubt eine ganzheitliche Analyse von geophysikalischen und geologischen Informationen die umfassende Interpretation der Krustenstruktur welche in Verbindung mit dem Kollisions Prozess steht.

Contents

Danksagung	iii
Abstract	iv
Zusammenfassung	v
Table of Contents	v
List of Figures	viii
List of Tables	x
Abbreviations	xi
1 Introduction	1
1.1 Eastern Mediterranean	1
1.2 Project Objectives and Motivation	5
1.3 Tectonics and Geology	8
2 Methods	20
2.1 Introduction to Seismic Waves	20
2.2 Model Parameterization	24
2.3 Forward Modelling	27
2.4 Traveltime Tomography / Inversion	30
2.5 Synthetic Seismogram Computation	34
3 Seismic Data and Processing	37
3.1 Data Acquisition	37
3.2 Data Preparation and Processing	41
3.3 Traveltime Picking	44
3.4 Data Examples	46
4 Crustal Modelling and Results	52
4.1 Tomographic Velocity Model	53
4.1.1 1-D start model	53
4.1.2 Development of the tomographic model	54
4.1.3 Development of the velocity model beneath Cyprus	56

4.1.4	Results	59
4.1.5	Checkerboard Tests	62
4.1.6	Picked vs. calculated traveltimes	65
4.1.7	Discussion	66
4.2	Layered Velocity Model	70
4.2.1	Results	71
4.2.2	Picked vs. calculated traveltimes	75
4.2.3	Discussion	79
4.3	Gravity	82
4.3.1	Results and Discussion	86
4.4	Line Drawing Migration	88
4.5	Integrated Interpretation	91
5	Conclusions	97
A	Station and land shot list	100
B	Legend of Geological Map of Cyprus	111
	Bibliography	113

List of Figures

1.1	Overview map of the tectonics of the eastern Mediterranean Sea	4
1.2	Tectonic evolution of the eastern Mediterranean region during the Pliocene (5 Ma) to recent (after Schattner, 2010)	6
1.3	Overview map of the geological units in the eastern Mediterranean and compilation of previous wide-angle seismic investigations	9
1.4	(a) Schematic cross section of the Troodos Ophiolites on Cyprus, (b) stratigraphic table and (c) tomographic section beneath Cyprus	15
1.5	(a) Cross-section through the ESM, (b) 1-D velocity models from ESM and Cyprus	19
2.1	Average seismic velocities of different rock types, modified after Sheriff and Geldart (1982); Bourbié et al. (1987); Christensen and Mooney (1995)	21
2.2	Schematic sketch showing the principles of Snell's Law	22
2.3	Traveltime curve and seismic phases and ray paths	23
2.4	Wide-angle seismic data workflow	25
2.5	Different types of velocity parameterisation (after Rawlinson, 2000)	26
2.6	Square grid of velocity nodes used by the method of Vidale (1988), A is the source grid point and h is the mesh spacing.	28
3.1	Station map	38
3.2	Schematic sketch showing the survey geometry for wide-angle profile WARRP27 (after Hübscher, 2012)	39
3.3	Frequency content of the OBS03	43
3.4	Frequency content of the OBH23	43
3.5	Butterworth bandpass filter	44
3.6	All picked first arrivals and second arrivals for the onshore and on-offshore parts of the profile.	45
3.7	Seismic section of OBS02	47
3.8	Seismic section of OBS02 with picked first arrivals	47
3.9	Seismic section of OBS17	48
3.10	Seismic section of OBS17 with picked first arrivals (red dots with black outline).	48
3.11	Seismic section of station C229 on Cyprus	49
3.12	Seismic section of station C229 with picked first arrivals (red dots with black outline).	49
3.13	Seismic section of southern land shot without picks	50
3.14	Seismic section of southern land shot with picks	50
3.15	Seismic section of northern land shot without picks	51
3.16	Seismic section of northern land shot with picks	51

4.1	All picked first arrival times (reduced by 8 km/s) and a best fit line (red line) which is used for estimating the initial 1-D velocity model.	53
4.2	Initial 1-D P-wave velocity model used in this study.	54
4.3	Final P-wave velocity model of the offshore part only (above) and corresponding ray plot (below). The Moho is inverted from the data.	55
4.4	Detailed geological map of Cyprus with receiver locations. Legend is shown in Appendix B.	59
4.5	Initial layered velocity model for the Troodos ophiolite complex beneath Cyprus. Red triangles are stations onshore Cyprus (C201 - C250), SDC = Sheeted Dyke Complex, PL = Pillow Lavas, P-wave velocities are shown in Table 4.3 and the P-wave velocity scale is shown in Fig. 4.6.	59
4.6	Off- / On-Offshore initial P-wave velocity model no. 10001.	59
4.7	Final tomographic P-wave velocity model with key observations labeled with 1. - 6.	61
4.8	Final tomographic P-wave velocity model with modelled upper crustal reflection	63
4.9	Checkerboard test with a grid size of 10x4 km	64
4.10	Checkerboard test with a grid size of 15x6 km	64
4.11	Seismic section of OBS02 with picked and calculated traveltimes.	65
4.12	Seismic section C229 with picked and calculated traveltimes.	66
4.13	Final layered velocity model with labeled layers (a-h) and main observations (i-iii, see text).	73
4.14	Final layered velocity model in which modeled refractions (a.) and reflections (b.) are shown	76
4.15	Seismic section of northern land shot with picked and calculated traveltimes	77
4.16	Synthetic seismogram section of northern land shot	78
4.17	Seismic section of southern land shot with picked and calculated traveltimes	79
4.18	Geometrical elements involved in the gravitational attraction of an n-sided polygon, modified after Talwani et al. (1959)	84
4.19	Final gravity model with observed and calculated gravity values	85
4.20	Example of input data (OBS 24) for pre-stack line-drawing migration	89
4.21	Result of the pre-stack line-drawing migration	90
4.22	Final geodynamic interpretation with associated geological units and seismicity distribution.	93
4.23	Comparison of flat subduction settings adapted from Lallemand et al. (2005)	94
4.24	Schematic blockmodel and evolution of the high velocity block beneath the Troodos ophiolites	96

List of Tables

1.1	Tectonic and geological units along the amphibious wide-angle seismic profile and associated questions	7
1.2	Combined stratigraphic cross-section of the <i>TG-6</i> well (Fernandez-Blanco et al., 2013) and <i>Esmekaya-1</i> well (Aydemir and Ates, 2006a)	11
1.3	Lithological cross-section of the <i>CY-4</i> well	16
1.4	Summary of previous investigations concerning the ESM (after Robertson, 1998a) and adjacent areas	18
3.1	Summary of the wide-angle survey (offshore part)	40
3.2	Summary of the wide angle survey (onshore part)	41
3.3	Coordinates of profile line	42
4.1	Initial 1-D P-wave velocity model used in this study.	54
4.2	Examples of model series with corresponding inversion parameters.	57
4.3	Stratigraphic units beneath Cyprus, the stations located on the unit and the corresponding P-wave velocity from Mackenzie et al. (2006); Salisbury et al. (1989); Smith and Vine (1989). Layered P-wave velocity model for Cyprus is shown in Fig. 4.5	58
4.4	Initial 1-D velocity models for the onshore part (Turkey and Cyprus), LT = Layer Thickness, LS = Land Shot, AGS = Airgun Shot	70
4.5	Final layered P-wave velocity model. Units are labeled in Fig. 4.13.	71
4.6	Units of the layered P-wave velocity model and the corresponding density (calculated after Birch's law, Eq. 4.1)	83
A.1	Station list	110

Abbreviations

CoCoCo	incipient C ontinent C oontinent C ollision
ESM	E ratosthenes S eamount
OBS	O cean B ottom S eismometer
OBH	O cean B ottom H ydrophone
NAFZ	N orth A natolian F ault Z one
EAfZ	E ast A natolian F ault Z one
DSFZ	D ead S ea F ault Z one
HA	H ellenic A rc
CYA	CY prus A rc
sps	samples p er s econd
GIPP	G eophysical I nstrument P ool P otsdam
EDL	E arth D ata L ogger
FD	F inite D ifference
CPU	C entral P rocessing U nit
KB	K onya B asin
TGB	TuzG özü B asin

Chapter 1

Introduction

1.1 Eastern Mediterranean

The term Eastern Mediterranean region is geographically defined as the most eastern part of the Mediterranean Sea with Cyprus located in the center of it. The region is bordered by Turkey in the north, by Israel, Lebanon and Syria in the east, by Egypt in the south and Greece and the Sea of Crete in the west. The term Levant is also used for this region to define it in a geographical and cultural way. It consists of the lands (Syria, Lebanon, Palestinian Territories, Israel and Jordan) and islands (Cyprus) of the eastern Mediterranean ([Graf, 2010](#)).

The eastern Mediterranean is associated with the interaction of four of the Earth's major lithospheric plates, Arabia, Africa, Anatolia and Eurasia (see Fig. 1.1). [McKenzie \(1972\)](#) provided a first-order, plate tectonic description of the region, recognizing active continental collision in eastern Turkey (Bilis Suture Zone), a westward, lateral transport of Anatolia accommodated by the North and East Anatolian fault zones (NAFZ and EAFZ in Fig. 1.1), subduction of African oceanic lithosphere (i.e. Neotethys) along the Hellenic and Cyprus arcs and extension in the Aegean and western Turkey (described main tectonic plate motions shown by white arrows in Fig. 1.1; [Reilinger et al., 2006](#)).

The region is composed of two separate tectonic domains, the northern Alpine orogenic belt, and the southern Eastern Mediterranean basin, with the two linked by subduction and plate collision ([Jowitt, 2007](#)).

The recent plate motions of the involved plates were investigated by [McClusky et al. \(2000, 2003\)](#) and [Reilinger et al. \(2006\)](#). The entire continental region south of the NAFZ (Arabia, Anatolia and the Aegean region) is involved in a circulatory, large-scale counterclockwise rotation, occurring since the Pliocene time ([Piper et al., 2010](#)), which dominates the plate motion in the eastern Mediterranean (see thin arrows in Fig. 1.1). These arrows reveal that the Arabian platform moves northwards with $15 - 18 \pm 2$ mm/y relative to Eurasia. Central Anatolia is characterized by coherent plate motion (internal deformation of < 2 mm/y) with a westward plate motion of $21 - 24 \pm 1$ mm/y, de-coupled from Eurasia along the right-lateral, strike-slip North Anatolian fault zone. The largest relative motions across plate boundaries occur along the Hellenic Arc. The Aegean region is moving rapidly towards the south-west, with $30 - 33 \pm 1$ mm/y relative to Eurasia. From some rare GPS stations in Egypt, a slow ($5 - 6 \pm 2$ mm/y) northward motion of the African Plate relative to Eurasia is observed.

One of the main recent tectonic features in the eastern Mediterranean is the Hellenic Arc (HA in Fig. 1.1) in the west of the study area, which is well studied and understood ([Makris, 1976](#); [Angelier et al., 1982](#); [Pichon and Angelier, 1979](#); [Makropoulos and Burton, 1984](#)), whereas its eastward extension, the Cyprus Arc (CYA in Fig. 1.1) is one of the less well-understood parts of the Alpine-Himalayan tectonic belt ([Pilidou et al., 2004](#)). Due to the similar geometry of the Hellenic Arc and the Cyprus Arc the two are often compared ([Wdowinski et al., 2006](#); [Stride et al., 1977](#); [Papazachos and Papaioannou, 1999](#)). However, observations of plate motions and seismicity revealed that the two arcs are connected to very different tectonic settings. The convergence across the Hellenic Arc is with $20 - 40$ mm/y, about two to three times faster than across the Cyprus Arc. This high rate yields a significantly higher level of seismicity with much greater hypocentral depths (up to 300 km). Another difference is the direction of relative motion: it is normal along the whole Hellenic Arc, whereas it is normal at the central part of the Cyprus Arc and subparallel at the eastern part of it. The reason for this is the different nature of convergence at the two arcs, with the Hellenic Arc being subjected to subduction throughout its entire length, whereas the Cyprus Arc is connected to subduction, collision and transcurrent motion ([Wdowinski et al., 2006](#)).

Several previous studies investigated the origin, evolution and tectonic context of the eastern Mediterranean basin ([Hsü, 1978](#); [Robertson and Dixon, 1984](#); [Ben-Avraham and Ginzburg, 1990](#); [Kissel et al., 2003](#)).

The Levantine Basin, east of the study area is also a well investigated area (Netzeband et al. (2006); Ben-Avraham et al. (2002), see table 1.4), although whether the origin of the crust beneath the basin is either oceanic (Ben-Avraham et al., 2002; Makris et al., 1983) or thinned continental (Netzeband et al., 2006; Gardosh and Druckman, 2006) is still under debate. The maximum sedimentary thickness within the basin is estimated to be 14 – 15 km (Ben-Avraham et al., 2002; Gardosh and Druckman, 2006).

The Levant region east of the Levantine Basin is tectonically affected by the recently ongoing collision of the Arabian plate with the Eurasian plate. Its main tectonic feature is the Dead Sea transform fault zone (DSFZ) which is a left-lateral strike slip fault with a total length of more than 1000 km, running from the Red Sea to the Biltis belt at the Maras triple junction (Adiyaman and Chorowicz, 2002). The total left lateral offset along the DSFZ is estimated to be 100 – 110 km, and has occurred since the Middle Miocene ($\sim 20 Ma$; e.g. Zak and Freund, 1981; Garfunkel, 1981; Marco, 2009). Slip mechanisms along the Dead Sea transform fault zone (DSFZ) vary from pure left-lateral strike slip (southern part) through left-lateral transtension in, for example, the Dead Sea basin to left-lateral transpression (northern part; $4 - 6 \pm 1 mm/y$; McClusky et al., 2003).

Tectonic evolution

The geological and tectonic evolution of the Anatolian plate and the eastern Mediterranean region is highly connected with the opening of the Neotethys ocean in late Paleozoic - early Mesozoic time, followed by rifting of several continental fragments from the northern edge of the Gondwana continent during Mesozoic and subsequent progressive closure of the Neotethys ocean (Robertson and Comas, 1998). The basin started to develop during the late Paleozoic - early Mesozoic when the Eratosthenes block, among other continental fragments, drifted northward away from the Gondwana super-continent (Schattner, 2010; Garfunkel, 1998). The tectonic evolution continues with northward drifting of these continental fragments across the Mesozoic Neotethys ocean, subduction and re-assembly of continental fragments to form the present-day Tauride-Anatolide belt during Late Cretaceous - Cenozoic (Robertson and Dixon, 1984; Okay and Tüysüz, 1999; Robertson et al., 2013a,b). Towards the terminal stages of the Neo-Tethys, during the

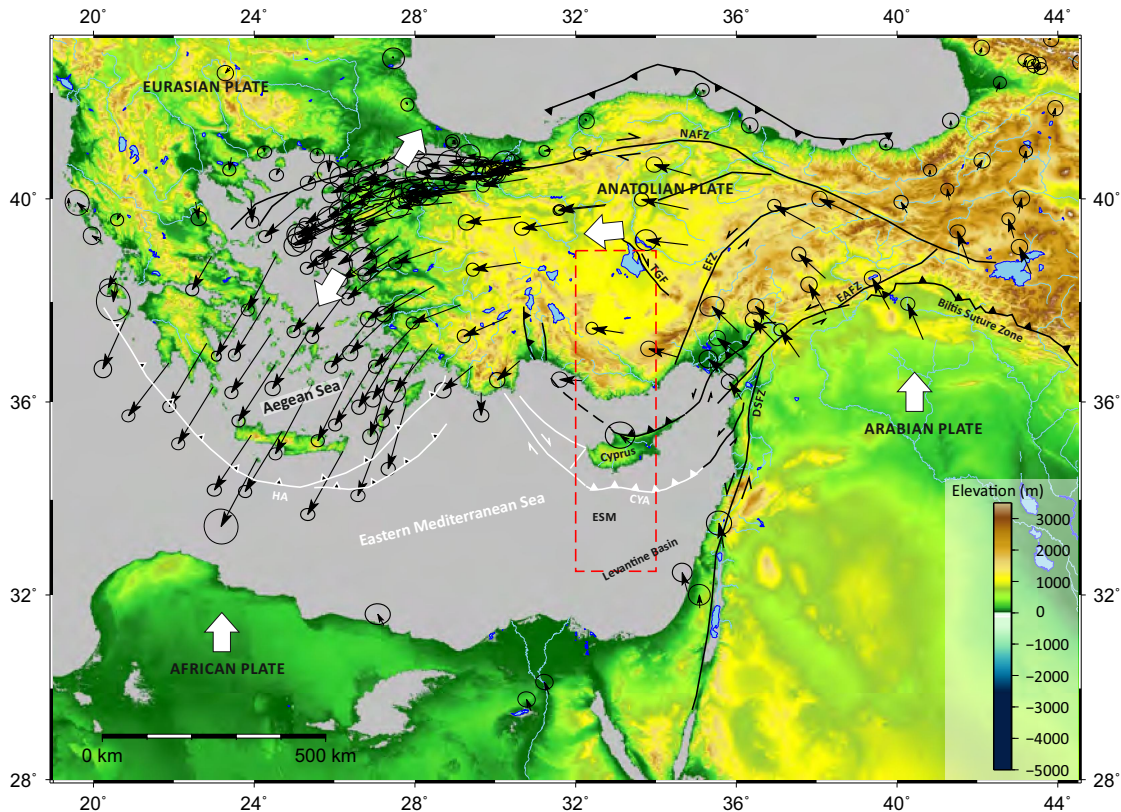


FIGURE 1.1: Overview map of the tectonics of the eastern Mediterranean Sea. Arrows indicate horizontal plate movement from GPS data after [McClusky et al. \(2000\)](#), faults are from [Schildgen et al. \(2012b\)](#) and white arrows indicate general plate movements. HA = Hellenic Arc, CYA = Cyprus Arc, ESM = Eratosthenes Seamount

late Paleogene to the present, the entire northern flank of the Afro-Arabian plate progressively subducted northward beneath Eurasia and formed the recent subduction zones of the Hellenic Arc and Cyprus Arc (see Fig. 1.1, [Schattner, 2010](#)). This is a widely accepted model and explains many aspects of the geology of the region ([Robertson et al., 2012](#)).

Throughout Plio-Pleistocene time the progressive closure of the eastern Mediterranean basin continued across the Bitlis-Zagros collision zone and the Cyprus, Hellenic and Calabria arcs at variable rates ([Schattner, 2010](#)). The Eratosthenes Seamount (ESM in Fig. 1.1), considered as a northward drifted continental fragment of the African plate ([Ben-Avraham et al., 2002](#); [Netzeband et al., 2006](#); [Robertson, 1998b](#)), collided with the subduction trench along the Cyprus Arc during the Late Pliocene - early Pleistocene (Fig. 1.2), triggering rapid uplift of Cyprus. Concurrently, uplift of the Taurides may relate to break off or delamination of a remnant oceanic slab ([Robertson et al., 2012](#)). Due to the transition from subduction to collision along the Cyprus Arc, the entire

eastern Mediterranean was massively deformed during the early-to-mid Pleistocene. Co-occurrence of the structural modifications recorded in the entire region was synchronous rather than a cascade of events. [Schattner \(2010\)](#) discusses this tectonic evolution in detail and figure 1.2 illustrates the timing and characteristics of the mentioned tectonic deformations.

1.2 Project Objectives and Motivation

The wide-angle seismic investigation presented here, took place within the *CoCoCo* project which was launched in 2010 / 2011. This project strives for a quantitative understanding of earth processes related to incipient **C**ontinent-**C**ontinent **C**ollision and to reveal its impact on the crystalline basement and sedimentary cover, as exemplified by Cyprus and the Eratosthenes Seamount (ESM) ([Ben-Avraham et al., 2002](#); [Netzeband et al., 2006](#); [Robertson, 1998b](#)) in the eastern Mediterranean. As the ESM is considered as a continental fragment of the African plate ([Ben-Avraham et al., 2002](#); [Netzeband et al., 2006](#); [Robertson, 1998b](#)), this tectonic setting provides the unique opportunity to investigate the transition from subduction to continent-continent collision. The 3D-geometry of the down thrustured crustal block of the seamount will be examined for the first time by the integrated interpretation of refraction, gravity, magnetic, magneto-telluric and multi-channel seismic data within the CoCoCo Project.

Subduction-to-collision settings have been documented mainly in the circum Pacific region, for example the Daisha Seamount which is approaching the Japan trench ([Cadet et al., 1987](#)) collision of the Louisville Ridge with the Tonga trench ([Dupont, 1985](#)) and subduction of seamounts at the Mariana and Izu-Bonin trenches ([Fryer and Smoot, 1985](#)). In contrast to the above mentioned Pacific scenarios, the ESM collision provides the unique opportunity to investigate the transition from subduction to continent-continent collision as the ESM is considered as continental crust ([Ben-Avraham et al., 2002](#); [Netzeband et al., 2006](#); [Robertson, 1998b](#)).

In particular the objectives of the wide-angle seismic study, presented in the following chapters, can be summarized as:

- Processing and analysis of an amphibian wide-angle reflection / refraction profile

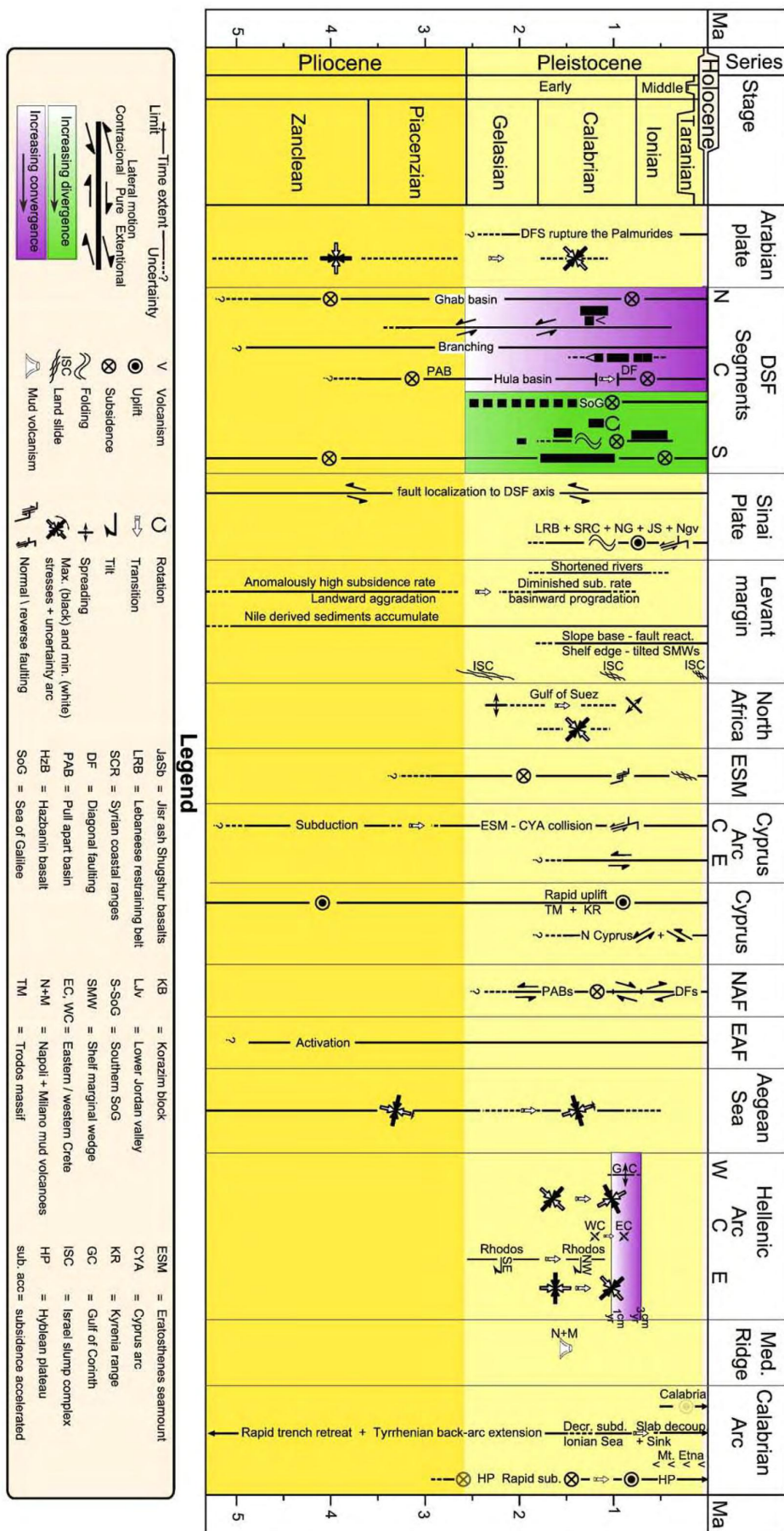


FIGURE 1.2: Tectonic evolution of the eastern Mediterranean region during the Pliocene (5 Ma) to recent (after [Scharntner, 2010](#))

- Frequency analysis, filtering, geometry editing and travel-time determination (see chapter 3, *Seismic Data and Processing*)
- Performing a 2-D ray tracing and travel-time inversion (see chapter 4, *Crustal Modelling and Results*)
- Revealing the 2-D geometry of the uplifted and overriding Cyprus-Anatolian plate (see chapter 4, *Crustal Modelling and Results*)
- Determining the nature, origin and deformation of the upper lithosphere of the primary building blocks (ESM, Cyprus and Anatolian Plateau; see chapter 5, *Conclusions*)

Based on these aims a 650 km long amphibious wide-angle seismic profile was deployed extending from the central Anatolian plate in the north to the ESM in the south (see red box in Fig. 1.3 and chapter 3.1). The main tectonic and geological features along the presented wide-angle profile are introduced in section 1.3 and shown in Table 1.1. Furthermore Table 1.1 shows some concrete questions associated with the studied geological units, which the present investigation tries to answer.

TABLE 1.1: Tectonic and geological units along the amphibious wide-angle seismic profile and associated questions

geological unit (from north to south)	questions
Central Anatolian Plateau (Central Turkey)	How thick is the crust of the Anatolian Plateau?
Central Taurides (S. Turkey)	Do the Taurus Mountains (Turkey) sit on the leading edge of the Anatolian plateau like the Himalayas do with respect to Tibet or is there a crustal root beneath the Taurus Mountains?
Cilicia-Adana Basin (Between S. Turkey and Cyprus)	
Cyprus (Troodos Ophiolites)	Is Cyprus floored by oceanic or continental crust? If Cyprus is floored by oceanic crust, where does the transition to the continental crust of the Anatolian micro-plate occur? How thick is the Troodos sequence?
Cyprus Arc (South of Cyprus)	
Eratosthenes Seamount	What is the nature and origin of the ESM? Is it a rifted continental fragment or is it of oceanic origin? How far does the downthrustured Eratosthenes Seamount stretch northwards and beneath the overriding Cyprus and Anatolian plate?

Thus this study tries to reveal structural information about the features summarized in Table 1.1, (such as geometry, seismic velocity distribution, crustal thicknesses) from new

geophysical data (wide-angle seismic and gravity). One main focus will be to examine the suggested continuation of the Cyprus Arc beneath Cyprus and derive a crustal model for the collision zone between the Eratosthenes Seamount and Cyprus. The question will be tackled if there is some evidence for a northward dipping slab arising from the subduction of the African plate beneath Cyprus (e.g. [Mackenzie et al., 2006](#); [Berk Biryol et al., 2011](#); [Kempler and Ben-Avraham, 1987](#)).

1.3 Tectonics and Geology

The study area is located within a complex tectonic and geological setting ranging from Central Anatolia in the north to the Eratosthenes Seamount in the south. Therefore it stretches across diverse geological and tectonic domains such as the Central Anatolian Plateau, the uplifted crust of Cyprus, the subduction zone of the Cyprus Arc and the continental fragment of the ESM.

Within the study area (see Fig. [1.3](#), red box), several major geological domains can be identified. From north to south these domains are:

- Central Anatolian Plateau
- Central Taurides (S.Turkey)
- Cilicia Adana Basin (Between S. Turkey and Cyprus)
- Cyprus
- Eratosthenes Seamount

In the following subsections the geological evolution and main tectonic features of these sub-areas and the associated previous investigations are introduced and discussed.

Central Anatolian Plateau, Taurides (S.Turkey) and the Cilicia-Adana Basin

The entire onshore part of the study area in Turkey is located within the Central Anatolian Plateau which marks the western end of the zone associated with the continental

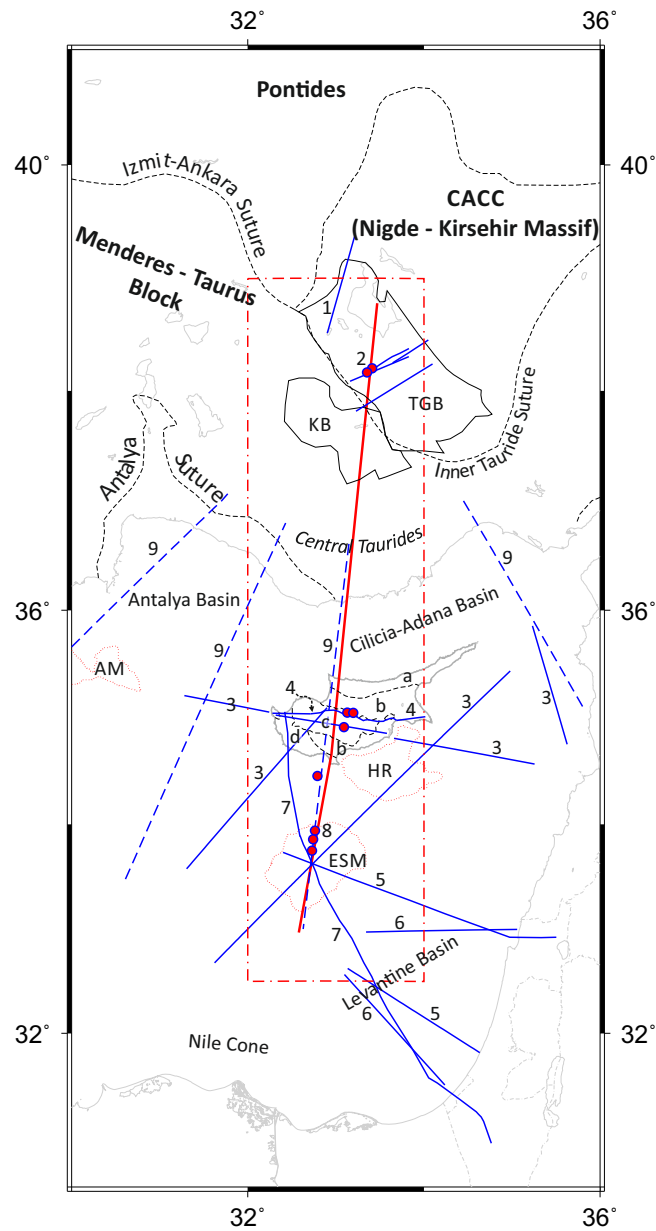


FIGURE 1.3: Overview map of the geology of Turkey and Cyprus and compilation of previous wide-angle seismic investigations. Black dashed line shows major sutures (Clark and Robertson, 2002), red dotted areas show continental blocks and red dots indicate existing wells (Aydemir and Ates, 2006a; Robertson, 2000). ESM = Eratosthenes Seamount, HR = Hecateus Ridge, AM = Anaximander Mountains, KB = Konya Basin, TGB = TuzGözü Basin, CACC = Central Anatolian Crystalline Complex modified after Okay (2000, 2008); Clark and Robertson (2002); Görür et al. (1998); Dilek and Sandvol (2009). Main geological terranes in Cyprus after Geological Survey Department (1995): a = Kyrenia Terrane, b = Circum Troodos Sedimentary Succession, c = Troodos Terrane (Ophiolite), d = Mamonia Terrane. Red line is the seismic profile of this study, blue lines indicate previous seismic studies: 1 = Gürbüz and Evans (1991), 2 = Aydemir and Ates (2006a); Fernandez-Blanco et al. (2013), 3 = Zverev (2010), 4 = Mackenzie et al. (2006), 5 = Ben-Avraham et al. (2002), 6 = Netzeband et al. (2006), 7 = Makris et al. (1983), 8 = wells from Robertson (1998b) and blue dashed lines (no. 9) are gravity cross-sections from Ergün et al. (2005).

collision of the Arabian plate with Eurasia. It is located between the predominantly compressional Eastern Anatolian Plateau and the predominantly extensional Western Anatolian province (Fig. 1.1) and includes parts of the Central Anatolian Crystalline Complex (CAAC) and the Menderes - Taurus Block (Fig. 1.3).

The northern edge of the study area is located within the southern part of the Central Anatolian Crystalline Complex (CACCC, Fig. 1.3). This complex is a large region of metamorphic and granitic rocks with Cretaceous to Miocene ages (Okay, 2008; Dilek and Sandvol, 2009) which occupies most of central Turkey (Göncüoğlu et al., 1997). It consists of the Kirsehir, Akdag and Niğde massifs and several curvilinear sedimentary basins (Tuzgölü, Ulukisla and Sivas), which initially evolved as peripheral foreland and/or forearc basins in the late Cretaceous, and delimit the CACCC in the west, the east and the south (Dilek and Sandvol, 2009). The Central Anatolian Crystalline Complex is regarded either as the metamorphosed northern margin of the Anatolide-Tauride terrane or a distinct terrane separated from the Anatolide-Taurides by the Inner Tauride suture.

In particular the amphibious wide-angle profile starts within the Tuz Gölü basin, the western part of which was investigated by Gürbüz and Evans (1991) using seismic refraction data (blue line, no. 1 in Fig. 1.3 NW of the Tuz Gölü). They concluded a varying depth of the basement along their profile of about 3 km below the southwestern end of the profile to 10 km below two basement depressions within the profile. They derived a middle sedimentary layer with a P-wave velocity of about 4.0 – 4.2 km/s and associated this with evaporites. For the metamorphic basement, consisting of metasediments typical for the region, P-wave velocities of 6.15 km/s are suggested. In addition to this some well data are available from Aydemir and Ates (2006a) and Fernandez-Blanco et al. (2013). Table 1.2 shows a combined stratigraphic columnar section of the well data (location of both wells is shown as no. 2 in Figure 1.3). The location of the wells along the profile is at about 66.5 km (65 km for the *Esmekaya-1* well and 68 km for the *TG-6* well).

South of the Tuz Gölü basin the Konya basin is located, which is infilled with up to 400 m thick Quaternary lake marls and other, mainly fine grained sediments (Roberts et al., 1999; De Ridder, 1965). The southern margin of the Konya basin marks the geological transition from the Central Anatolian Plateau to the Central Taurides, where topography increases and older rocks appear at the surface.

TABLE 1.2: Combined stratigraphic cross-section of the *TG-6* well (Fernandez-Blanco et al., 2013) and *Esmekaya-1* well (Aydemir and Ates (2006a)); for location see no.2 in Fig. 1.3). * = Formation / P-wave velocity after Aydemir and Ates (2006a), ** = Formation / P-wave velocity after Fernandez-Blanco et al. (2013), *** = estimated P-wave velocity after Christensen and Mooney (1995)

Depth [m]	Age	Formation	Lithology	P-wave velocity [m/s]
800- 900	Mio - Pliocene	Cihanbeyli	conglomerate, sandstone, siltstone, claystone and lacustrine limestone	2035 - 3585
	Oligo - Miocene	Kochisar (*) / Eskipolati (**)	claystone, marls and siltstones	3042 (*) - 4260 (**)
1200 - 1300	Upper Cretaceous	Kartal	Metamorphic unit: terrestrial redbeds and conglomerates	~ 4600
1926		BASEMENT	Magmatic unit: diabase and splitic basalt	~ 6600 (***)
4609				

For the central Anatolian block Vanacore et al. (2013) proposed an average crustal thickness of about 37 km, which is consistent with typical continental crust. Towards the southern edge of central Anatolia and Cyprus they observed a crustal thinning to 30 km.

The main part of the study area onshore Turkey is located within the central Tauride (or Anatolide-Tauride) unit (Fig. 1.3) which covers western and southern Turkey and is thereby the largest unit in the Anatolian domain. It is accepted as a fragment of Gondwana because it is underlain by Paleozoic sediments, mainly clastics, which resemble the coeval sediments of northern Arabia and North Africa (Garfunkel, 2004). The term Anatolides is used to designate the metamorphosed rocks at the northern edge of the Anatolide-Tauride Block, whereas the term Taurides designates the non-metamorphosed thrust and folded sediments, more to the south (Pourteau et al., 2010; Okay, 1984). This area mainly consists of a stack of thrust sheets of Paleozoic and Mesozoic sedimentary rocks (Okay, 2008). Subsequently, the Eocene to middle Miocene deformation phases of the Taurides in southern Turkey resulted from closure of the Inner Tauride Ocean between the northern end of the Tauride block and the Central Anatolian Crystalline Complex (Gökten, 1993; Pourteau et al., 2010; Cosentino et al., 2012) with magmatism associated with the Eocene slab break-off event following ocean closure (Kadioglu and Dilek, 2010; Kadioglu et al., 2006).

Schildgen et al. (2012a) investigated the marine sediments of the Mut basin, located in the central Taurides and concluded a multi-phased surface uplift along the southern margin of the Central Anatolian plateau from Late Miocene to the present. The uplift history involves a phase of ca. 0.8 km of surface uplift starting between 8 and 5.5 Ma

until 1.6 *Ma* and a phase of rapid uplift starting at ca. 1.6 *Ma* that has increased the margin elevation by ca. 1.2 *km* and likely continues to the present day. This scenario is explained by lithospheric slab break-off and the arrival of the ESM at the collision zone south of Cyprus (Schildgen et al., 2012b, 2014).

Between the southern coast of Turkey and the northern coast of Cyprus the Cilicia-Adana basin is located. It is claimed to have been formed as a result of the differential incompatibility arising at an intracontinental FFF-triple junction¹, where the East Anatolia and the Dead Sea Transform Faults meet (Ediger et al., 1997). The basin is characterized by an E-W striking extensional fault system. Sediment thicknesses increase eastward from about 1 *km* to about 1.8 *km* in the middle part of the Cilicia-Adana basin, and to about 3 *km* in the east, near Adana Bay, which experienced input from the Seyhan River (Robertson, 1998a). In the central part of the basin, where the profile crosses it, sediments are estimated to comprise ~ 1000 *m* of Plio-Quaternary plus Messinian and 1000 *m* of pre-Messinian rocks (Ergün et al., 2005). A detailed discussion of the sediments and tectonic features of the Cilicia-Adana basin is given by Aksu et al. (2005) and Ozel et al. (2007).

Cyprus

Cyprus is the third largest Mediterranean island with a surface of 9251 *km*² and is located in the north-eastern corner of the Mediterranean Sea (app. centered on 35°N/33°E).

Cyprus consists of four main geological units (Figure 1.3, a - d). The main terrane on Cyprus is the central Troodos ophiolite complex (*c* in Fig. 1.3), which was uplifted during late Pliocene-Pleistocene time. This can be largely explained by the collision of the Eratosthenes Seamount with a subduction zone south of Cyprus (Robertson et al., 2013a). The circum-Troodos sedimentary succession (*b* in Fig. 1.3) covers the area between the Kyrenia Terrane (*a* in Fig. 1.3) and Troodos Terrane (*c* in Fig. 1.3) as well as the southern part of the island. It consists of autochthonous² sedimentary rocks. Carbonate sedimentation began in the Palaeocene (65 Ma) with the deposition of the Lefkara Formation (No. 11 in Fig. 1.4(a)), which includes marls and chalks with characteristic white colour, with or without cherts (Geological Survey Department, 1995). The Lefkara

¹a place where three tectonic plates meet, **FFF**-triple junction = all transform triple junction

²rocks which are located at the place of their original formation, in contrast to allochthonous rocks, which have been relocated from their site of formation (Bates et al., 1984)

Formation is followed by the Pancha Formation (23 - 7 Ma) and the evaporites of the Kalavassos Formation (No. 9 in Fig. 1.4(a)) in the Upper Miocene (7 Ma). They consist mainly of yellowish marls and chalks and gypsum and gypsiferous marls, respectively. During the Pliocene time (5 Ma) a new cycle of sedimentation began and the Nicosia Formation (No. 8 in Fig. 1.4(a)) was deposited consisting of siltstones, calcarenites and marls. Finally in the Pleistocene the fan conglomerate was deposited which includes clastic deposits (gravels, sand and silt; No. 7 in Fig. 1.4(a); [Geological Survey Department, 1995](#)). The Mamonia Zone (*d* in Fig. 1.3 and No. 1 in Fig. 1.4(a)) contains a diverse and structurally complex assemblage of igneous, sedimentary and metamorphic rocks, ranging in age from Middle Triassic to Upper Cretaceous (230 - 75 Ma). These rocks, which are regarded as allochthonous were placed over and adjacent to the Troodos ophiolite during the Maastrichtian ([Geological Survey Department, 1995](#)). The Kyrenia Terrane (*a* in Fig. 1.3 and No. 12 in Fig. 1.4(a)) is located in the northern part of Cyprus close to the northern coast and forms a narrow, steep-sided chain of mountains which rise abruptly up to an altitude of about 1000 m. The terrane consists of allochthonous limestone formations, which were thrust southward over the younger autochthonous marine sediments of Campanian to Eocene age (85 - 40 Ma). These sediments include pelagic marls and chalks with cherts ([Geological Survey Department, 1995](#)).

The juxtaposition of these oceanic and continental fragments took place in a series of tectonic episodes. It was initiated with the subduction of the African Plate beneath the Eurasian Plate and the formation of the Troodos Ophiolite (Upper Cretaceous, 90 Ma). Following a relative inactive tectonic phase (75 to 10 Ma), the placement of the Kyrenia Terrane and the uplift of the island to almost its present position (Miocene, 10 - 15 Ma) took place and constitutes an important tectonic episode in the geological evolution of Cyprus ([Geological Survey Department, 1995](#)).

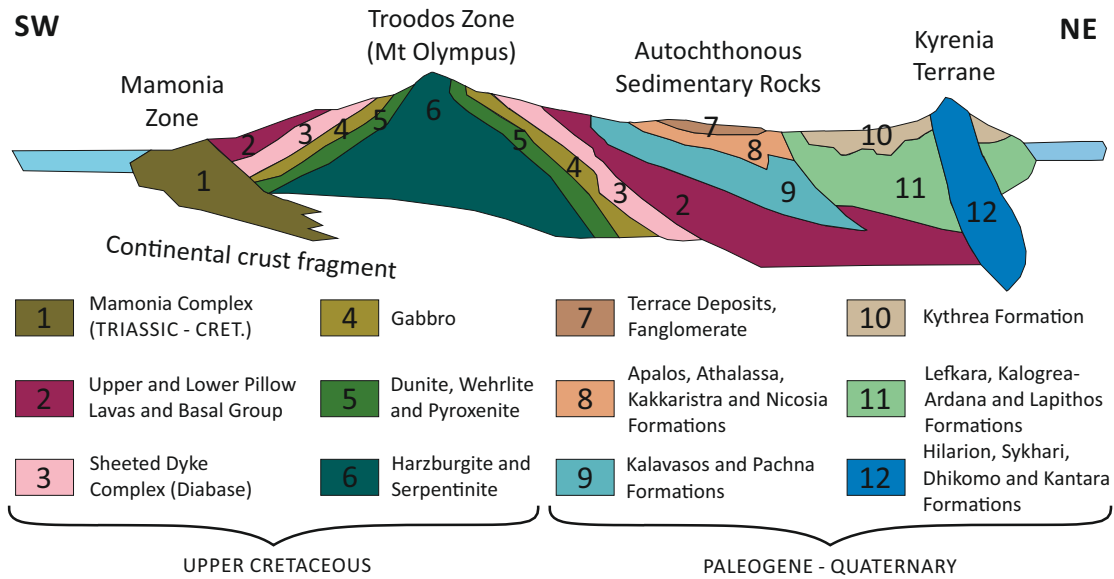
The island, which has been continuously uplifted since the late Miocene, was rapidly uplifted and completely emerged from the sea during the early Pleistocene ([Kempler, 1998](#); [Harrison et al., 2004](#)). Due to the complexity of plate interactions, different ideas exist about the neotectonic setting of Cyprus. One idea is that an active subduction zone, located between the Eratosthenes Seamount and Cyprus, referred as the Cyprus Arc, has been the main driving force behind the uplift of the island ([Gass and Masson-Smith, 1963](#); [Robertson, 2000](#); [Kempler and Ben-Avraham, 1987](#)). One problem regarding a "classical" subduction zone model is an absence of volcanism on Cyprus at any time

during the Cenozoic and the absence of a northerly dipping Benioff Zone beneath Cyprus (Harrison et al., 2004). Therefore Harrison et al. (2004) support a tectonic model which includes collision of the ESM and the southern margin of Cyprus during the Pleistocene, which triggered a rapid uplift of Cyprus, followed by domination of a major left-lateral strike-slip fault system located between Cyprus and the Eratosthenes Seamount rather than a classical subduction zone. In contrast to this Berk Biryol et al. (2011) proposed a slab beneath Cyprus subducted along the Cyprus Arc (see Fig. 1.4(c)).

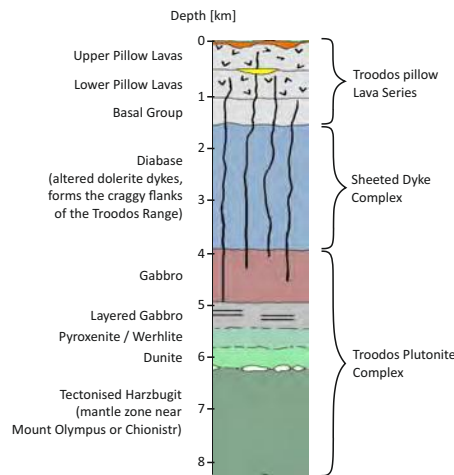
The most prominent geological feature on Cyprus is the ophiolite sequence of the Troodos massif with an estimated U-Pb zircon age of 91 ± 1.4 Ma. The whole ophiolite complex was obducted³ and emplaced on continental crust in the Late Cretaceous (ca. 75 Ma) (Silantsev and Portnyagin, 2005; Ghose et al., 2014) and has an overall dome geometry centered on Mt Olympus. The core of the dome is serpentinized mantle peridotite, which is surrounded by a plutonic then a sheeted dyke complex (SDC) with overlying extrusive lavas and sediments (Mackenzie et al., 2006). Figure 1.4(a) shows a schematic section through the Troodos complex and a stratigraphic section. Oceanic crust preserved as ophiolite sequences are found widely across the eastern Mediterranean, including ophiolites in Bosnia, Croatia, Greece (e.g. Othris, Pindos ophiolites), Oman (e.g. Semail ophiolite), Syria (e.g. Hatay, Baer-Bassit ophiolites), Turkey (e.g. Lycian, Armutlu ophiolites,) and Cyprus, with its Troodos ophiolite and associated, but still controversial, Mamonia complex (Jowitt, 2007). The Troodos massif on Cyprus belongs to a group of ophiolites (including Kizildag in southern Turkey and the Baer-Bassit ophiolite of Syria, Dilek and Moores, 1987) which are well preserved and relatively undeformed, so that almost the complete sequence through the oceanic crust can be observed (Jowitt, 2007). Figure 1.4(b) shows the ophiolite sequence of the Troodos and its lithological composition, which was used for the preliminary construction of an P-wave velocity model (see chapter 4) for the area of the Troodos complex.

From teleseismic P-wave tomography, Berk Biryol et al. (2011) resolved a fast velocity anomaly underneath Cyprus and associated this with the Cyprus trench. Down to a depth of 200 km they suggested a sub vertical slab, which begins to dip northwards with a $\sim 45^\circ$ angle between 200 and 400 km. Below 400 km the dip of the slab becomes much gentler and begins to flatten out (see Fig. 1.4(c)). Vanacore et al. (2013) find some

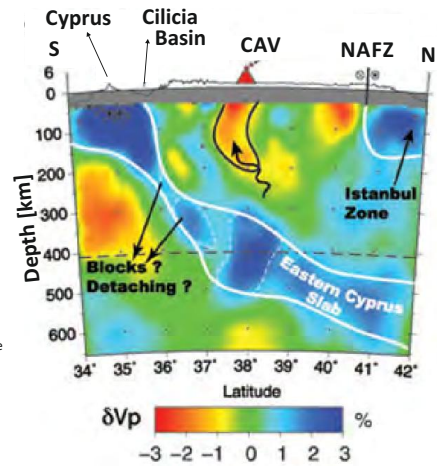
³The term *Obduction* was introduced by Coleman, 1971 and describes the overthrusting of oceanic lithosphere (Ophiolites) onto continental lithosphere at a convergent plate boundary where oceanic lithosphere is being subducted beneath continental lithosphere



(a)



(b)



(c)

FIGURE 1.4: Schematic structure of the Troodos Ophiolites on Cyprus: (a) cross section through the Troodos complex modified after Geological Survey Department (1995); (b) stratigraphic table for the Troodos complex adapted from West (2013); (c) interpretation of tomographic sections modified after Berk Biryol et al. (2011). CAV = Central Anatolian Volcanics, NAFZ = North Anatolian Fault Zone.

evidence for a complicated structure of the Moho depth beneath Cyprus. Their data were compatible with a crustal thickness of about 30 km and a deep dipping structure at a depth of ~ 55 km, which is interpreted as the slab. Koulakov and Sobolev (2006) suggested a Moho depth under Cyprus of 33 km, which is in line with the seismic refraction investigation of Ben-Avraham et al. (2002) (Fig. 1.3, no. 5) who estimated the crustal thickness to be 30 – 32 km. Makris et al. (1983) (Fig. 1.3, no. 7) postulated continental crust beneath Cyprus with a Moho at about 35 km depth. Mackenzie et al. (2006) (Fig. 1.3, no. 4 and Fig. 1.5(b)) executed a wide-angle seismic investigation on

Cyprus. In combination with some well data they suggested that the Troodos crust is only ~ 5 km thick, probably similar to average crust formed at slow spreading ridges. They could not resolve the layer beneath the ophiolite complex but assumed typical mantle velocities beneath 16 – 18 km. This would indicate a significantly different crustal thickness beneath Cyprus than other previous studies. Nevertheless they found some evidences for a deep reflector at ~ 55 km depth, which could originate from the northward dipping slab. The assumed slab is also suggested by modeling of gravity data (Kempfer and Ben-Avraham (1987); Ergün et al. (2005), Fig. 1.3, no. 9). Furthermore Ergün et al. (2005) concluded thick sediments between the Eratosthenes Seamount and Cyprus that represent the remnants of an accretionary wedge sitting in the former trench. In the late 1980s the Cyprus Crustal Study Project (CCSP) drilled three boreholes (CY-1/1a, CY-2/2a and CY4, location shown in Fig. 1.3) to investigate the geology of the Troodos ophiolite (Salisbury et al., 1989; Malpas, 1990). The borehole CY-4 penetrated 2263 metres through the sheeted dyke complex and plutonic section of the ophiolite, but do not reach ultramafic rocks of the mantle section. Table 1.3 shows the lithology of the drilled zones and the corresponding P-wave velocities.

TABLE 1.3: Lithological cross-section of the *CY-4* well after Malpas (1990). P-wave velocities are from (a) Smith and Vine (1989), (b) Mackenzie et al. (2006) and (c) Salisbury et al. (1989)

Depth [m]	Lithology	P-wave velocity [km/s]
675	Sheeted diabase dykes	6.5 ^a , 4.6-5.0 ^b , 5.0-6.4 ^c
900	Fine- to medium-grained gabbros	
1330	Fine- to medium-grained gabbro-norites and 2-pyroxene diabase dykes	
1747	Medium- to coarse-grained gabbro-norites	6.93 ^a , 6.05-6.67 ^b , 6.7-6.9 ^c
2263	Medium- to coarse-grained websterites and related rocks	7.26-7.39 ^a , 6.91-7.10 ^b , 7.0-7.4 ^c

Eratosthenes Seamount

The Eratosthenes Seamount (ESM) is located in the center of the eastern Mediterranean basin ~ 100 km south of Cyprus, bounding the passive margin of the Levant to the east and south and the Nile cone in the southwest. Its size is about 120×80 km and its peak lies at a depth of 900 m, rising about 2000 m above the surrounding seafloor (Mascle et al., 2000).

The sedimentary thickness of the ESM is approximately 5 *km* (Ben-Avraham et al., 2002). Drilling during LEG 160 has shown that at least the upper part of the seamount is predominantly composed of limestone and contains no igneous rocks (for drilling position see No. 8 in Fig. 1.3 and for cross section see Fig. 1.5(a), Robertson, 1998b). It is suggested that the ESM was uplifted by at least 1 km in post-Oligocene time, with the main reason for the uplift being seen as tectonic, rather than e.g. glacio-eustatic (Robertson, 1998b). Zverev and Ilinsky (2005) confirmed the existence of uplifted high-velocity rocks (6.2 – 7.0 *km/s*) within a complex layering pattern beneath the ESM. In contrast to other authors, they suggested that the ESM has a volcanic origin.

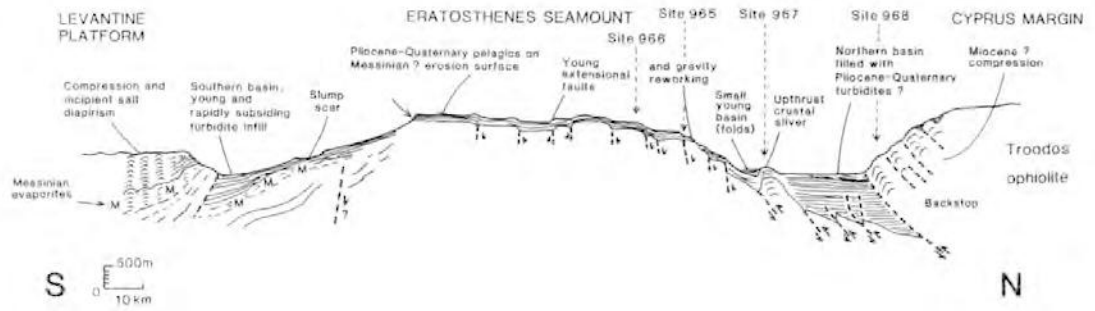
Robertson (1998b) interprets the Eratosthenes Seamount as a carbonate platform constructed on stretched continental crust rifted from the southern margin of Tethys in early Mesozoic time. Ben-Avraham et al. (2002) confirm that the crust under the ESM is continental, but note that it is thinner than normal continental crust. They suggest that this is caused by the extension that took place during the rifting of this fragment away from the African continent. By the Early Cretaceous, the Eratosthenes block formed a shallow-water carbonate platform which subsided in the Late Cretaceous and was overlain by bathyal pelagic carbonates. This subsidence is seen as the result of crustal flexure related to collision with the Cyprus active margin to the north. It is now widely accepted that the seamount is now in the process of an incipient collision with the Cyprus active margin to the north, i.e. part of the regional Africa-Eurasia boundary (Robertson, 1998b).

The Moho depth is reported to be 26 – 28 *km* beneath the ESM by Ben-Avraham et al. (2002). This is supported by the tomographic inversion of Koulakov and Sobolev (2006), who derived a crustal thickness beneath the ESM of 27 *km*. Makris et al. (1983) also inferred the presence of continental crust which is derived to be 27 *km* thick.

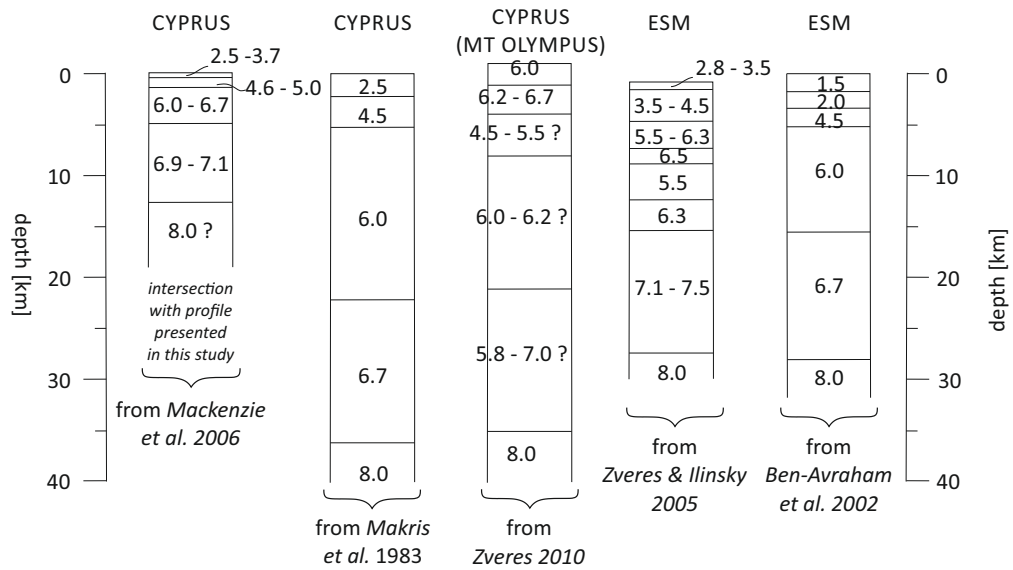
Table 1.4 shows a compiled overview of previous investigations that took place in the region of the ESM and adjacent areas such as the Levantine Basin.

TABLE 1.4: Summary of previous investigations concerning the ESM (after [Robertson, 1998a](#)) and adjacent areas

Authors	Key Observations	Comments
Netzeband et al. (2006)	The presence of thinned continental crust under the Levantine Basin is suggested	
Koulakov and Sobolev (2006)	Crustal thickness of up to 33 km in Cyprus and 27 km under the Eratosthenes Seamount	
Ergün et al. (2005)	Gravity anomalies of the Cyprus Arc and their tectonic implications	
Ben-Avraham et al. (2002)	The crust under the Levantine Basin is considered as oceanic	
Leg 160 studies: Emeis et al. (1996) ; Robertson (1998a)	Pliocene-Quaternary deep-sea muds underlain by shallow-water Miocene limestones and then by upper Eocene and Upper Cretaceous pelagic limestones; shallow-water at base; major depositional hiatuses; breccias indicate early Pliocene break up and subsidence.	Collapse of seamount to >1800 m coeval with rapid uplift of southern Cyprus in late Pliocene - early Pleistocene.
Limonov et al. (1994) ; Robertson et al. (1995a)	Seismic data indicate break-up of seamount by down-to-north normal faulting; seamount down-flexed and thrust beneath Cyprus along active margin; also compression-related subsidence along southern margin.	First clear imaging of Cyprus trench and upper part of down-going slab.
Krasheninnikov (1994)	Suggested Eratosthenes down faulted and thrust beneath Cyprus; dredged granite, basalt; Cenomanian limestone and Tortonian - Quaternary pelagic carbonate.	No evidence that granite and basalt are in situ. Dredged coral probably Miocene not Cenomanian.
Kempler (1994)	Eratosthenes as a quadrilateral graben surrounded by steep faults to produce a moat; originated as a pre-Messinian high of African origin.	High-angle faults and related moat concept not supported by later evidence.
Clube and Robertson (1986)	Relate uplift of Cyprus to underthrusting of the Eratosthenes carbonate platform or (more northerly) equivalent.	Cyprus uplift caused by collision.
Sonnenfeld and Finetti (1985)	Seismic data suggest that evaporites are absent from west of Eratosthenes Seamount.	Confirmation of Messinian edifice.
Robertson (1990) ; McCallum and Robertson (1990) ; Poole and Robertson (1991)	Synthesis of the Pliocene-Quaternary sedimentary cover of Troodos in terms of collision-related tectonic uplift of southern Cyprus.	Confirming dominant role of tectonics above north-dipping subduction zone.
Eaton and Robertson (1993)	Deformation in southern Cyprus in early Miocene related to underthrusting, possibly initial stages of northward subduction beneath southern Cyprus.	Evidence of southward migration of subduction front.
Kempler and Ben-Avraham (1987)	Eratosthenes Seamount suggested to be a continental fragment rifted from Africa.	Eratosthenes part of African Plate.
Garfunkel and Derin (1984)	Available data suggest Levant margin rifted in the Triassic, orthogonally and not by transform rifting.	Eastern Mediterranean Tethys is oceanic since the Triassic.
Makris et al. (1983)	Seismic refraction data suggest that both Eratosthenes and Cyprus are underlain by continental crust.	However, recently accepted to be on different plates.
Robertson and Woodcock (1979)	Eastern Mediterranean Sea seen a relict of Tethys ocean; Levant possibly rifted from Southern Turkey (Antalya) in Triassic.	Eastern Mediterranean oceanic since the Triassic.
Montadert et al. (1978)	Available seismic data suggest the Eratosthenes platform not covered by Messinian evaporite.	Eratosthenes as a raised edifice in the Messinian?
Robertson (1977)	Initial synthesis of tectonic uplift of the Troodos ophiolite since the Upper Cretaceous; driving force serpentinite diapirism and tectonic collision.	Rapid uplift of southern Cyprus in Plio-Pleistocene.
Woodside (1977)	Single channel seismic survey of the Eratosthenes platform reveals reflective unit below relatively transported unit; seamount is faulted; sediment-filled basin to north.	Subduction trench to the north visible with benefit of hindsight.
Ben-Avraham et al. (1976)	Eratosthenes is a large deep-seated structure, large magnetized feature at depth larger than, and displaced relative to, the bathymetric high; paleomagnetic pole at $\sim 27^\circ N$.	Basic igneous material at depth; platform evolved with Africa.
Finetti and Morelli (1973)	Eratosthenes platform is a major edifice with Tertiary or Mesozoic reflectors dipping beneath the inferred base Messinian.	Eratosthenes emergent during Messinian?
Giermann (1969)	Identified major north-dipping fault to north of Eratosthenes Seamount Giermann Fault.	This fault now seen as effective trace of downgoing Eratosthenes slab.
Gass and Masson-Smith (1963)	Cyprus ophiolite uplift driven by underthrusting of the continental margin of North Africa.	Far-sighted inference of continental collision as cause of Cyprus uplift.



(a)



(b)

FIGURE 1.5: (a) Cross-section through the ESM from Robertson (1998b); (b) compilation of 1-D P-wave velocity models from different wide-angle seismic investigations.

Chapter 2

Methods

2.1 Introduction to Seismic Waves

Seismic waves have been used for studying Earth's subsurface for about 100 years. The composition and characteristics of inner Earth were deduced from studying seismic waves transmitted from natural (passive: earthquakes) and human made sources (controlled-source: explosions, airgun shots). Seismic surveys reveal the distribution of seismic velocities and interfaces between rock units ([Levander et al., 2010](#)).

Seismic Wave Velocities

Generally the seismic velocities (V_p - compressional-wave velocity, V_s - shear-wave velocity) depend on the elastic moduli and density of the rock:

$$V_p = \sqrt{\frac{K + 4/3\mu}{\rho}} \quad V_s = \sqrt{\frac{\mu}{\rho}} \quad (2.1)$$

where K is the bulk modulus ($=1/\text{compressibility}$), μ is the shear modulus and ρ is the density ([Mavko et al., 2009](#)).

Empirical ranges of compressional or P-wave velocities through different lithologies have been investigated by numerous authors (e.g. [Christensen and Mooney, 1995](#); [Birch, 1966](#); [Sheriff and Geldart, 1982](#); [Bourbié et al., 1987](#)) and are summarized in Fig. 2.1.

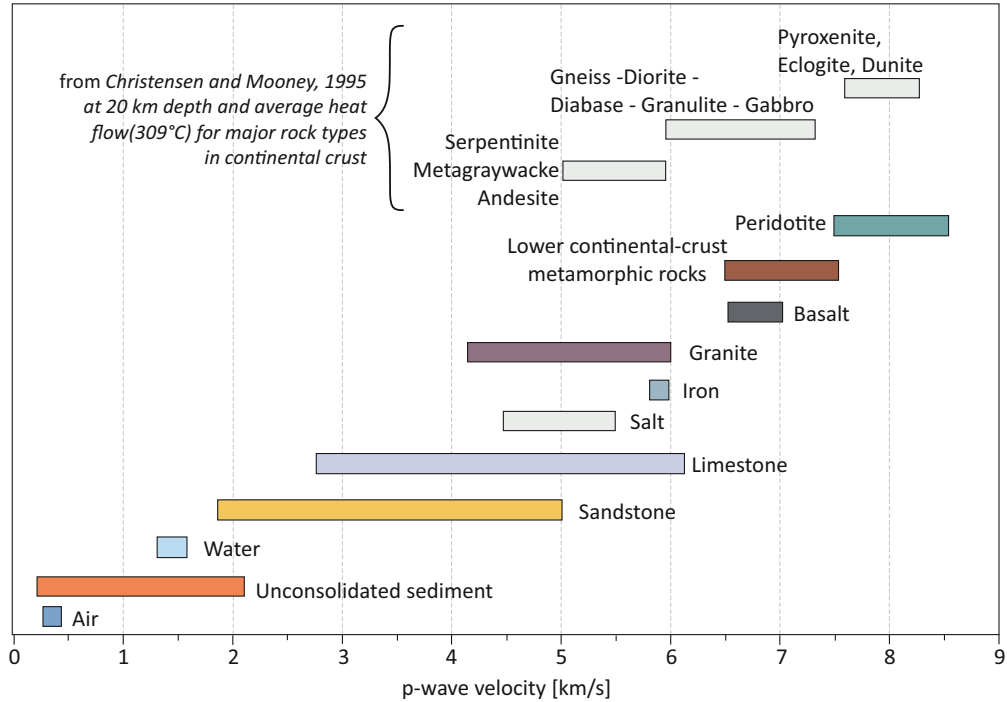


FIGURE 2.1: Average seismic velocities of different rock types, modified after Sheriff and Geldart (1982); Bourbié et al. (1987); Christensen and Mooney (1995)

Ray Theory

When a seismic ray strikes an interface between two rocks (marking a change in seismic velocity), *Snell's law* describes the relationship between the seismic ray path and the seismic velocities of the layers (Fig. 2.2):

$$\frac{\sin i}{v_1} = \frac{\sin i'}{v_2} = p \quad (2.2)$$

where i is the angle of the incident and reflected wave, i' the angle of the refracted wave, v_1 is the velocity in the layer in which the wave is incident and reflected and v_2 is the velocity in the layer in which the wave is refracted. p is called the *seismic parameter*, *ray parameter* or *horizontal slowness* (Lay and Wallace, 1995).

The geometry of the seismic source, subsurface structure and receiver location define the seismic ray paths through the inner Earth. Exemplified by a two layer medium (Fig. 2.2) where $v_2 > v_1$, three types of seismic rays are observed at the surface (Lay and Wallace, 1995):

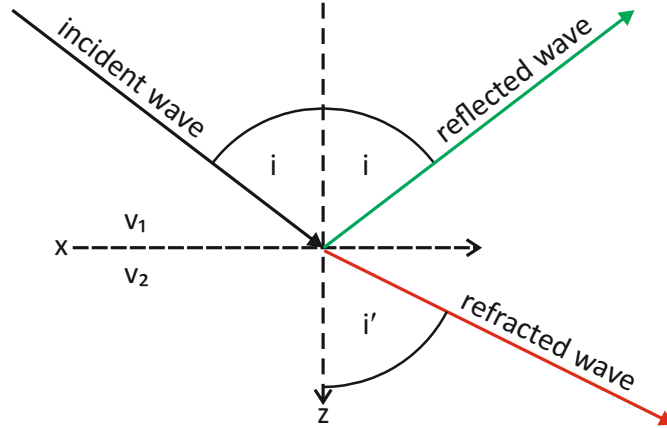


FIGURE 2.2: Schematic sketch showing the principles of Snell's Law

- the **direct wave** (blue line in Fig. 2.3), propagates along the atmosphere-upper layer boundary and its travel time is given by

$$T_{dir} = \frac{X}{v_1} \quad p = \frac{1}{v_1} \quad (2.3)$$

where X is the distance.

- the **reflected wave** (green line in Fig. 2.3), the travel time of which is given by

$$T_{refl} = \frac{2h_1}{\cos i * v_1} \quad (2.4)$$

where h_1 is the thickness of the upper layer.

- the **head wave** (red line in Fig. 2.3). Assuming $v_2 > v_1$ and $i' \rightarrow 90^\circ$, Snell's law predicts a so called *critical refraction*.

$$\frac{\sin i_c}{v_1} = \frac{\sin 90^\circ}{v_2} \quad (2.5)$$

where the incident angle (i) is equal to the *critical angle* i_c . In this case the refracted wave travels as a head wave horizontally immediately below the layer boundary (see Fig. 2.3; Lay and Wallace, 1995). The critical angle is defined as

$$i_c = \sin^{-1}(v_1/v_2) \tag{2.6}$$

The travel time of the head wave is given by

$$T_{refr} = \frac{r}{v_2} + \frac{2h_1}{\cos i_c * v_1} \tag{2.7}$$

where r is the traveled distance of the refracted wave along the layer boundary and i_c the critical angle. The intercept time T_0 is given by

$$T_0 = \frac{2h_1}{v_1} * \sqrt{1 - \frac{v_1^2}{v_2^2}} \tag{2.8}$$

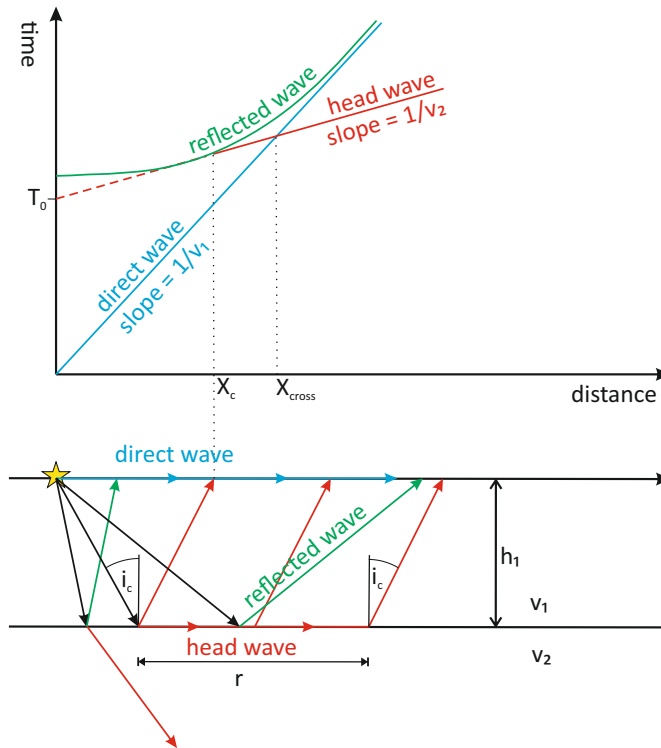


FIGURE 2.3: Traveltime curve and seismic phases and ray paths

As shown in Fig. 2.3 different types of seismic phases occur which provide different types of information about the subsurface. Reflected seismic waves are particularly used for imaging the subsurface in terms of contrasts in seismic impedance, the product of seismic

velocity v and density ρ (see Eq. 2.26). Thus the reflected wavefield is directly used to form an image of the *reflectivity structure* of the subsurface (Levander et al., 2010).

In contrast to this, **wide-angle methods** rely on the identification of first arriving refracted waves (measuring the traveltimes) which gives direct evidence for seismic velocities and layer thicknesses. Subsequently this information is used to derive a velocity model of the subsurface.

The two conventional controlled-source methods lead to two different end members (Levander et al., 2010):

- reflected data provide a high-resolution structural image,
- whereas wide-angle data provide a lower-resolution velocity model.

The following chapter presents the methods which were used to obtain a P-wave velocity model of the subsurface. Figure 2.4 shows a simplified workflow from the raw data to the P-wave velocity model using

- a) the method of inverting the data, which is used in this study to produce the **laterally heterogeneous P-wave velocity model** (traveltime tomography) beneath Cyprus and offshore south of Cyprus and
- b) the method of manual fitting of the data to obtain a **layered P-wave velocity model** (*trial-and-error forward modelling*) beneath South Turkey.

2.2 Model Parameterization

As shown in Fig. 2.4 the model parameterization is part of both methods, the *trial-and-error forward modelling* (chapter 2.3) and the *traveltime tomography* (chapter 2.4).

Velocity variations may be defined by a set of interfaces whose geometry is varied to satisfy the data, a set of constant velocity blocks (Fig. 2.5a) or nodes with a specified interpolation function (Fig. 2.5b), or a combination of velocity and interface parameters (Rawlinson, 2000).

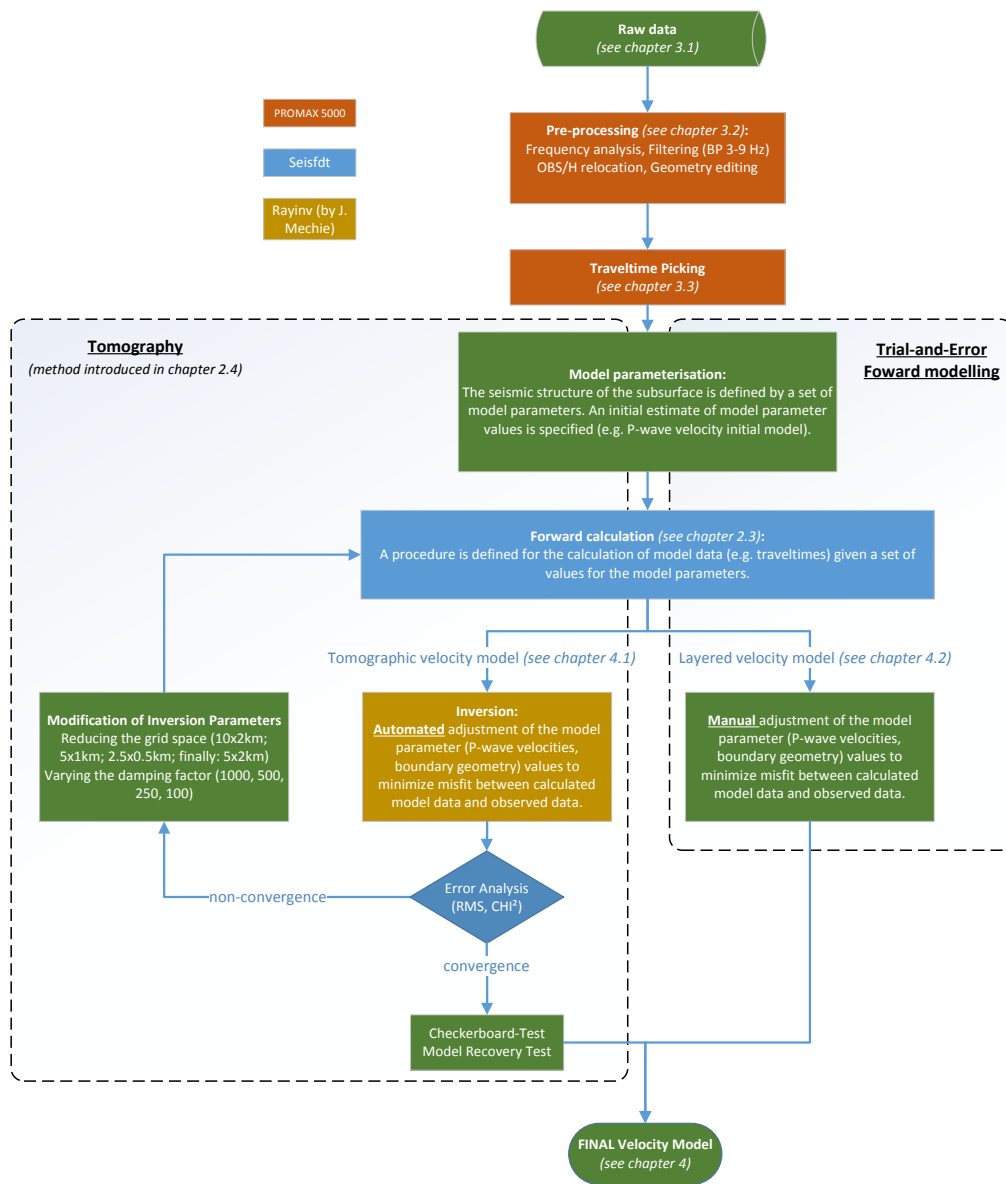


FIGURE 2.4: Wide-angle seismic data workflow

In this study the velocity distribution is described by irregular blocks or grid nodes following the method of Červený et al. (1977) (rectangular blocks) which is similar to the method of Zelt and Smith (1992) (trapezoidal blocks). In the method of Zelt and Smith (1992), the velocity field is discretised into a series of trapezoidal blocks, with four corner vertices used to specify the velocity within the block (see Fig. 2.5d). The P-wave velocity v_p within each trapezoid is given by Zelt and Smith (1992):

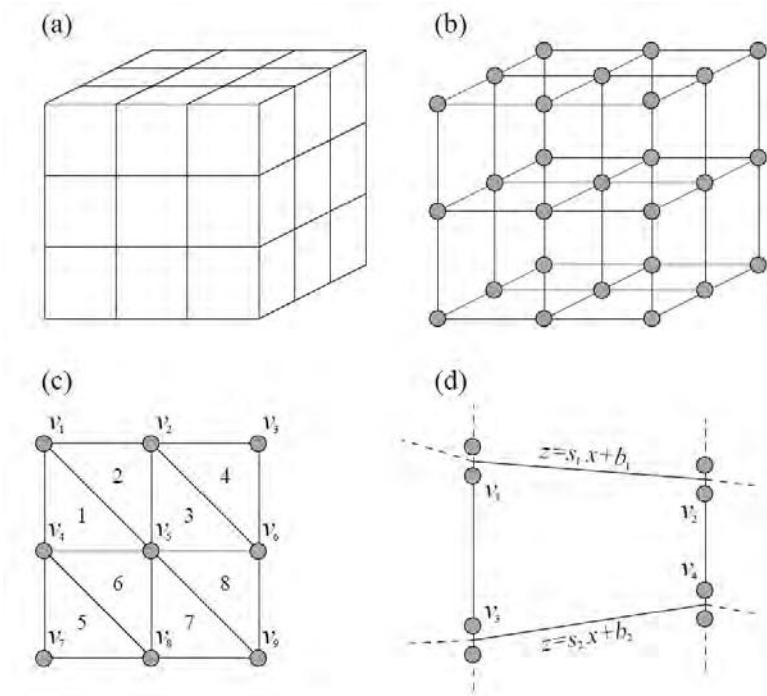


FIGURE 2.5: Different types of velocity parameterisation (after [Rawlinson, 2000](#)): (a) constant velocity blocks, (b) a grid of velocity nodes, (c) triangulated velocity grid designed for constant velocity gradient cells (after [White, 1989](#)), (d) velocity defined by a trapezoidal block (after [Zelt and Smith, 1992](#)). The four corner vertices labelled v_1 to v_4 define the velocity within the block. If adjacent nodes in vertically adjacent blocks are the same, velocity will be vertically continuous. If not, then a sub-horizontal interface will be defined

$$v_p(x, z) = \frac{c_1x + c_2x^2 + c_3z + c_4xz + c_5}{c_6x + c_7} \quad (2.9)$$

where the coefficients c_i are linear combinations of the corner velocities v_i ([Zelt and Smith, 1992](#)). If instead of trapezoids, rectangles are used as in the case of the method of [Červený et al. \(1977\)](#), then equation 2.9 is somewhat simplified as s_1 and s_2 (see Fig. 2.5(d)) are zero and consequently c_2 and c_6 (see Eq. 2.9) are zero too. Due to the flexibility of this technique a velocity structure with or without layering can be represented. If layers are present, it is possible for the velocity within the layers to vary arbitrarily.

2.3 Forward Modelling

The calculation of ray traveltimes between known end points (source and receiver) through a given velocity structure is often called the forward problem or forward modelling (Rawlinson and Sambridge, 2003).

The traveltime of a seismic wave along a ray path L is given by the integral for a continuous velocity field $v(x, z)$ as

$$t = \int_L \frac{1}{v(x, z)} dl \quad (2.10)$$

where dl is the differential path length (Zelt and Smith, 1992).

In the ray theory, kinematic wave propagation is described by the eikonal equation

$$(\nabla T)^2 = s^2 \quad (2.11)$$

where $s(x)$ is the slowness of the medium ($1/v$) and $t(x)$ represents the arrival time of a wavefront at point x (Podvin and Lecomte, 1991). The eikonal equation is an approximation of the wave equation that assumes seismic wavelengths are small compared to the fractional change in velocity gradient in the medium (Lay and Wallace, 1995). Thus the eikonal equation is a high-frequency approximation of the wave equation.

Two classical, ray-based approaches to determine ray traveltimes are the *shooting* (e.g. Zelt and Smith, 1992) and *bending* method (Julian and Gubbins; 1977 Um and Thurber 1987). In practice, shooting methods are more efficient and sufficiently robust for 2-D models, whereas bending methods are favored for 3-D models (Levander et al., 2010).

In the late 1980s a new forward modelling approach was introduced in which first-arrival traveltimes are calculated on a fine grid using a finite-difference solution of the eikonal equation (Vidale, 1988; Podvin and Lecomte, 1991; Schneider et al., 1992). This method has become very popular and is collectively known as the wavefront tracking method or eikonal solver (Levander et al., 2010). The scheme is based on a progressive integration of the traveltimes along an expanding square grid of velocity nodes in 2-D.

The propagation of two-dimensional wavefronts is defined by the 2-D eikonal equation

$$\left(\frac{\partial T}{\partial x}\right)^2 + \left(\frac{\partial T}{\partial z}\right)^2 = s(x, z)^2 \quad (2.12)$$

where $s(x, z)$ is the slowness field and $T(x, z)$ is the traveltime of a propagating wave (Vidale, 1988).

The method of Vidale (1988) is formulated for a structure defined by a square grid of velocity points (see Fig. 2.6). Assuming A is the source point, the traveltime of the four points adjacent to the source ($B_1 - B_4$) is given by

$$t_{B_i} = t_0 + \frac{h}{2}(s_{B_i} + s_A) \quad (2.13)$$

where h is the mesh spacing, s_A the slowness at the point A , and s_{B_i} is the slowness at the grid point B_i . t_0 gives the traveltime at point A . For the initial calculation, t_0 is zero since it is the traveltime of the source grid point (A), but in general t_0 is not zero and A is not restricted to be the source point (Vidale, 1988).

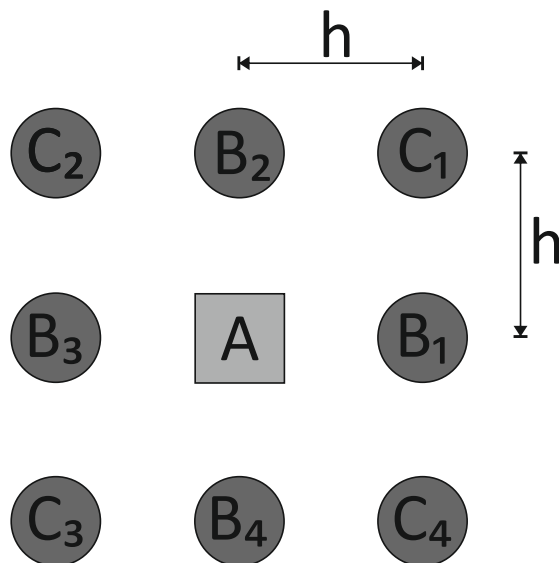


FIGURE 2.6: Square grid of velocity nodes used by the method of Vidale (1988), A is the source grid point and h is the mesh spacing.

Once the traveltimes t_{B_1} and t_{B_2} are known, the traveltime for the grid node C_1 is determined from the eikonal equation by approximating the two differential terms in Equation 2.12 with finite differences as

$$\frac{\partial t}{\partial x} = \frac{1}{2h} (t_0 + t_{B_2} - t_{B_1} - t_{C_1}) \quad (2.14)$$

and

$$\frac{\partial t}{\partial z} = \frac{1}{2h} (t_0 + t_{B_1} - t_{B_2} - t_{C_1}) \quad (2.15)$$

Substituting equations 2.14 and 2.15 into equation 2.12, the traveltime to point C_1 can be written as

$$t_{C_1} = t_0 + \sqrt{2(hs)^2 - (t_{B_2} - t_{B_1})^2} \quad (2.16)$$

With this scheme it is possible to calculate the traveltimes to all corner grid nodes (C_i). Equation 2.16 gives the traveltime to point C_1 using the traveltime from the source to the points A (t_0), B_1 (t_{B_1}) and B_2 (t_{B_2}) in a plane wave approximation, where the point A does not need to be the source point. This approximation will be most accurate for nearly flat wavefronts. For strongly curved wavefronts Vidale (1988) approximates the traveltimes assuming locally circular wavefronts. Following a specified scheme described by Vidale (1988) the square where traveltimes are already calculated (Fig. 2.6) is extended by a ring of grid nodes where the traveltimes are unknown (a 3x3 grid becomes a 5x5 grid).

The basic scheme proposed by Vidale (1988, 1990) remains popular and has been improved by several authors (Hole and Zelt, 1995; Koketsu et al., 2000; Podvin and Lecomte, 1991; van Trier and Symes, 1991; Schneider et al., 1992).

The advantage of finite-difference methods is that they find the fastest ray between any two points, including the diffracted path in the case of a geometrical shadow zone, and they can be very efficient, especially for 3-D (Levander et al., 2010).

With the method of forward modelling, the velocity and interface structure of the subsurface can be revealed by the so called trial-and-error forward modelling. This scheme involves a manual, iterative adjustment of the calculated traveltimes to fit the observed traveltimes. This procedure was performed for the onshore part (S. Turkey - Cyprus) of the wide-angle profile (see Fig. 2.4 and Chapter 4.2).

2.4 Traveltime Tomography / Inversion

Controlled-source seismic tomography is nowadays a widely used technique for investigating the Earth's crust and lithosphere. There are two main types of seismic data which can be inverted: traveltime data (Hole et al., 1992; Zelt and Barton, 1998; Zelt, 1999; Imbrota et al., 2002; Hobro et al., 2003) and waveform data (Tarantola, 1984; Pratt et al., 1996; Ravaut et al., 2004). Traveltime tomography is typically much more robust, easier to implement, and computationally much cheaper, whereas waveform tomography reconstructs the Earth's velocity structure with much higher resolution. Nevertheless the inversion of seismic traveltime data is the primary technique to achieve a reliable and smooth velocity model of the Earth (Tikhotsky and Achauer, 2008).

Traveltime tomography is the main method by which the Earth's seismic velocity structure is determined on all scales, from the upper few meters to the whole mantle. It was adapted from algorithms used in medical imaging in the 1970s (Dziewonski and Anderson, 1984). The word *tomography* literally means *slice picture* (from the Greek word *tomos* meaning *slice*) and was first used in medical imaging to describe the process of mapping the internal density distribution of the human body using x-rays (Lee and Pereyra, 1993).

The advantages of inversion compared to trial-and-error forward modelling includes

- 1.) providing estimates of model non-uniqueness by exploring model structure thoroughly to better understand what structure is required by the data and what structure is consistent with the data,
- 2.) resolving small scale structures,
- 3.) quantifying model errors and resolution,
- 4.) handling larger datasets.

Following the ray-tracing described in chapter 2.3 a 2-D traveltime inversion (Zelt and Smith, 1992; Zelt and Barton, 1998) is performed to determine the velocity model, including the uncertainty and resolution of the estimated parameters. With, for example, the Zelt and Smith (1992) algorithm an irregular grid of velocity and interface nodes can be used, and any type of refracted or reflected arrival can be inverted simultaneously

for velocity and interface geometry. Today, this type of 2-D and 3-D traveltime inversion and tomography are the central analysis methods applied to crustal wide-angle data (Levander et al., 2010).

Formulation

If some elastic properties of the subsurface (e.g. velocity structure) are represented by a set of model parameters \mathbf{m} , then a set of data (e.g. traveltimes) \mathbf{d} can be predicted for a given source-receiver array by line integration through the model. The relationship between data and model parameters

$$d = g(m) \tag{2.17}$$

where $g(m)$ is the model prediction, forms the basis of any tomographic model.

As schematically shown in figure 2.4 the main parts of a seismic tomography workflow are

- **Model parameterization:** Based on the fundamental relationship between predicted data and model parameters (Eq. 2.17) it is necessary to represent variations in subsurface structure by a set of model parameters \mathbf{m} (e.g. seismic velocities) to compute the model predictions $g(m)$ (introduced in Chapter 2.3).
- **Forward calculation** (see chapter 2.3): prediction of model data \mathbf{d} (e.g. traveltimes) for the given model parameters
- **Inversion:** Automated adjustment of the model parameters \mathbf{m} to minimize misfit between model data \mathbf{d} and the observed data
- **Error Analysis:** investigate solution robustness

Three basic approaches of tomography are defined (Rawlinson and Sambridge, 2003) as

- **linear tomography:** the relationship between traveltime residual and velocity perturbation is linearized about a reference model. Ray paths are determined once and are not re-traced

- **iterative non-linear tomography**: this is also a linearization, but accounts for the non-linearity (ray path dependence on the velocity correction) of the problem by iteratively applying corrections and re-tracing rays until the data are satisfied, or the rate of data fit improvement per iteration satisfies a given tolerance.
- **fully non-linear tomography**: locates a solution without relying on linearization in any way, but is rarely done in practice.

Consequently the tomography technique introduced and applied in this study is defined as an iterative non-linear tomography.

Inversion

The inverse step involves the adjustment of the model parameters m to satisfy the observed data d_{obs} through the known relationship (Eq. 2.17).

The discrete form of equation 2.10

$$t = \sum_{i=1}^n \frac{l_i}{v_i} \quad (2.18)$$

is used in practical applications, where l_i and v_i are the path length and velocity of the i th ray segment, respectively. Therefore traveltime is a linear combination of slowness, whereas traveltime inversion is a non-linear problem since the ray path is velocity dependent (Zelt and Smith, 1992).

The linearized equation based on the assumption of neglecting higher-order terms is

$$d = Gm \quad (2.19)$$

where d is the traveltime residual vector, m is the model update parameter adjustment vector (e.g. velocity nodes, interface depths) and G is the partial derivative matrix. The matrix of partial derivatives contains the elements $\frac{\partial t_i}{\partial m_j}$, where t_i is the i th observed traveltime and m_j is the j th model parameter selected for inversion, either a velocity value or the z coordinate of a boundary node (Zelt and Smith, 1992). The dimension

of G is defined by $M \times N$ where M is the number of data (e.g. seismic rays) and N is the number of model parameters (e.g. slowness nodes). The partial derivative of the j th velocity value is defined (see e.g. [Zelt and Smith, 1992](#)) as

$$\frac{\partial t}{\partial v_j} = \int_L -\frac{1}{v^2} \frac{\partial v}{\partial v_j} dl. \quad (2.20)$$

The partial derivatives associated with the boundary nodes are shown in the Appendix of [Zelt and Smith \(1992\)](#). The partial derivatives are generally calculated during the forward-modelling step, as a by-product of the ray-tracing.

To solve the inverse problem a full-matrix inversion is applied by performing a Gaussian elimination. The damped least-squares (DLS) solution can be written as

$$m = (G^T C_d^{-1} G + D C_m^{-1})^{-1} G^T C_d^{-1} d \quad (2.21)$$

where D is an overall damping factor and C_d and C_m are the estimated data and model covariance matrices given by

$$C_d = \text{diag} \{ \sigma_d^2 \}, \quad C_m = \text{diag} \{ \sigma_m^2 \} \quad (2.22)$$

After ray tracing, the parameter adjustment vector m is solved for and applied to the current model, after which rays are traced through the updated model. This procedure is repeated until a satisfactory fit to the observed data is achieved or a prescribed stopping criterion is satisfied ([Zelt and Smith, 1992](#)).

Error Analysis

A statistical analysis is carried out in order to quantify model errors.

The correction vector is calculated based on the damped least squares inversion and the model is updated iteratively until the difference between the calculated model response and the data is minimized. This difference is represented by the Root Mean Square

(RMS) traveltime residual and the traveltime misfit χ^2 (*chi-square*), which should have a value of almost one. This value indicates the capability of the data to resolve small-scale heterogeneities within the model. Other factors that may contribute to a final χ^2 value greater than one are (1) significant out-of-plane structural and velocity variations, (2) deviations of the shot-receiver geometry from a straight line, (3) some of the picks identified as P_g arrivals were non-geometrical arrivals (i.e. they were diffractions associated with a shadow zone or low-velocity body), and (4) the errors in the traveltime data were significantly under-estimated (Zelt and Smith, 1992).

The chi-squared statistic is defined as

$$\chi^2 = \sum_{j=1}^M \left(\frac{R_j}{\sigma_j} \right)^2 \quad (2.23)$$

where R_j is the traveltime residual and σ_j the traveltime uncertainty. The traveltime residual is defined as

$$R_j = \Delta t = d_j - F_j \quad (2.24)$$

where d_j is the data ("observed mean"), F_j is the model ("predicted mean").

The reduced chi-square statistic is defined as

$$\chi^2 = \frac{\chi^2}{N - 1} \quad (2.25)$$

where N is the number of observations (number of rays).

2.5 Synthetic Seismogram Computation

During the forward modelling by ray tracing, theoretical travel times are calculated based on the derived velocity model. These traveltimes are later displayed with the recorded data and the observed or picked travel times. With this method it is possible to directly compare the resulting traveltimes of the real velocity model and the derived velocity model and to perform a subsequent estimation of the misfit between both velocity models

for each record section. To enhance this misfit estimation and to extract more information from the data, it is necessary not just to compare travel times but also to use the amplitudes of the phase arrivals. For this reason theoretical seismograms were calculated using the finite-differences method which is introduced in the following section. Based on these synthetic seismograms it is now possible to compare traveltimes in combination with the amplitude of the wavelet which leads to a much more comprehensive estimation of the misfit between the real and derived velocity structure.

As shown by [Sheriff \(1975\)](#) propagation of seismic energy in the Earth is a complex phenomenon. Nevertheless one major factor which affects directly the amplitude of the seismic wave is the *reflection coefficient* defined as

$$R_c = \frac{V_{p2}\rho_2 - V_{p1}\rho_1}{V_{p2}\rho_2 + V_{p1}\rho_1} = \frac{AI_2 - AI_1}{AI_2 + AI_1} \quad (2.26)$$

where AI is the acoustic impedance defined by the product of seismic velocity V and bulk density ρ ([Sheriff, 1975](#)). The numbers 1 and 2 of equation 2.26 refer to the upper and lower layer, respectively (as shown in Fig. 2.3). Effectively, the amount of reflected energy determines how much energy can be transmitted through a section. The transmitted energy is described by the *transmission coefficient* T ([Simm and Bacon, 2014](#))

$$T = \frac{2AI_1}{AI_2 + AI_1} \quad (2.27)$$

With this relationship it is shown that less energy is transmitted through a boundary with high acoustic impedance contrast, which leads to an observed higher amplitude of the reflected seismic wave. Adjusting the velocity contrast at layer boundaries is one of the main approaches to minimize the misfit between the observed and theoretical amplitudes of the seismic phases.

To compute synthetic seismograms in this study the finite-difference (FD) method introduced by [Kelly et al. \(1976\)](#) is applied. This method propagates complete seismic wave fields through a two-dimensional grid with arbitrarily complex variations in material properties. It produces synthetic seismograms for any point on the grid and includes direct waves, all primary and multiply reflected waves, surface waves, head waves, converted waves, diffractions and critically refracted waves.

The finite-difference technique not only provides reliable arrival times, but also accounts for the variations in signal amplitude with subsurface elastic impedance contrast and range (Kelly et al., 1976).

The FD method uses the computer power to solve the wave equation over a discrete set of grid points or model parameters. The FD calculation could be parallelized very efficiently, taking advantage of the large number of modern CPUs (Ryberg et al., 2000).

The elastic wave equation describes the temporal and spatial development of the wave field in an elastic solid body for the vertical (U) and horizontal (W) component (Kelly et al., 1976) :

$$\rho \frac{\partial^2 U}{\partial t^2} = \frac{\partial}{\partial x} \left[\lambda \left(\frac{\partial U}{\partial x} + \frac{\partial W}{\partial z} \right) + 2\mu \frac{\partial U}{\partial x} + \frac{\partial}{\partial z} \left(\mu \frac{\partial W}{\partial x} + \frac{\partial U}{\partial z} \right) \right] \quad (2.28)$$

$$\rho \frac{\partial^2 W}{\partial t^2} = \frac{\partial}{\partial z} \left[\lambda \left(\frac{\partial U}{\partial x} + \frac{\partial W}{\partial z} \right) + 2\mu \frac{\partial W}{\partial z} + \frac{\partial}{\partial x} \left(\mu \frac{\partial W}{\partial x} + \frac{\partial U}{\partial z} \right) \right] \quad (2.29)$$

where μ and λ are the elastic constants, which describe the elastic properties of the model and ρ is the density. To solve the equations 2.28 and 2.29 numerically, the partial derivatives are replaced by their finite difference equivalents (Ryberg et al., 2006) :

$$U_{i,j}^{n+1} = F \left(U_{i,j}^{n-1}, U_{i,j}^n, U_{i\pm 1,j}^n, U_{i,j\pm 1}^n, W_{i\pm 1,j\pm 1}^n \right) \quad (2.30)$$

where $U_{i,j}^n$ represents the vertical component for the n -th time step at the location i, j and F is a simple linear function of their arguments with coefficients which depend on the local value of μ and λ . Equation 2.30 gives the rule to calculate the $n + 1$ time step of $U_{i,j}$ from its past values $U_{i,j}^n$ and $U_{i,j}^{n-1}$ and from the spatial neighbors $U_{i\pm 1,j\pm 1}^n$ and $W_{i\pm 1,j\pm 1}^n$. A similar scheme is defined for $W_{i,j}^{n+1}$

$$W_{i,j}^{n+1} = F' \left(W_{i,j}^{n-1}, W_{i,j}^n, W_{i\pm 1,j}^n, W_{i,j\pm 1}^n, U_{i\pm 1,j\pm 1}^n \right) \quad (2.31)$$

Both equations 2.30 and 2.31 can easily and efficiently be calculated on a parallel computer system (Ryberg et al., 2006).

Chapter 3

Seismic Data and Processing

3.1 Data Acquisition

The data were collected along a 650 *km* long N-S trending amphibian profile, running from the Tuz Gölü basin in the north to the Eratosthenes Seamount (ESM) in the south, crossing Cyprus (Fig. 3.1(a)). The profile consists of an offshore part (South of Cyprus, ESM) and an onshore part (Cyprus, South Turkey). The offshore and the onshore survey were performed at the same time to achieve an amphibian connection between both parts. The airgun shots of the offshore survey were also recorded by the stations onshore Cyprus.

Offshore

The offshore wide-angle data were acquired with the research vessel Maria S. Merian during the cruise MSM14 leg 3 during the period from 12.03.2010 to 05.04.2010. Besides shallow reflection seismic, magnetic, magnetotelluric, gravity and hydroacoustic measurements this survey involves four wide-angle reflection / refraction profiles (WARRPs) where the WARRP 27 is the offshore part of the amphibian profile presented in this study (station location is shown in Fig. 3.1(a) and Table A).

For data recording 34 ocean bottom seismometers (OBS) and hydrophones (OBH) were deployed. 19 of these were Canadian ocean bottom seismometers from Dalhousie University. The sensors comprise a 3-component 4.5 *Hz* geophone and an OAS E-2SD

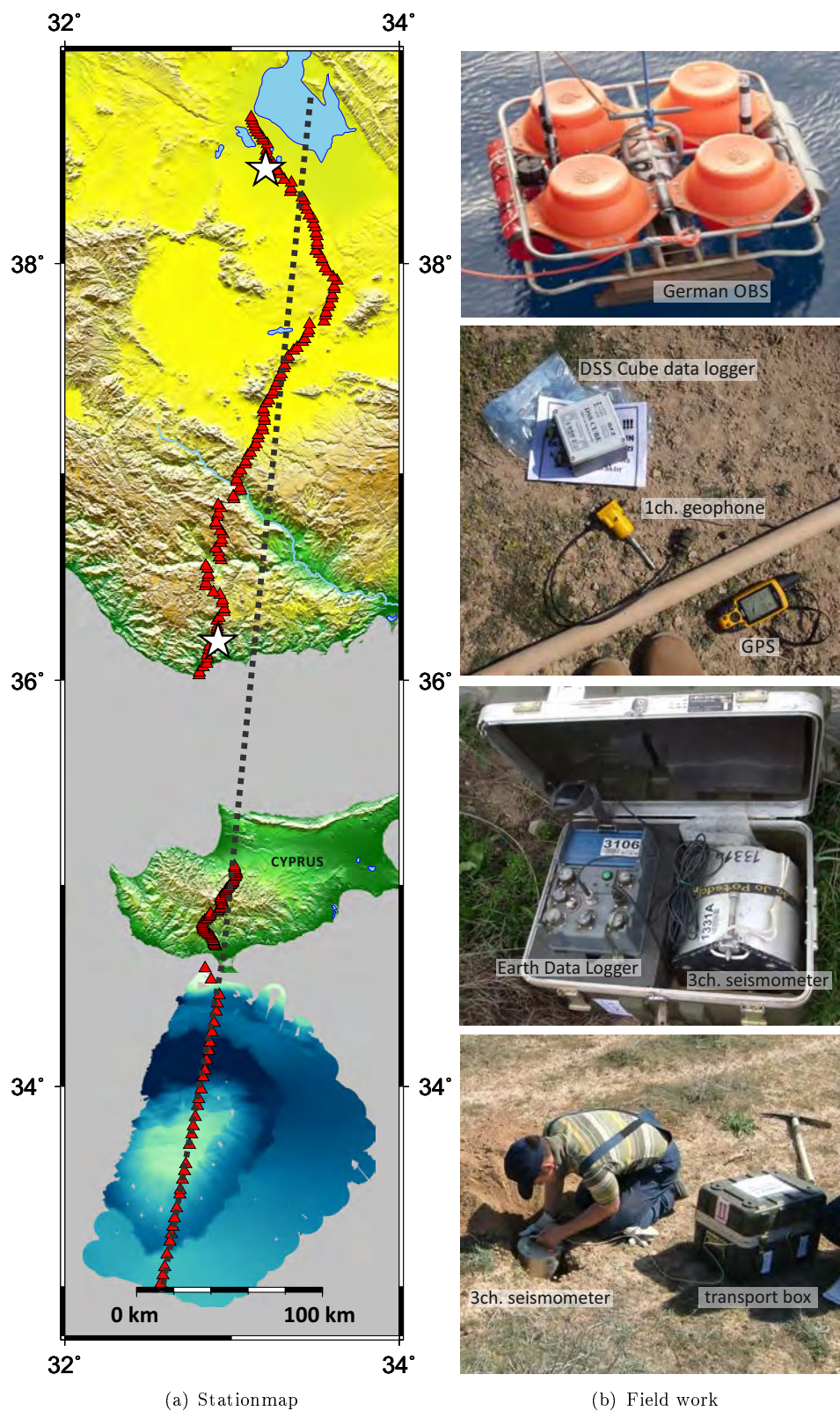


FIGURE 3.1: (a) Map view of stations (red triangles) and land shots (white stars), where the dashed black line is the defined profile line and (b) pictures of field work.

hydrophone. The other 15 stations (10 OBS and 5 OBH) were German instruments consisting of LE-1D/V seismometers, HTI-04-PCA/ULF hydrophones and a Geolon MLS data logger. Accurate time is ensured by synchronizing the internal clock with the GPS time signal before deploying and after recovery and an elimination of the linear time shift if necessary.

6 BOLT airguns (2 x 700 in^3 , 2x 1000 in^3 and 2 x 1900 in^3) with a total volume of 120 liters were used as the seismic source. The survey geometry set-up is shown in Fig. 3.2. The air guns were shot directly along the profile where the stations were deployed previously. Shots were fired at a pressure of 120 *bar* with a shot interval of 60 *s*, resulting in a shot distance of approximately 120 *m* at a ship's speed of 4 *kn* over ground. Synchronization and triggering were done by the SureShot trigger system (Hübscher, 2012).

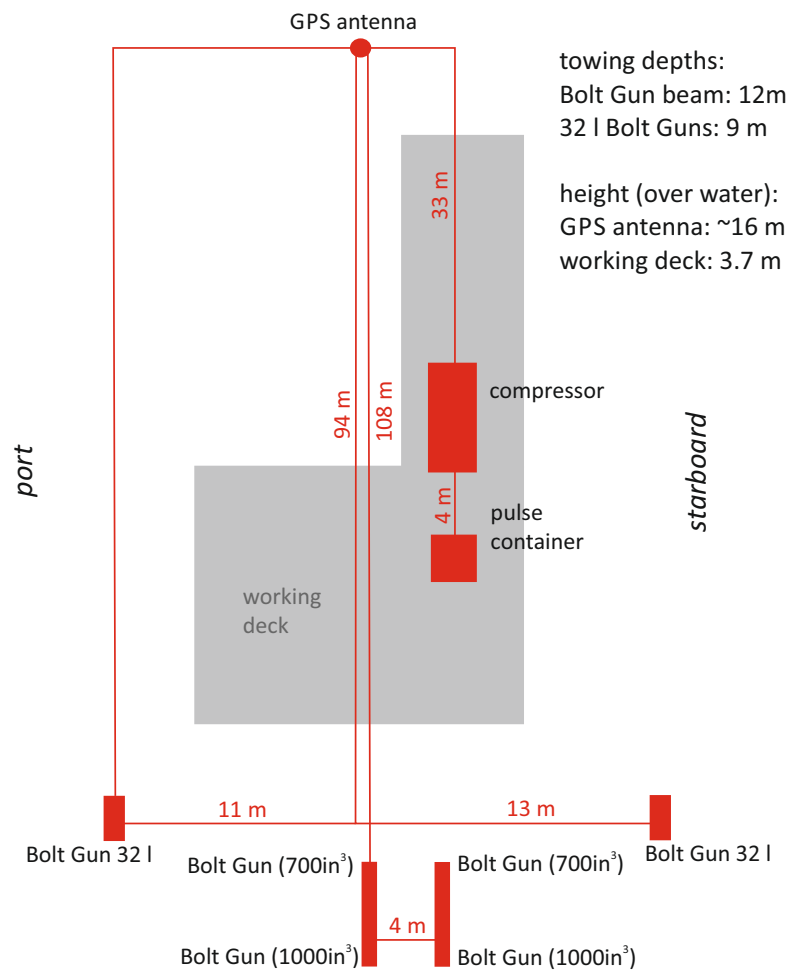


FIGURE 3.2: Schematic sketch showing the survey geometry for wide-angle profile WARRP27 (after Hübscher, 2012)

After shooting, all deployed ocean bottom instruments were recovered by submitting an acoustic release signal by a 12.5 *kHz* transducer. The uplift of the stations was ensured by glass spheres for buoyancy (orange buoyancy chamber in Fig. 3.1(b)). Due to technical problems station 15 recorded no data and was rejected from further processing.

TABLE 3.1: Summary of the wide-angle survey (offshore part)

source	1520 airgun shots (Bolt airguns, total volume 120 <i>l</i>)
receiver	34 ocean bottom seismometers and hydrophones
instrumentation	3-component 4.5 <i>Hz</i> geophone, LE-1D/V seismometer and hydrophones
sampling rate	OBH = 50 <i>sps</i> , OBS = 200 / 250 <i>sps</i>
shot spacing	120 <i>m</i> (every 60 seconds)
receiver spacing	~ 5 <i>km</i>

Onshore

During the period from 23.03.2010 to 06.04.2010 246 land stations were deployed. 50 stations (station numbers C201 to C250) were deployed on Cyprus and 196 in south Turkey (T1 - T185, T187-T196 and T256 which has the same location as T56). All station locations, including elevations and sampling rates are shown in Table A.

102 stations were equipped with an Earth Data Logger (EDL) and a 3 channel Mark 1 *Hz* seismometer or 3 channel 4.5 *Hz* geophone. 84 stations consisted of a DSS Cube data logger and a 1 channel 4.5 *Hz* Geophone. This instrumentation was provided by the Geophysical Instrument Pool Potsdam, GIPP (instrumentation and deployment shown in Fig. 3.1(b)). 60 stations were REFTEK Texan instruments from Bogazici University in Istanbul (shown by "tXXXX" as station type in Table A). The exact time for the recordings is transmitted by an internal GPS for the Cube and EDL stations. Due to the fact that the Reftek Texans have no internal GPS, they are synchronized before and after the deployment to GPS, as for the offshore stations, and then a linear drift correction is applied. Due to political reasons it was not possible to deploy stations in the Turkish part of Cyprus (northern part).

The average station spacing in Turkey was about 1.25 *km* and about 0.9 *km* in Cyprus. The EDL and Cube stations recorded the data with a sampling rate of 100 *sps*. The Texans instruments recorded the data at 125 *sps*. Due to technical problems station C221 recorded no data.

The seismic sources on land were two land shots each of 1125 *kg* seismic dynamite (locations shown as white stars in Fig. 3.1(a), T2001: southern land shot and T2002: northern land shot). Each shotpoint consisted of two boreholes with a depth of ~ 52 *m* and a diameter of 32 *cm*.

TABLE 3.2: Summary of the wide angle survey (onshore part)

source	2 land shots (seismic dynamite, each 1125 <i>kg</i>)
receiver	246 land stations (196 in S. Turkey and 50 in Cyprus)
instrumentation	1 ch 4.5 <i>Hz</i> geophone, 3 ch 1 <i>Hz</i> Mark seismometer or 3 ch 4.5 <i>Hz</i> geophone, Cube, EDL and REFTEK Texan as data logger
sampling rate	100 <i>sps</i>
receiver spacing	~ 1.25 <i>km</i> (Turkey) and ~ 0.9 <i>km</i> (Cyprus)

3.2 Data Preparation and Processing

The seismic data were processed with the seismic processing software Landmark ProMAX R5000. The data are stored in SEG-Y format. The processing of the data includes

- Visualization and examination of the data and meta-data.
- The exact location of each offshore receiver (OBS/OBH station) is determined based on the very first arrivals.
- The offsets of the traces are split into positive (to the south) and negative (to the north) values.
- For the ocean bottom seismometers the recordings of the hydrophone and Z-component of the seismometer are visually compared and the channel with the lower noise level is chosen for the further processing. In most cases this is the Z-component of the seismometer (see Table A).
- Water depths are added to the trace headers.

- For each trace an uncertainty is calculated based on the signal to noise ratio (S/N ratio). For the calculation of uncertainties an empirical relationship is defined:

$$S/N \leq 1 \Rightarrow error = 0.2 s \quad (3.1)$$

$$4 > S/N > 1 \Rightarrow error = \left[\frac{0.2}{S/N} \right] s \quad (3.2)$$

$$S/N \geq 4 \Rightarrow error = 0.05 s \quad (3.3)$$

- For the offshore stations and the stations on Cyprus an automatic gain correction (AGC) with an operator length of 5000 *ms* is applied, which automatically varies the gain applied to trace samples as a function of sample amplitude within an AGC time window.
- The amphibious profile line is defined for 2-D modelling. Based on the receiver locations the line is fitted by eye. The locations of receivers and land shots are projected onto this line and the distances of receiver and land shot locations from the northern end of the profile line is calculated (line is shown in Fig. 3.1(a) as a grey dashed line). Based on the geometry of the receivers and land shots the line is divided into two parts, namely a northern part for the onshore stations (Turkey to southern coast of Cyprus) and a southern part for the offshore stations (south of Cyprus). The line is defined by three coordinates:

TABLE 3.3: Coordinates of profile line

	lon [°]	lat [°]	distance from northern end [km]
northern point	33.47054382	38.78115193	0
middle point	32.94935194	34.65560303	460
southern point	32.57986184	32.96995052	650

Frequency Analysis

To reveal the dominant frequency content of the main signal, a frequency analysis was performed. The frequency content of all stations was analyzed by an interactive spectral analysis, which uses the Fourier Transform to compute and display the average power spectrum for an interactively selected subset of traces. Figures 3.3 and 3.4 show the frequency content of an OBS, exemplified by OBS03 and of an OBH, exemplified by OBH23, respectively.

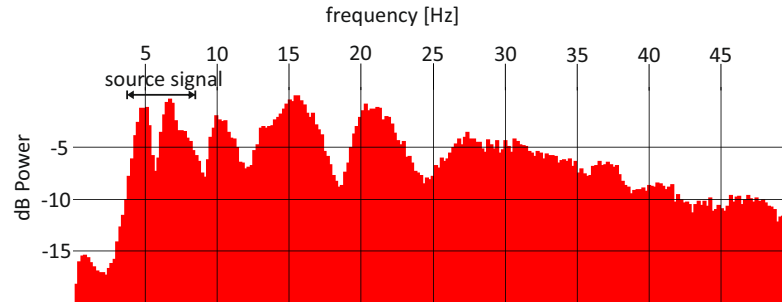


FIGURE 3.3: Frequency content of the OBS03

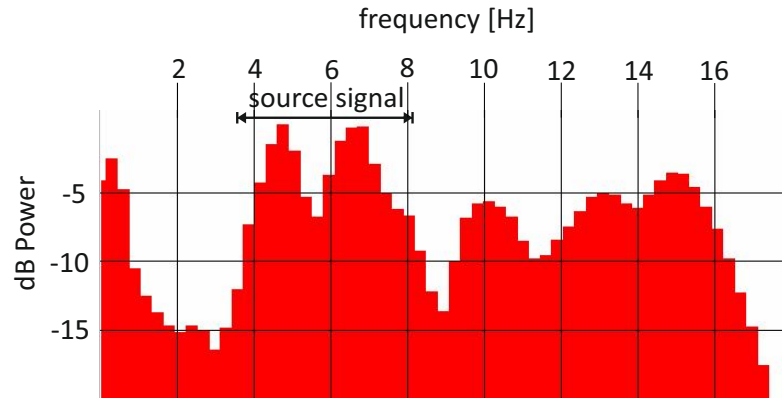


FIGURE 3.4: Frequency content of the OBH23

The analysis shows that the main content of the source signal is located in the frequency range of 3 to 9 Hz (marked in Fig. 3.3 and 3.4). The following frequency peaks (10, 15 and 20 Hz) are most likely due to the bubble pulse (oscillation) of the air gun source (Parkes and Hatton, 1986). The different frequency range of the OBS and OBH is explained by the different sampling rate of both instruments (250 sps and 50 sps). The frequency analysis shows the same result with the onshore stations on Cyprus.

Due to interfering frequencies recorded by the stations onshore Turkey a classical frequency analysis turned out to be difficult with the land shot data. Instead a set of filters with different frequency bands were applied to the data which is subsequently checked by eye. A bandpass filter with the frequency band of 4 – 8 Hz showed the highest signal to noise ratio and therefore is chosen as the filter for further processing of the land shot data.

Filtering

After obtaining a main frequency of 3 to 9 Hz for the offshore / on-offshore data and 4 to 8 Hz for the onshore data, the data are ready to be filtered to remove unwanted

frequencies (noise) and to improve the clarity of the display. For all wide-angle data a Butterworth bandpass filter was applied.

The Butterworth filter is defined by the frequencies at which the amplitude is down by 3 dB (70% or half power) and by the slope of the cutoff (Fig. 3.5, Telford et al. 1990). The slopes are specified in decibels per octave, where an octave corresponds to a change in frequency by a factor of two.

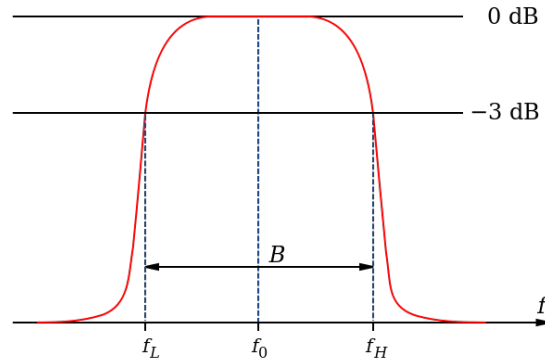


FIGURE 3.5: Butterworth bandpass filter

The parameters for the applied zero-phase bandpass filter were a 3 to 9 Hz pass-band (3 and 9 Hz represent the -3 dB points of the amplitude spectrum) for the offshore / on-offshore data and a 4 to 8 Hz pass-band for the onshore data with a 20 $db/octave$ low and high roll-off (slopes).

3.3 Traveltime Picking

After processing the data all visible arrivals of the airgun shots recorded by the offshore stations and stations on Cyprus (common receiver gathers, Figs. 3.7 to 3.12) were manually picked. The same procedure was performed for the land shots recorded by the land stations (common shot gathers, Figs. 3.13 to 3.16). The picked phases potentially include all refracted and reflected P-waves, especially the P_g^1 , PmP^2 and P_n^3 phases.

¹crustal refracted phase

²reflected phase at crust-mantle boundary (Moho)

³mantle refracted phase

Offshore and On-Offshore

The offshore and on-offshore data (airgun shots recorded by the Cyprus stations) show a good data quality with a clear onset of the first arrival almost along the whole offshore part (190 km, see Fig. 3.7). On the recordings of the station onshore Cyprus an area with low S/N ratio of the first arrival between 70 and 130 km offset is observed (red dashed area in Fig. 3.11). In this segment it was not possible to pick a clear first arrival at some stations. Note that on the seismogram section of OBS02 (red dashed area in Fig. 3.7) a similar feature is observed for the same area.

Stations C222 and C241 show very noisy data along the whole profile, so no first arrivals were picked. C221 had technical problems and recorded no data. Thus, finally 47 of the 50 stations were appropriate for picking first arrival times and were therefore used for the subsequent crustal modeling.

For the onshore and on-offshore parts 51880 first arrival travel times from 80 stations (black picks in Fig. 3.6) were picked and used as the input data for the inversion. In addition at some stations a second arrival was picked, which was used for modeling a crustal reflection (red picks in Fig. 3.6).

Table A shows for every station (onshore and on-offshore data) the channel which was used for picking (Z-component of the seismometer or hydrophone) and the offset range where a first break was visible and picked.

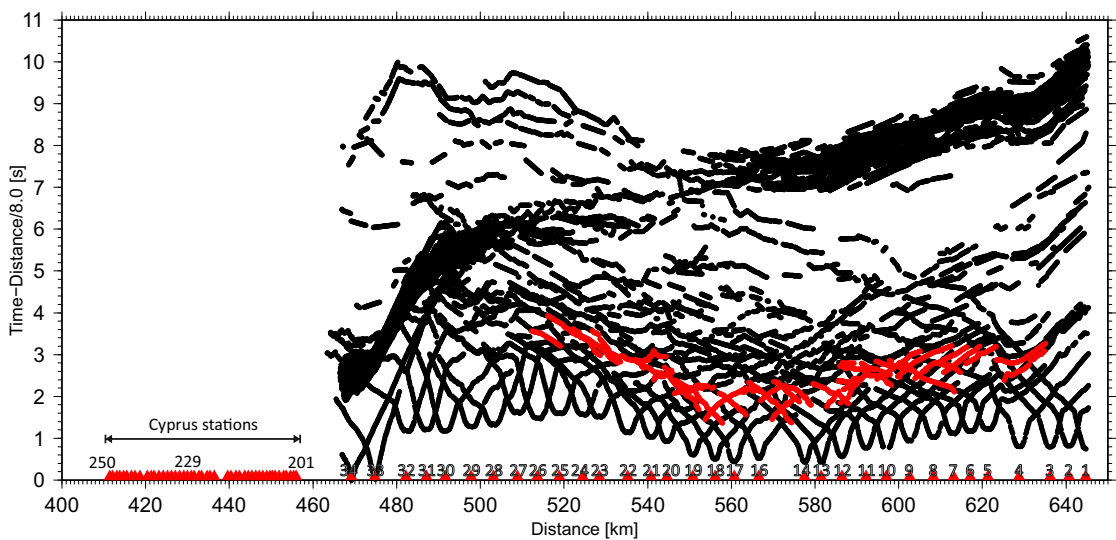


FIGURE 3.6: All picked first arrivals (black dots) and second arrivals (red dots) for the onshore and on-offshore parts of the profile. Red triangles are stations. Traveltime is reduced by 8 km/s

Onshore

The recordings of both land shots (T2001 and T2002) show a good data quality. The southern land shot has a good S/N ratio till about 200 *km* to the north. The southern land shot was also recorded on the Cyprus stations (Fig. 3.13). Although there is a high noise level at these recordings, it was possible to pick several phases (refractions and reflections, see Fig. 3.14). The northern land shot (T2002) shows a clear onset along the whole 300 *km* of the profile in Turkey (Fig. 3.15). In the seismogram section of the northern land shot an area with low energy on the first arrival is observed compared to later phases (red dashed area in Fig. 3.15). For the determination of the layered P-wave velocity model 201 first arrival times were picked (Figs. 3.13 to 3.16) and used for further analysis.

3.4 Data Examples

In the following section some seismogram sections are shown from the offshore part (OBS02, OBS17), from Cyprus (C229) and both land shots (T2001 and T2002). Each seismogram section is shown filtered without picked data and with picked first arrivals. All shown seismogram sections are reduced by 8 *km/s*.

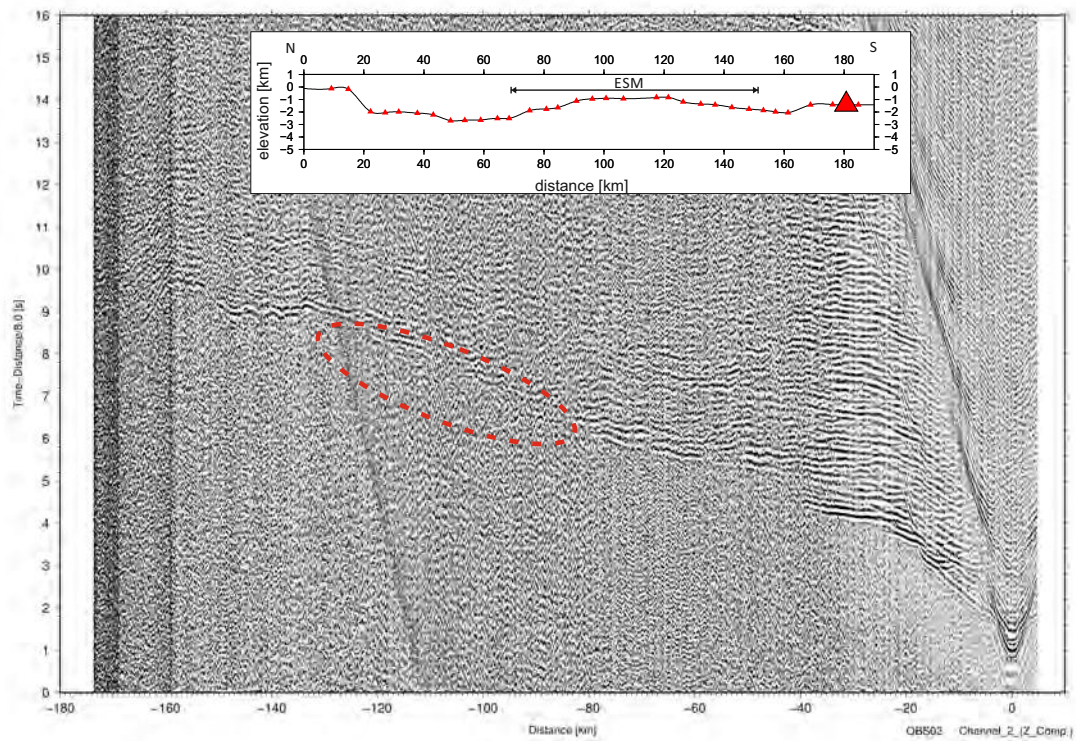


FIGURE 3.7: Seismic section of OBS02, band-pass filtered from 3 – 9 Hz and with an AGC applied (time window length: 5000 ms), where the red dashed ellipse shows area with low S/N ratio and no clear first arrival energy (compare to data example from station C229, Fig. 3.11). Inlay shows position of OBS02 (big red triangle) along the offshore profile. ESM = Eratosthenes Seamount

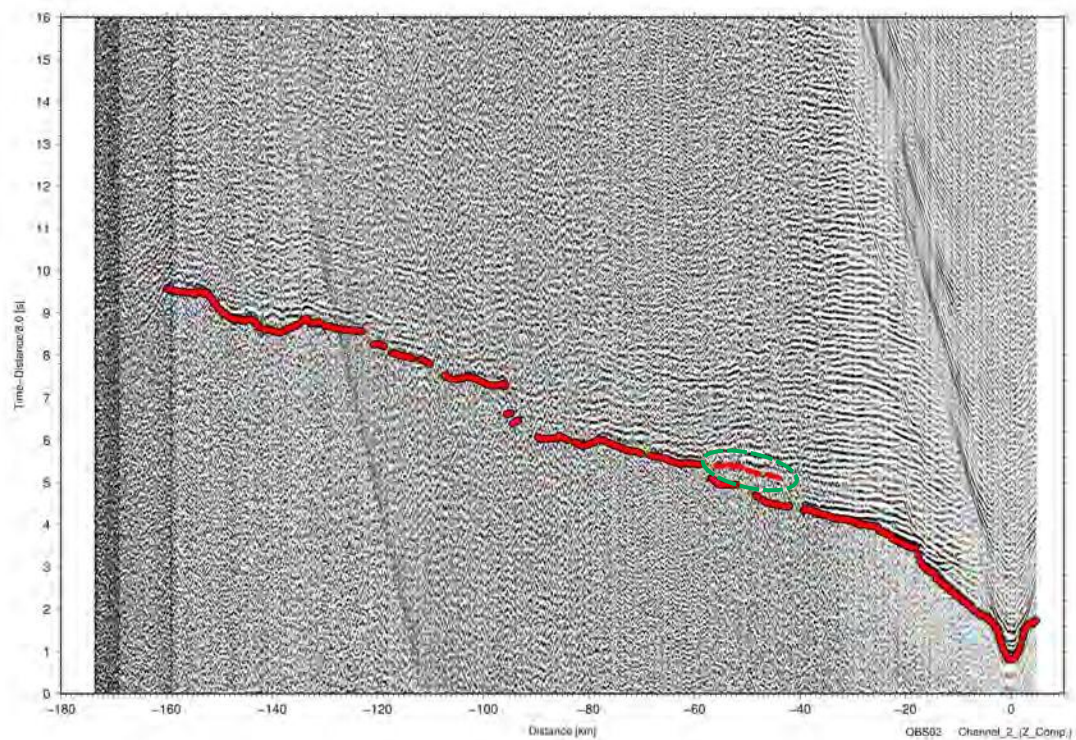


FIGURE 3.8: Seismic section of OBS02 with picked first arrivals (red dots with black outline). Green dashed ellipse marks the picked second arrivals, later used for modelling the upper crustal reflection

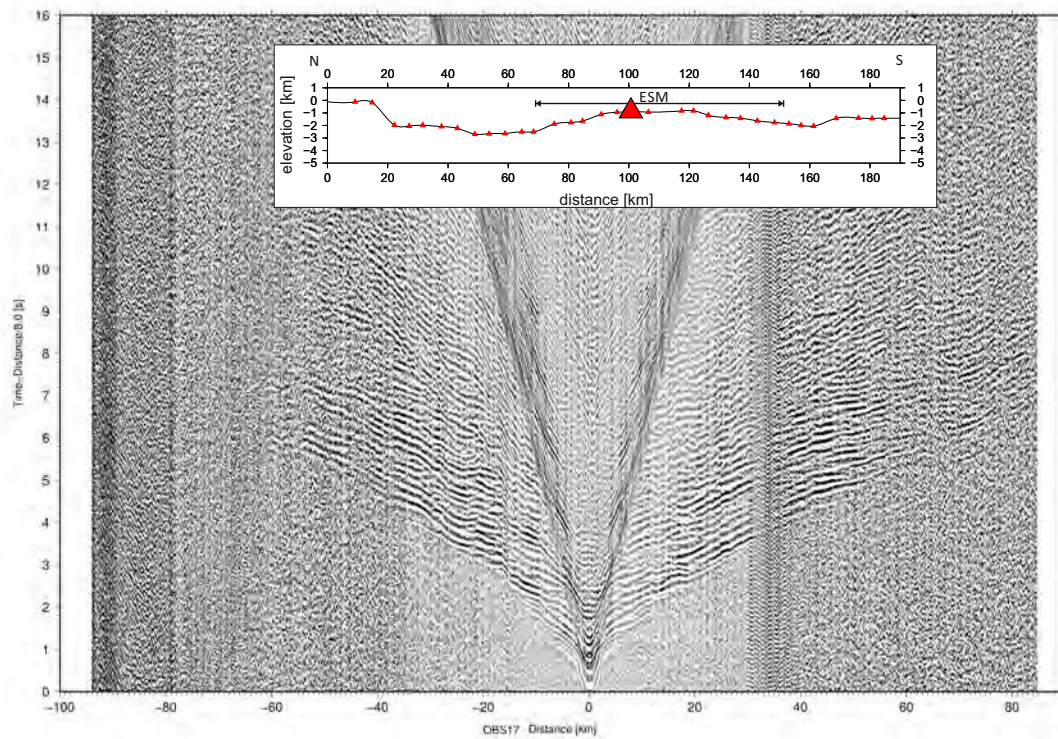


FIGURE 3.9: Seismic section of OBS17, band-pass filtered from 3 – 9 Hz and with an AGC applied (time window length: 5000 ms). Inlay shows position of OBS17 (big red triangle) along the offshore profile.

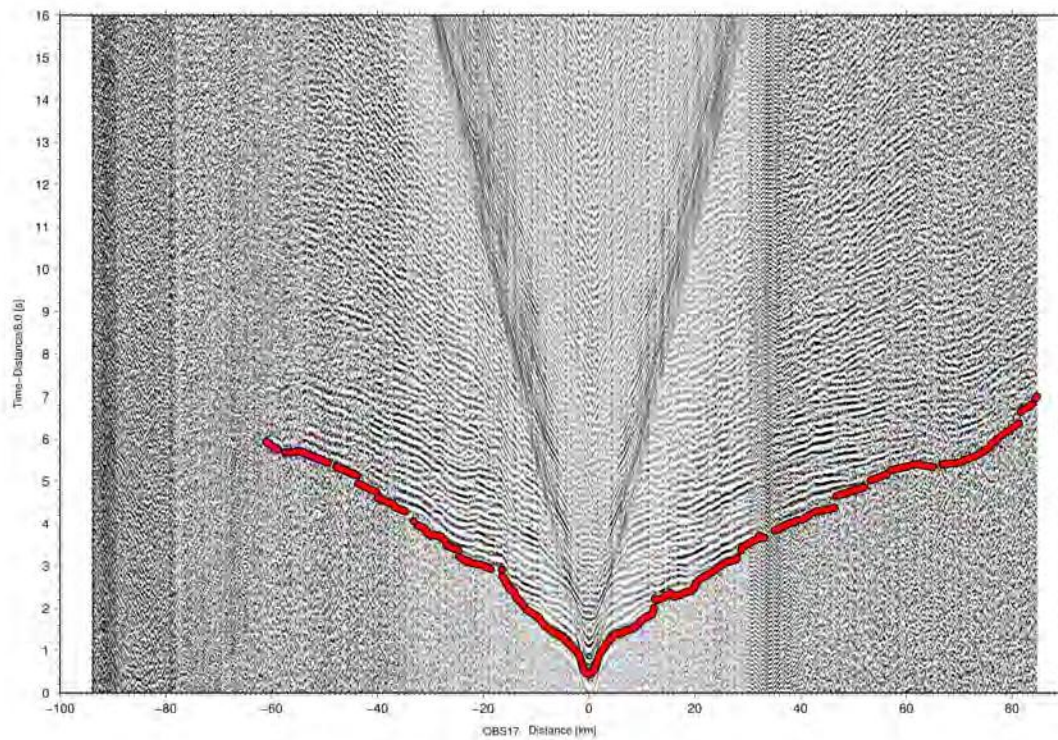


FIGURE 3.10: Seismic section of OBS17 with picked first arrivals (red dots with black outline).

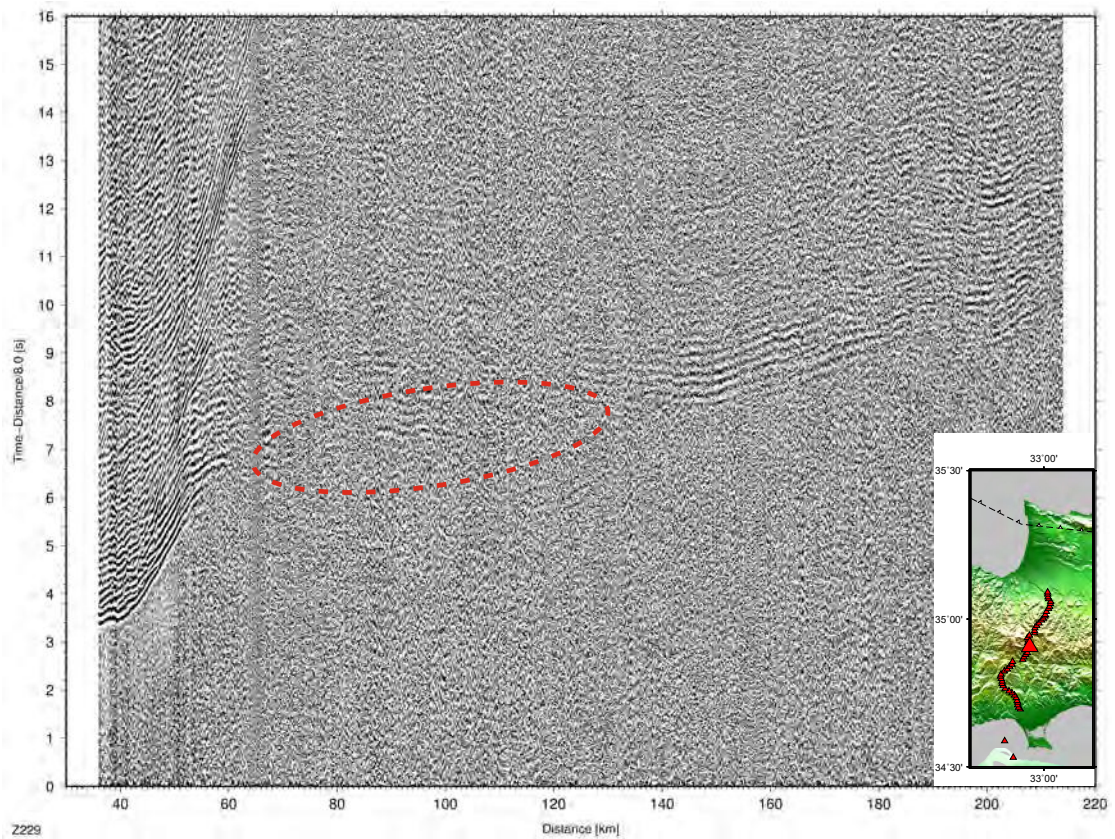


FIGURE 3.11: Seismic section of station C229 on Cyprus, band-pass filtered from 3 – 9 Hz and with an AGC applied (time window length: 5000 ms). Inlay shows location of station C229 (big red triangle) on Cyprus. Red dashed ellipse shows area of low S/N ratio and no clear first arrival energy (compare to data example from OBS02, Fig. 3.7)

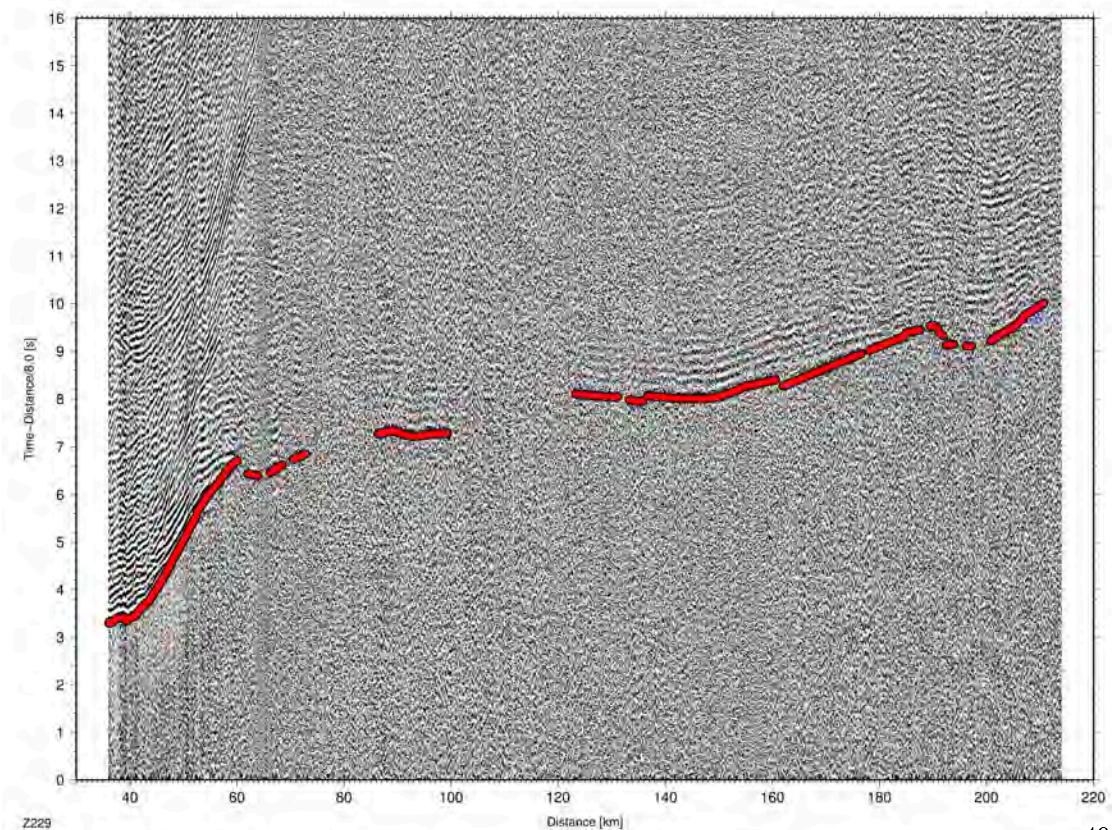


FIGURE 3.12: Seismic section of station C229 with picked first arrivals (red dots with black outline).

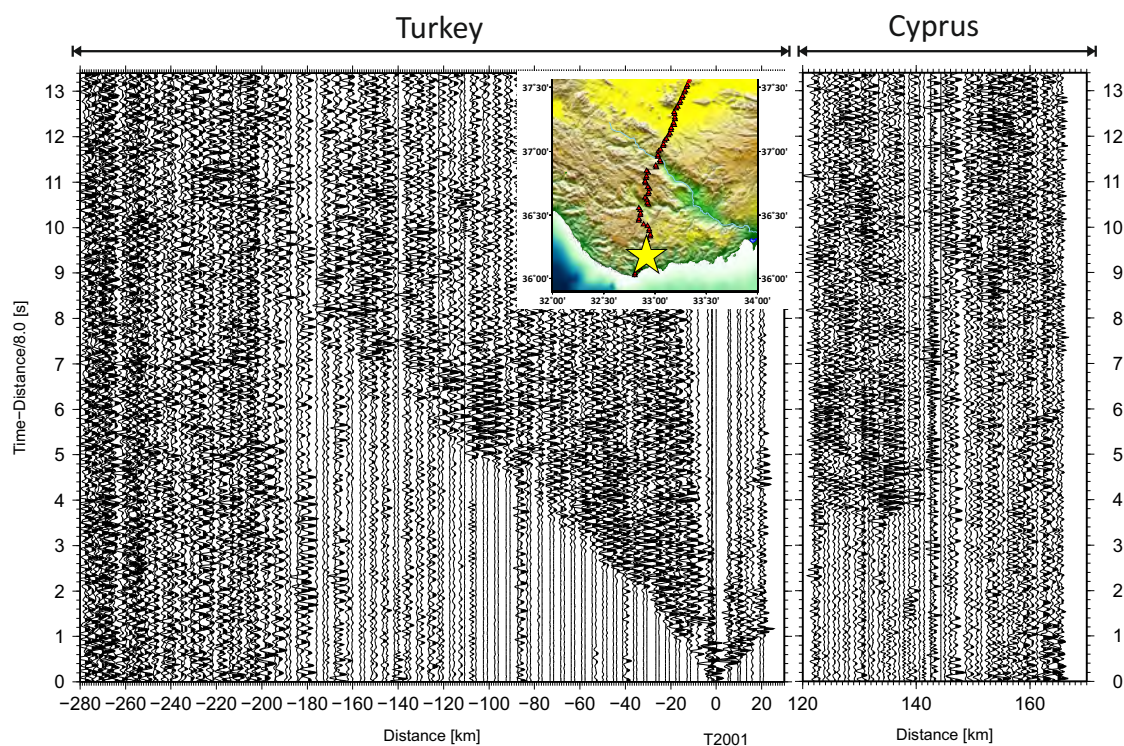


FIGURE 3.13: Seismic section of southern land shot in Turkey, band-pass filtered from 4 – 8 Hz. Inlay shows location of southern land shot (big yellow star). Note the recordings on Cyprus (120 – 170 km)

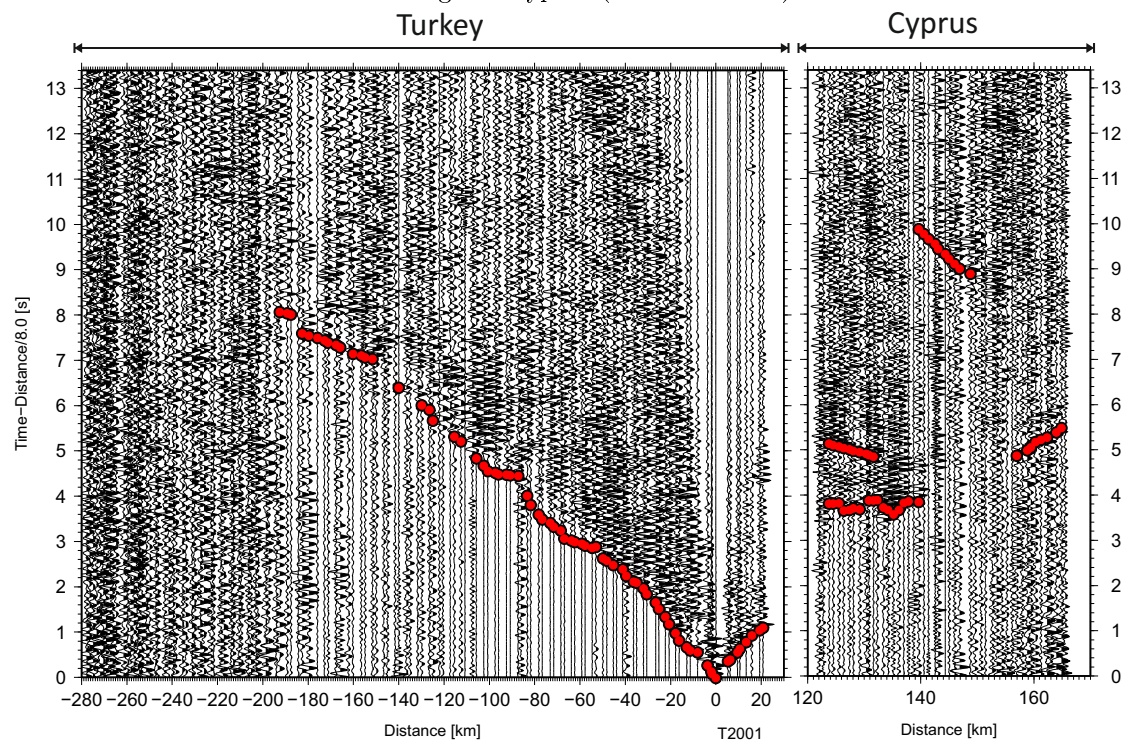


FIGURE 3.14: Seismic section of southern land shot with picked first and later arrivals in Turkey and Cyprus, band-pass filtered from 4 – 8 Hz. Note the recordings on Cyprus (120 – 170 km).

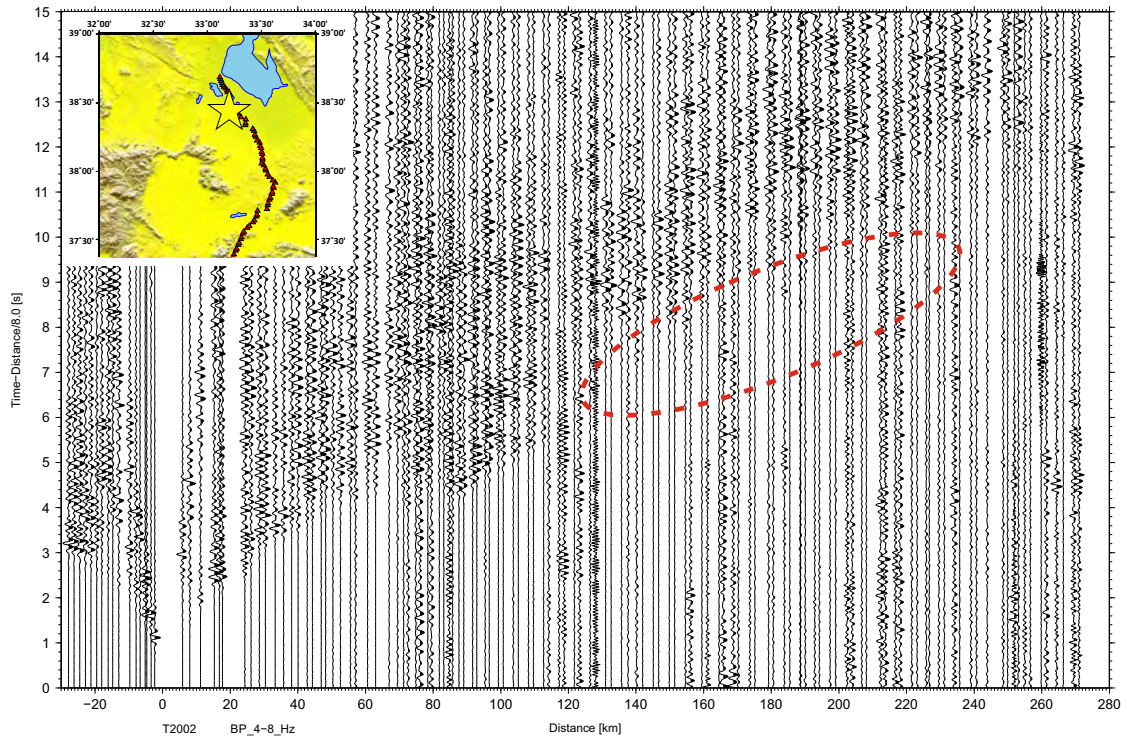


FIGURE 3.15: Seismic section of northern land shot in Turkey, band-pass filtered from 4 – 8 Hz . Inlay shows location of northern land shot (big yellow star). Red dashed ellipse shows area of low energy of first arrivals compared to later arrivals.

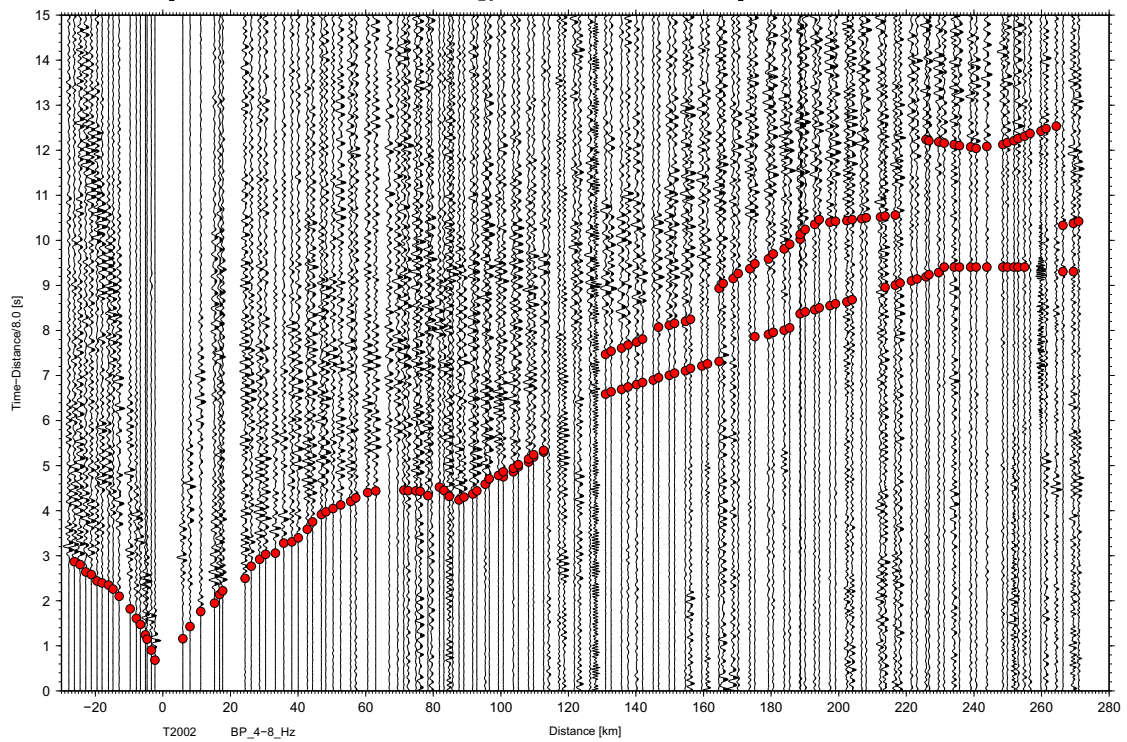


FIGURE 3.16: Seismic section of northern land shot with picked first and later arrivals in Turkey, band-pass filtered from 4 – 8 Hz .

Chapter 4

Crustal Modelling and Results

After picking the arrival times the next and essential part of the analysis is the development of a P-wave velocity model. The arrival times are picked in the data and exported in tables including the corresponding pick uncertainty. Since the modelling procedure is divided into two parts, the tomographic and layered velocity model (shown in Fig. 2.4), the results presented and discussed in this chapter follow this classification. Based on the combination of both velocity models revealed by the wide-angle seismic data a density model was built and theoretical gravity data calculated from this model were compared with a compiled gravity data set. In chronological order the modelling procedure involves the following steps:

- Inversion of the offshore data for a tomographic P-wave velocity model.
- Modelling of the onshore data (land shots) for a layered P-wave velocity model including the velocity structure beneath Cyprus.
- Extension of the offshore data with the on-offshore data (airgun shots recorded by the Cyprus stations), building an initial model for Cyprus based on the layered velocity model and inversion for a P-wave velocity model for the amphibian part (Cyprus - ESM).
- Transforming the P-wave velocity model (both layered and tomographic) to a gravity model and comparing the calculated gravity values with the measured gravity values.

- Simultaneous modification and adjustment of the gravity model, tomographic P-wave velocity model and layered P-wave velocity model till all geophysical data fit to one consistent crustal model.

Both the P-wave velocity model and the gravity model cross-section are defined along the transect shown in Fig. 1.3 (red line). A combined analysis of both geophysical methods leads to a geological interpretation and reveals the crustal structure of the transect.

4.1 Tomographic Velocity Model

4.1.1 1-D start model

Based on all picked first arrivals at the offshore stations a 1-D initial P-wave velocity model is estimated. Figure 4.1 shows all picked first arrivals times plotted against the distance. A polynomial function is fitted to these data (red line in Fig. 4.1) which is used to estimate an initial 1-D P-wave velocity model. A Moho at 27 km depth (Makris et al., 1983) is added to the estimated 1-D velocity model (Fig. 4.2). Table 4.1 shows the derived 1-D velocity model for the offshore part of the profile.

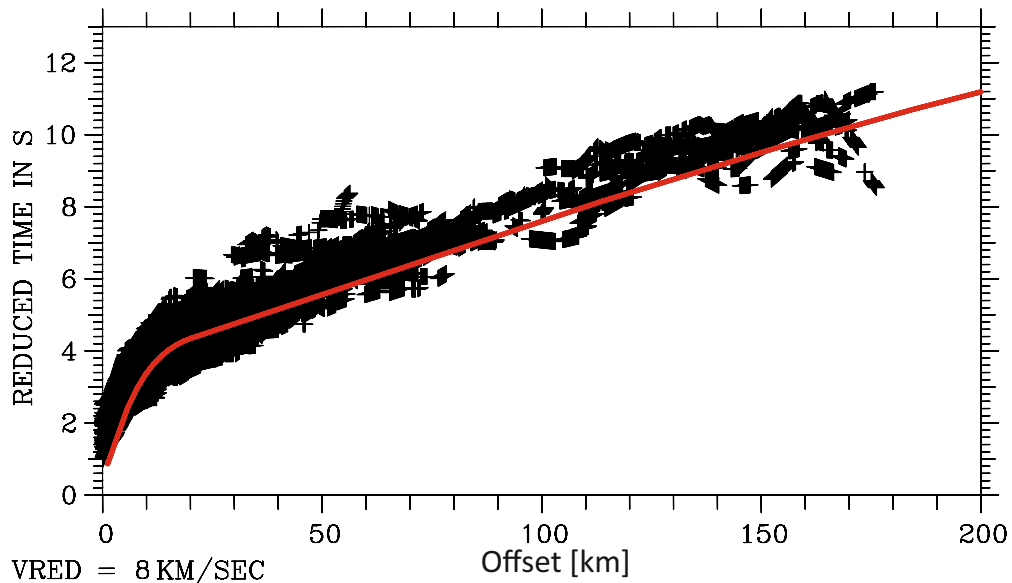


FIGURE 4.1: All picked first arrival times (reduced by 8 km/s) and a best fit line (red line) which is used for estimating the initial 1-D velocity model.

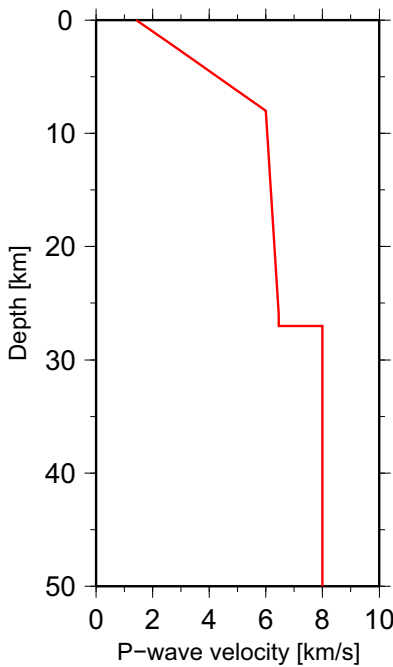


FIGURE 4.2: Initial 1-D P-wave velocity model used in this study.

TABLE 4.1: Initial 1-D P-wave velocity model used in this study.

P-wave velocity [km/s]	depth [km]
1.43	0
2.57	2
3.71	4
4.86	6
6.0	8
6.048	10
6.096	12
6.144	14
6.195	16
6.246	18
6.297	20
6.348	22
6.399	24
6.45	26
6.45	27
8.0	27
8.0	50

This initial 1-D velocity model represents the basis and the background model for all following inversions. As described in the next section (and shown in Table 4.2) the initial 1-D velocity model (model no. 001) is extended and modified iteratively.

4.1.2 Development of the tomographic model

For the initial versions of the tomographic velocity model (model nos. 1 - 47, see Table 4.2), only the offshore stations which recorded the airgun shots south of Cyprus (pure offshore part) were taken into account. Fig. 4.3 shows the final model no. 4608. This model was the final model of the offshore part only.

Later the offshore part was extended with the Cyprus stations which also recorded the airgun shots (model no. 50 - 100). This part of the profile (airgun shots, recorded by the Cyprus stations) is described with the term *amphibian* or *on-offshore* part. Due to the extension with the on-offshore part it was possible to reveal the deeper velocity structure and obtain some evidence for the Moho depth beneath Cyprus. The development of the velocity model beneath Cyprus is discussed in more detail in the section 4.1.3. The total length of the off- / on-offshore profile is 250 km (at a distance from 400 – 650 km along the whole profile).

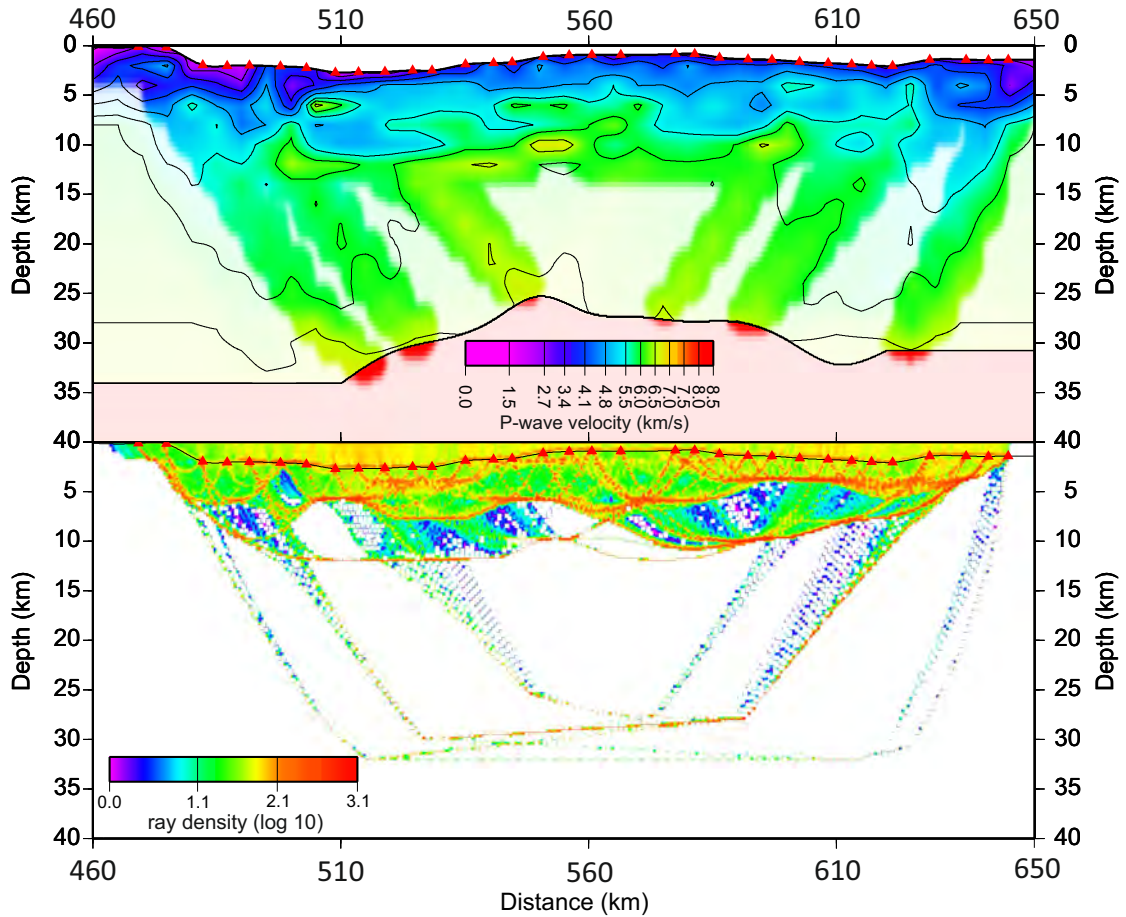


FIGURE 4.3: Final P-wave velocity model of the offshore part only (above) and corresponding ray plot (below). The Moho is inverted from the data.

The development of the tomographic velocity model involves the extensive modification of the initial model and alteration of model parameters such as grid spacing and damping factor (see Table 4.2).

The first models (model nos. 1 - 7) have a constant horizontal grid spacing of 10 *km* and a vertical grid spacing of 2 *km*. The damping factor was varied from 100 to 5000. In the following model series (nos. 8 and 14 to the final model) the horizontal grid spacing is reduced to 5 *km* and a damping factor of 500 shows the lowest residuals for the offshore part. A horizontal grid spacing of 5 *km* equates approximately to the station spacing offshore. If horizontal grid spacing is reduced further then one has many boxes at the surface with no stations in them and thus one can obtain horizontal oscillations in near surface velocities. The final model series (no. 10001, off / on-offshore profile) has a damping factor of 2000, which is a reasonable compromise between too slow convergence (caused by high damping factors, e.g. 5000) and instability (caused by low damping factors, e.g. 100) e.g. negative velocities, which cause problems for the program. In the

models 9 to 13 the grid spacing was varied, with the horizontal spacing being reduced to 2.5 km and the vertical spacing to 0.5 km. In addition a varying vertical grid spacing was tested (model nos. 9 and 10: for the upper 14 km a grid spacing of 1 km and below 2 km). Some models used a model from the previous model series as the initial model (e.g. model nos. 11 and 12) instead of the initial starting model. Table 4.2 shows an extract of the model series with the corresponding model parameters and initial model. In addition the number of features which are inverted is varied. For example, in the model series 18 the Moho boundary was inverted, the model series 27 includes the inversion of both the Moho and mantle velocity and in the model series 42 the Moho was fixed based on the results of the previous model series, but the mantle velocity was inverted. All in all the development of the tomographic P-wave velocity model involves 70 model series. In addition 9 inversions were performed to model the upper crustal reflection beneath the ESM.

The Moho geometry of the final offshore P-wave velocity model no. 4608 (see Fig.4.3) was used as the input Moho geometry for the subsequent modelling of the offshore / on-offshore part (model series nos. 50 – 53). Subsequent modification of the initial P-wave velocity model and the Moho geometry shows that the most reasonable results were achieved if the initial Moho is a flat plane with a constant initial Moho depth of e.g. 25 km (model series nos. 58-63) or 35 km (model series no. 7701).

This development leads to a decreasing RMS¹ value (see Table 4.2) and a better fitting of the data to the model. Due to the significantly higher number of picks for model series 50-100 the RMS value is about ~ 0.21 s instead of ~ 0.18 s. For the decision of which resulting P-wave velocity model should be used for further analysis, not only the RMS value was considered but also the question of whether the P-wave velocity model is geologically reasonable was taken into account. Model series 4708 and 11008 are models where the picked secondary phases (see red dots in Fig. 3.6) are inverted for an upper crustal reflection.

4.1.3 Development of the velocity model beneath Cyprus

The area of Cyprus represents the boundary between the layered P-wave velocity model (northern part of the profile, onshore part) and the tomographic P-wave velocity model

¹Root Mean Square, see Eq. 2.24

TABLE 4.2: Examples of model series with corresponding inversion parameters.

model no. ¹	initial model	number of picks	horizontal grid spacing [km]	vertical grid spacing [km]	damping factor	data uncertainty ² [s]	a priori model uncertainty	RMS [s]	CHI^2	comments
108	001 ³	21861	10	2	1000	0.01 - 0.2	$V_p : \pm 1 \text{ km/s}$	0.22	3.1	
208	001	21861	10	2	1000	0.1	$V_p : \pm 1 \text{ km/s}$	0.19	3.67	
306	001	21861	10	2	1000	0.05 - 0.2	$V_p : \pm 1 \text{ km/s}$	0.20	3.52	
408	001	21861	10	2	500	0.05 - 0.2	$V_p : \pm 1 \text{ km/s}$	0.198	3.466	
508	001	21861	10	2	5000	0.05 - 0.2	$V_p : \pm 1 \text{ km/s}$	0.2143	3.908	
607	001	21861	10	2	250	0.05 - 0.2	$V_p : \pm 1 \text{ km/s}$	0.198	3.455	
707	001	21861	10	2	100	0.05 - 0.2	$V_p : \pm 1 \text{ km/s}$	0.198	3.449	
808	001	21861	5	2	500	0.05 - 0.2	$V_p : \pm 1 \text{ km/s}$	0.183	3.073	
908	001	21861	5	2	500	0.05 - 0.2	$V_p : \pm 1 \text{ km/s}$	0.198	2.755	
1008	001	21861	5	1 (<14km depth), 2 (>14km depth)	250	0.05 - 0.2	$V_p : \pm 1 \text{ km/s}$	0.178	2.749	
1108	403 ⁴	21861	5	1	500	0.05 - 0.2	$V_p : \pm 1 \text{ km/s}$	0.1777	2.679	
1208	1103 ⁵	21861	2.5	0.5	500	0.05 - 0.2	$V_p : \pm 1 \text{ km/s}$	0.1777	2.679	
2708	001	21861	5	2	500	0.05 - 0.2	Moho: $\pm 5 \text{ km}$ $V_p : \pm 1 \text{ km/s}$	0.181	3.05	Moho depth and mantle velocity are also inverted
4608	001	21890	5	2	500	0.05 - 0.2	Moho: $\pm 2 \text{ km}$ $V_p : \pm 1 \text{ km/s}$	0.18	2.72	Moho depth is inverted, final model of the offshore part
4708	4608	2444	5	2	100	0.05 - 0.2	reflector: $\pm 5 \text{ km}$	0.122	1.85	Inversion of the upper crustal reflection
10008	8901	51880	5	2	2000	0.05 - 0.2	$V_p : \pm 1 \text{ km/s}$	0.210	2.68	final tomographic P-wave velocity model
11008	10008	2444	5	2	100	0.05 - 0.2	reflector: $\pm 5 \text{ km}$	0.123	1.77	Inversion of the upper crustal reflection

¹ first digit is the model no. and last digit is the number of iteration, for example 1305 = fifth iteration of model no. 13² rms value of the data is 0.14 s³ initial P-wave velocity model⁴ third iteration of model no. 4⁵ third iteration of model no. 11

(southern part of the profile, offshore part). This and the complex geological structure of Cyprus with the Troodos ophiolite complex was the reason for a special treatment in model development for this region. Thus the first step for the development of the velocity model was to include geological information (Fig. 4.4) to build a layered P-wave velocity model (Fig. 4.5) with the boundary to the tomographic model at the southern coast of Cyprus (tomographic model just from offshore stations, model nos. 1 – 47). Later this layered velocity model was used to build the initial model for a tomographic velocity model beneath Cyprus with the boundary to the layered velocity model at the northern coast of Cyprus (tomographic model from offshore stations and stations onshore Cyprus, model nos. 50 – 100).

Based on geological information and maps (Fig. 4.4) and the positions of the stations on Cyprus the boundaries between the stratigraphic units (Sediments, Pillow lavas, Sheeted Dykes and Gabbros) along the profile were derived (Table 4.3). For every geological unit a corresponding P-wave velocity is assigned and integrated into the layered (later tomographic) initial model. It is known that for example the Gabbro unit of the Troodos crops out along the profile. Based on the study of Mackenzie et al. (2006) the Gabbro unit was assigned a P-wave velocity of 6.75 km/s . Table 4.3 shows all stratigraphic units, the stations located on these units and the corresponding P-wave velocities from Mackenzie et al. (2006).

TABLE 4.3: Stratigraphic units beneath Cyprus, the stations located on the unit and the corresponding P-wave velocity from Mackenzie et al. (2006); Salisbury et al. (1989); Smith and Vine (1989). Layered P-wave velocity model for Cyprus is shown in Fig. 4.5

stratigraphic unit	station no.	P-wave velocity [km/s]
Sediments	C201 - C221 and C248 - C250	2.8 - 2.9
Pillow Lavas	C222 and C240 - C247	3.6 - 3.7
Sheeted Dyke Complex	C223	5.5 - 5.6
Gabbro	C224 - C239	6.75

The initial layered velocity model for Cyprus (Fig. 4.5) takes the dome character of the Troodos complex into account. It was transformed and added to the initial model for the tomographic inversion of the off- / on-offshore data (Fig. 4.6).

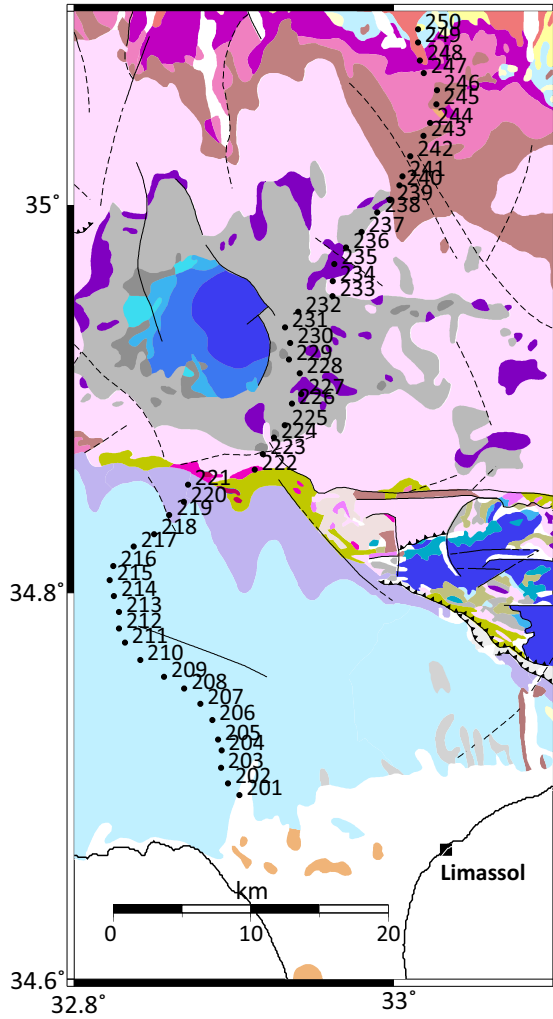


FIGURE 4.4: Detailed geological map of Cyprus with receiver locations. Legend is shown in Appendix B.

4.1.4 Results

With a RMS value of 0.21 s and a CHI^2 value of 2.68 the model no. 100 (8th iteration = 10008) is the final P-wave velocity model for the off- / on-offshore part. With a CHI^2 value of 2.68 the data are not over-fitted. Figure 4.6 shows the corresponding starting model 10001. The Moho geometry was fixed and not inverted during the final model no. 100. The Moho geometry was adopted from model no. 7708, where the initial Moho geometry was a flat plane with a constant Moho depth of 35 km. The upper mantle velocity of 8.0 km/s was also not inverted because previous inversions showed that the inversion of the upper mantle velocity interferes with the resulting model and leads to an unreasonably low P-wave velocity in the upper mantle in disagreement with previous

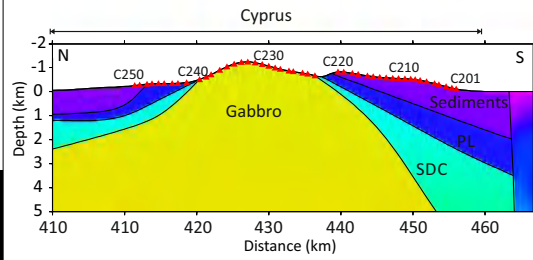


FIGURE 4.5: Initial layered velocity model for the Troodos ophiolite complex beneath Cyprus. Red triangles are stations onshore Cyprus (C201 - C250), SDC = Sheeted Dyke Complex, PL = Pillow Lavas, P-wave velocities are shown in Table 4.3 and the P-wave velocity scale is shown in Fig. 4.6.

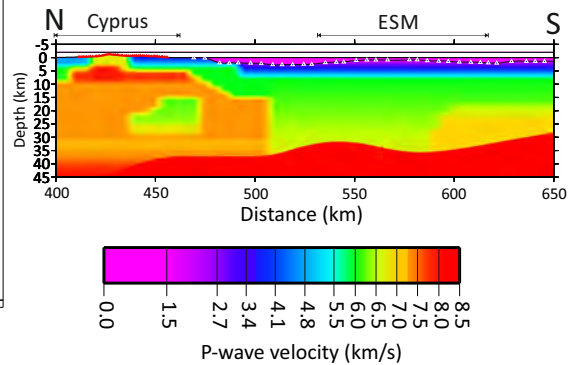


FIGURE 4.6: Off- / On-Offshore initial P-wave velocity model no. 10001.

studies (Makris et al., 1983). Thus the mantle velocity is assigned a value of 8.0 km/s in agreement with Makris et al. (1983).

The final P-wave velocity model (Fig. 4.7 with the key observations labeled) involves seismic phases traveling down to 35 km depth, revealing the P-wave velocity distribution and the Moho depth and geometry.

The key observations (shown and labeled in Fig. 4.7) and first geological interpretations of this model are:

- 1.) Moho depth: a Moho depth of 28 km at the southern end of the profile, increasing up to $32 - 35 \text{ km}$ depth beneath the ESM. North of the ESM the Moho depth is about 37 km and increasing beneath Cyprus.
- 2.) General P-wave velocities: Beneath the ESM P-wave velocities of 5.5 to 6.5 km/s were derived. The absence of a lower crystalline crust with P-wave velocities higher than 6.5 km/s is observed in this region. North of the ESM ($450 - 525 \text{ km}$ offset) P-wave velocities between 6.5 and 7.0 km/s are observed at depths greater than 15 km .
- 3.) Sediments: Low P-wave velocities ($< 4.8 \text{ km/s}$) occur at shallow depths (max. 5 km) beneath the ESM and greater depths (max. 12 km) south and north of the Eratosthenes Seamount. They are interpreted as sedimentary cover with a thickness of about $5 - 12 \text{ km}$ south and north of the ESM. Beneath the ESM the sedimentary cover is thinner with $1 - 5 \text{ km}$ thickness.
- 4.) Accretionary wedge: The triangle shaped low velocity zone (P-wave velocities lower than 5.5 km/s) north of the ESM (reaching a depth of 15 km) has a north dipping lower surface starting at the trench of the Cyprus arc (at an offset of 512 km along the profile, red dashed line in Fig. 4.7). Due to this geometry and P-wave velocities this low velocity zone is interpreted as the accretionary wedge above the northward subducting plate with a total width of $\sim 37 \text{ km}$.
- 5.) South of the ESM ($620 - 650 \text{ km}$): The presence of a thickened low velocity layer ($< 4.8 \text{ km/s}$) in the upper $10 - 12 \text{ km}$, higher velocities in the lower crust and the decreasing Moho depth to about 28 km are indicators for a transition towards a crust with a different origin.

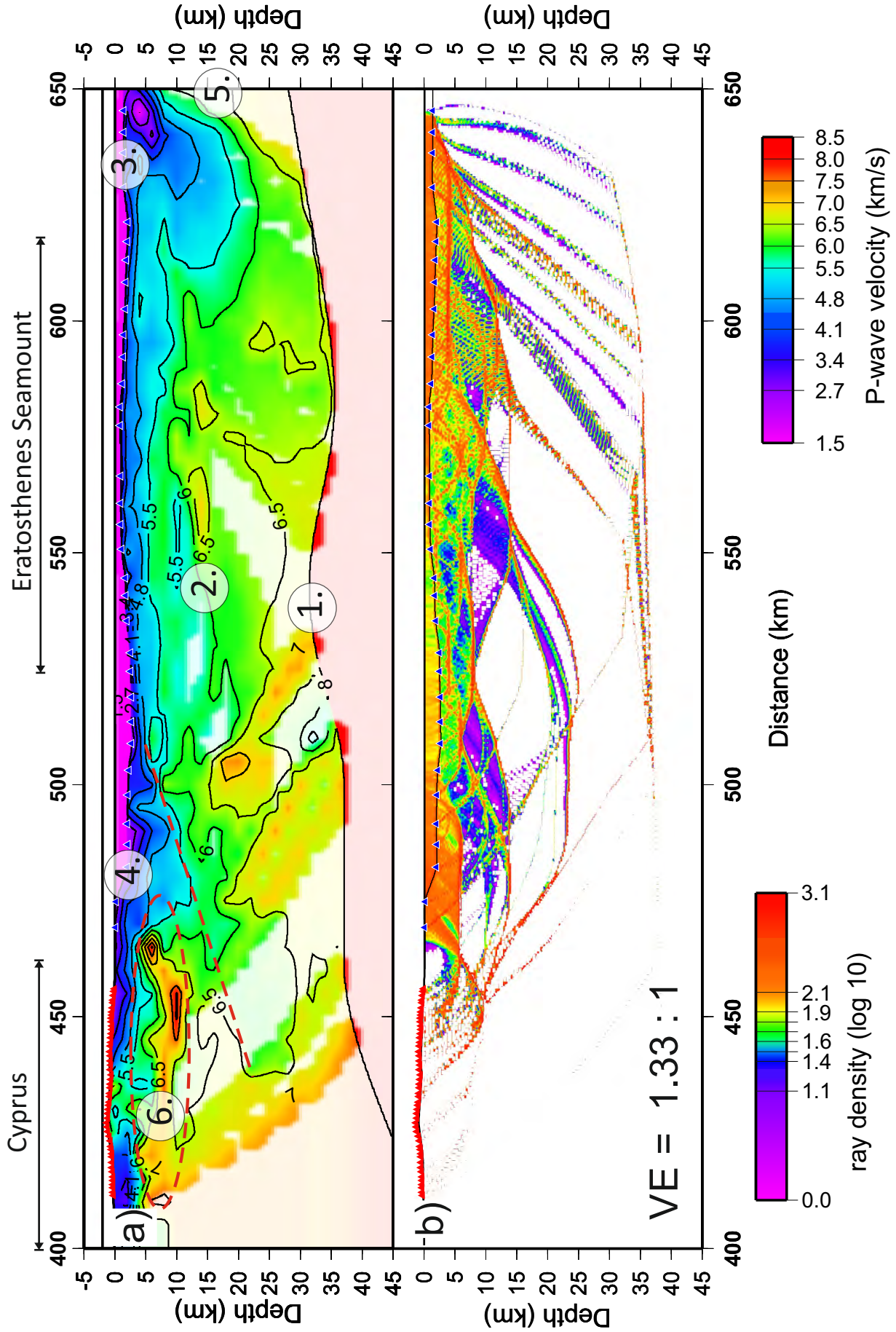


FIGURE 4.7: a) Final tomographic P-wave velocity model with key observations labeled with 1. - 6., see text for more detail and b) ray density plot. Both plots have a vertical exaggeration of 1.33 : 1 .

- 6.) A high velocity zone ($7.6 - 8.0 \text{ km/s}$) beneath Cyprus which is interpreted as the ophiolite sequence of the Troodos complex on Cyprus (red dashed ellipse in Fig. 4.7). The high velocity zone is located at $5 - 12 \text{ km}$ depth and extends offshore south of Cyprus (up to 470 km offset).
- 7.) The picked secondary seismic phases (labeled red in Fig. 3.6 and green dashed ellipse in Fig. 3.8) were used to invert a reflector beneath the ESM. The geometry of this reflector is shown and labeled in Fig. 4.8. The modeled reflector is located at $8 - 9 \text{ km}$ depth at the northern and southern end of the ESM. Directly beneath the ESM the reflector rises up to 3.5 km depth. The geometry of the reflector corresponds to the 5.5 km/s P-wave velocity isoline and agrees with the general observation that the upper low-velocity layers ($< 4.1 \text{ km/s}$) thicken to the north and south of the ESM. Therefore this modeled reflector could be interpreted as the boundary between the sedimentary layers and the upper crystalline crust beneath the ESM.

4.1.5 Checkerboard Tests

For the offshore and on-offshore part a checkerboard test was performed to reveal the resolution with depth. With the checkerboard test a regular pattern of velocity anomalies is recovered by the data. Therefore an input model has to be built which consists of regular, rectangular patches of opposite velocity anomalies (e.g. $+ 0.3 \text{ km/s}$ and $- 0.3 \text{ km/s}$, see Fig. 4.9 top). These perturbations are combined with a background model which corresponds to a 1-D average of the model that is being tested. A subsequent forward calculation produces the theoretical traveltimes corresponding to the perturbed velocity model. Random noise was added to these traveltimes which are then used for the following inversion. The result of this inversion is ideally a reproduction of the input velocity anomaly grid. If the recovered velocity patches are undeformed with respect to the input anomaly grid, then one can be confident that the data can resolve velocity structures similar in size to the input checkerboard anomalies. In those areas where the recovered velocity patches are deformed, smeared and not reconstructed the resolution capability of the data is lower than the size of the velocity anomalies. In this way the checkerboard test provides an estimation of the size of the velocity anomalies that can be well resolved in which depths. The checkerboard tests performed with the final model of

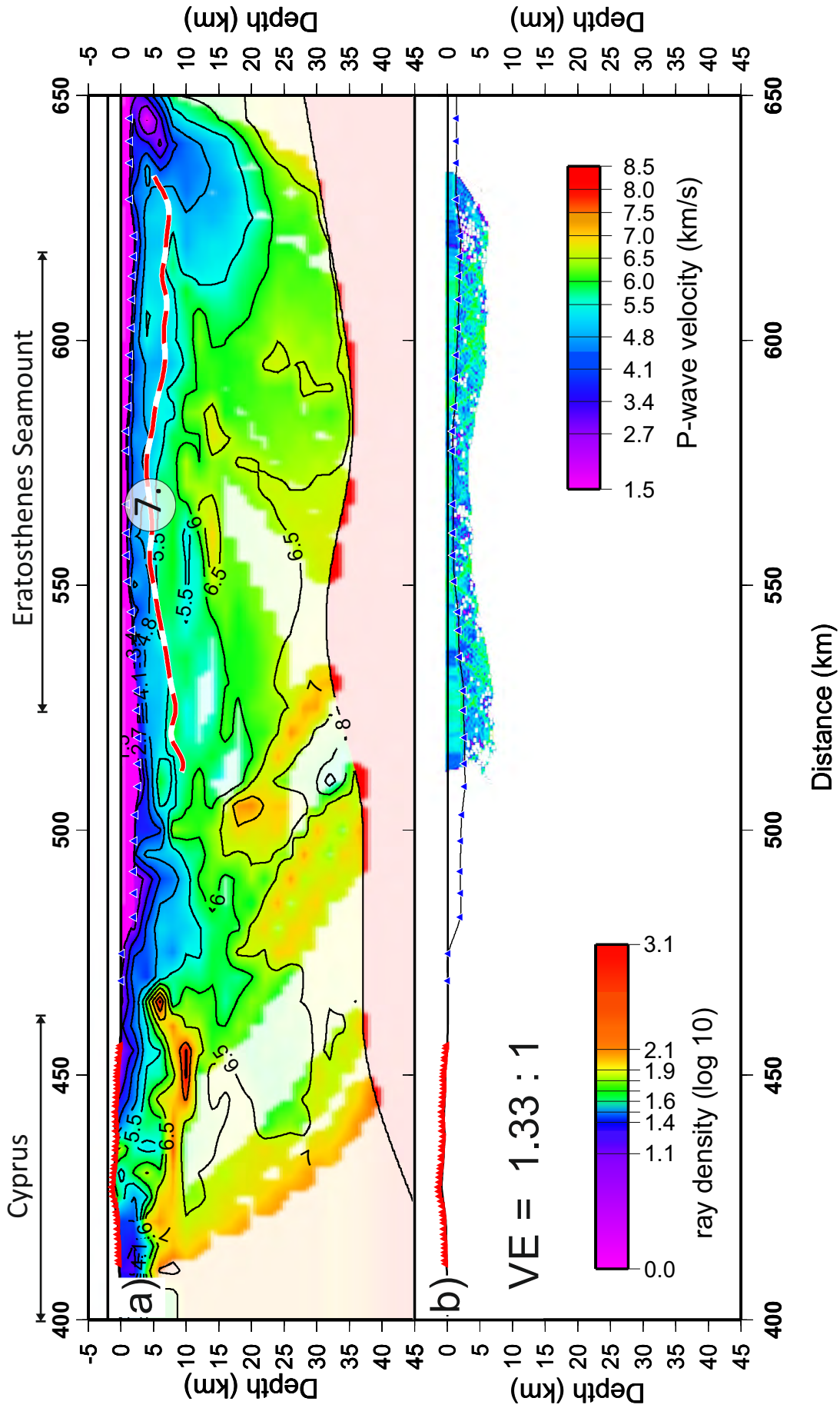


FIGURE 4-8: a) Final tomographic P-wave velocity model with modelled upper crustal reflection (red dashed line) and b) ray density plot. Both plots have a vertical exaggeration of 1.33 : 1 .

the tomographic velocity model consist of two different block sizes of velocity anomalies. The input model and the result of the smaller block size ($10 \times 4 \text{ km}$) is shown in Fig. 4.9 and the input model and the result of the bigger block size ($15 \times 6 \text{ km}$) is shown in Fig. 4.10.

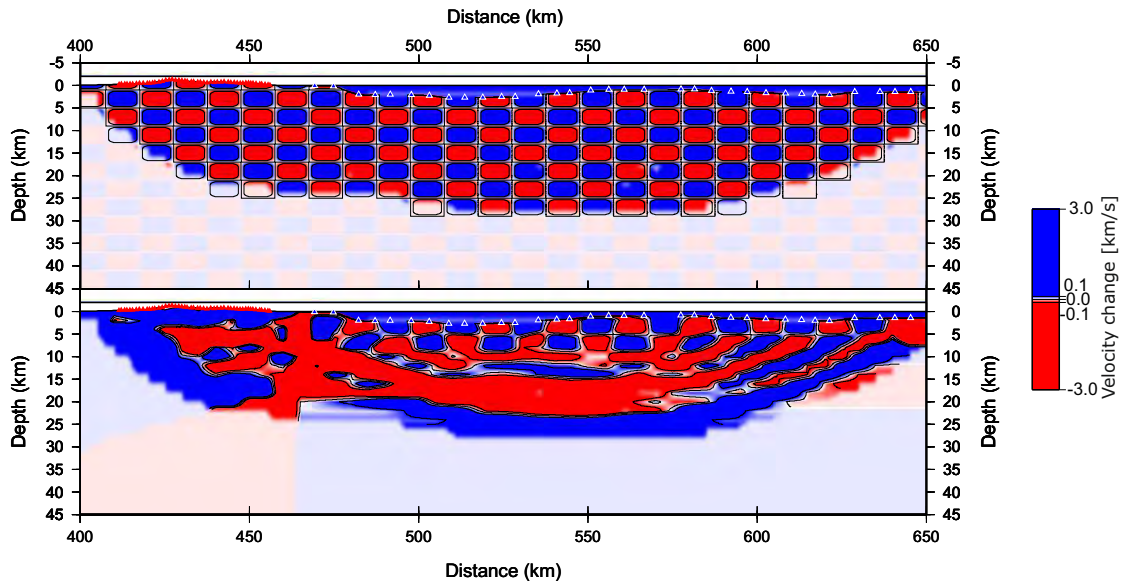


FIGURE 4.9: Checkerboard test with a grid size of $10 \times 4 \text{ km}$ (above: input model below: output recovered model). Grid could be recovered till $\sim 10 - 15 \text{ km}$ depth in the offshore part

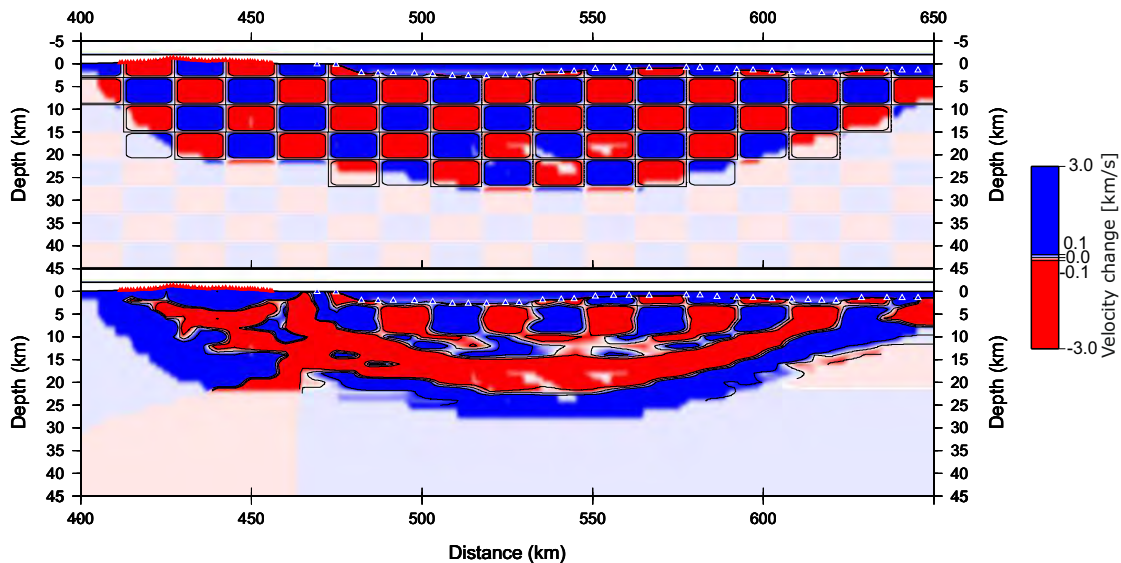


FIGURE 4.10: Checkerboard test with a grid size of $15 \times 6 \text{ km}$ (above: input model, below: output recovered model). Grid could be recovered till $\sim 10 - 15 \text{ km}$ depth in the offshore part.

The results (Figs. 4.9 and 4.10) reveal that both block sizes could be resolved well till a depth of $\sim 10 - 15 \text{ km}$ for the offshore area south of Cyprus. This means that for the offshore area P-wave velocity structures with a size greater than $10 \times 4 \text{ km}$ can be

resolved well in the upper $\sim 10 - 15 \text{ km}$. The data can resolve the velocity structure to some degree in the lower crust below 15 km depth, but when interpreting the crustal structure below 15 km depth it has to be considered that the geometry of the structures are less well constrained. Due to the lack of crossing rays and the lower ray density the onshore area beneath Cyprus is less well constrained compared to the offshore area south of Cyprus.

4.1.6 Picked vs. calculated traveltimes

To compare the observed and picked traveltimes with the calculated traveltimes both were plotted onto the data. The following figures show two examples with the calculated traveltimes of the final tomographic P-wave velocity model (OBS02 and C229, Fig. 4.11 and 4.12, respectively). The example of the station OBS02 (Fig. 4.11) shows the good fitting of the picked traveltimes (in red) and the calculated traveltimes (in green). At the northern end a P_n phase is observed. The example of station C229 (Fig. 4.12) shows also that the calculated P_g and P_n phases fit very well to the data.

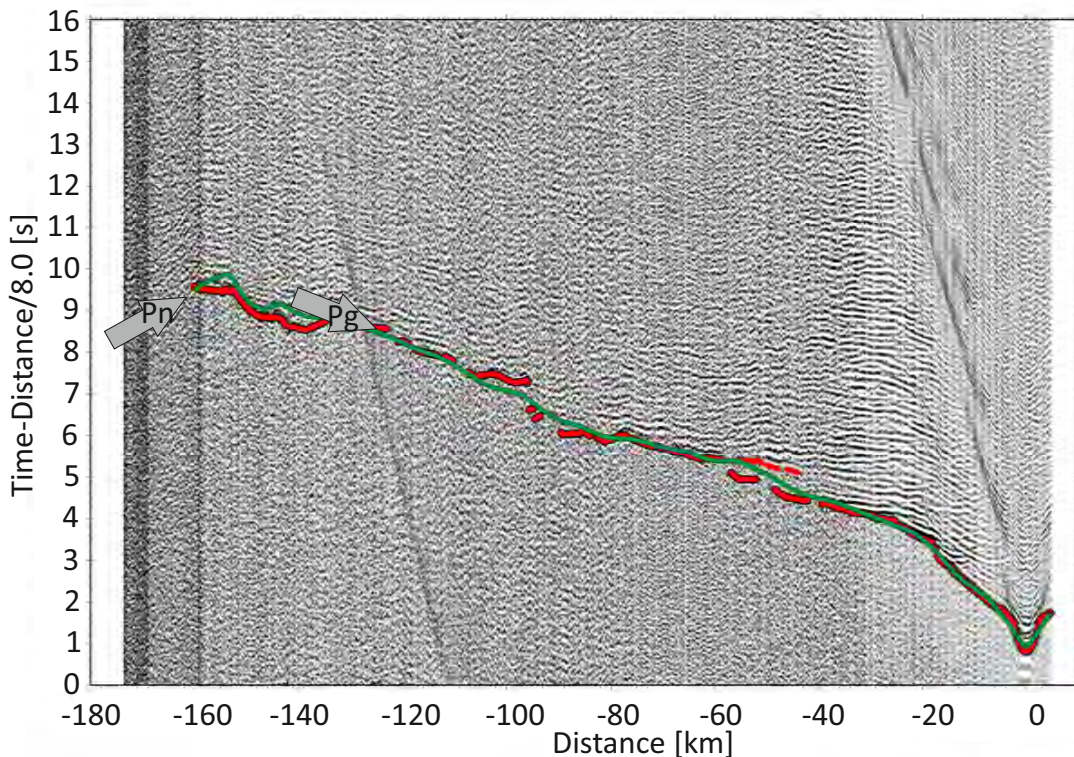


FIGURE 4.11: Seismic section of OBS02, band-pass filtered from $3 - 9 \text{ Hz}$. Red circles show picked first arrival times and the green solid line shows calculated first arrival times (P_g and P_n) based on the final tomographic P-wave velocity model (Fig. 4.7).

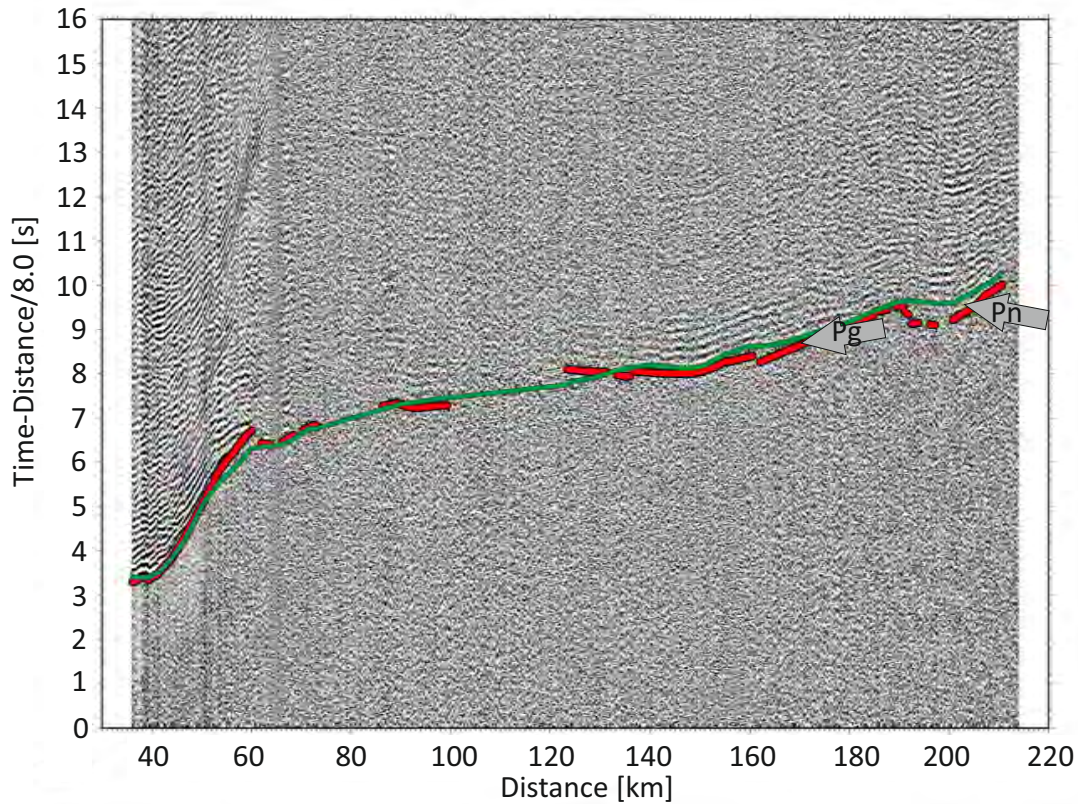


FIGURE 4.12: Seismic section of C229, band-pass filtered from 3 – 9 Hz. Red circles show picked first arrival times and the green solid line shows calculated first arrival times (Pg and Pn) based on the final tomographic P-wave velocity model (Fig. 4.7).

4.1.7 Discussion

Based on the observations made, the tomographic P-wave velocity model can be divided into 4 different sectors with different geological and geodynamic interpretations which will be discussed in the following from south to north.

(I) South of the ESM

The area south of the ESM ($\sim 625 - 650$ km offset) shows a thickening of the sediments (ca. ~ 12 km), higher velocities (> 6.5 km/s) in the lower part of the crust and a Moho at about 28 km depth. Compared to the area beneath the ESM a change in crustal thickness and P-wave velocity structure can be observed.

This is similar to the observations made by Makris et al. (1983) and Ben-Avraham et al. (2002). They suggested a transition from continental crust underlying the ESM to an oceanic crust underlying the thick sedimentary sequence of the Levant Basin. East and

south of the ESM an evaporitic layer ($v_p = 4.2 \text{ km/s}$) thickens from the seamount toward the basin. A thickening of P-wave velocities lower than 4.8 km/s toward the southern end of the profile is also observed in the velocity model presented here. [Ben-Avraham et al. \(2002\)](#) also recognize a sediment layer with P-wave velocities of 4.5 km/s at a depth of $\sim 12 \text{ km}$. This is consistent with the interpretation of the P-wave velocity model presented in this study. The upper $10 - 12 \text{ km}$ of the most southern part of the profile consists mainly of thick sediments probably including an evaporitic layer with P-wave velocities of $2.5 - 4.6 \text{ km/s}$. The geological investigation by [Robertson \(1998b\)](#) suggests a basin south of the ESM infilled with young and rapidly subsiding turbidites and Messinian evaporites (see Fig. 1.5a), also confirming the results presented here.

In the lower crust a southward increasing P-wave velocity can be observed (up to $\sim 6.9 \text{ km/s}$). This is further evidence for a transition to oceanic crust. [Ben-Avraham et al. \(2002\)](#) also observed a southward thinning of the 6.0 km/s layer (greenish colors in Fig. 4.7) towards oceanic crust with a P-wave velocity of 6.7 km/s overlain by thick sediments.

The southward decrease of the Moho depth in this sector also supports the interpretation of a southward transition from continental (crustal thickness greater than 25 km , [Ben-Avraham et al., 2002](#)) to oceanic crust with a Moho depth of $< 25 \text{ km}$. Especially for the deeper crustal structure (P-wave velocities and Moho depth) of this area, it has to be considered that this is near the edge of the velocity model and is therefore not so well constrained due to the lack of seismic rays. Nevertheless, in summary, the section south of the ESM is mainly characterized by the southward transition from continental crust with a thin sedimentary layer to oceanic crust with thick sediments and evaporites.

(II) ESM

Beneath the ESM ($\sim 525 - 625 \text{ km}$ offset) the dominant P-wave velocities do not increase above 6.5 km/s . The minimum Moho depth in this region is 32 km . Thickened crust of about $\sim 32 - 35 \text{ km}$, together with the observed low velocities in the crust supports the interpretation that the crust in this block has a continental origin. This is consistent with several investigations ([Ben-Avraham et al., 2002](#); [Koulakov and Sobolev, 2006](#); [Robertson, 1998b](#)). The velocities in this region are in line with the suggestion

that the predominant lithology in the sediments is limestone (Robertson (1998b), see Fig. 2.1).

Ben-Avraham et al. (2002) suggested a lower crust beneath the ESM of 10 km thickness and a P-wave velocity of 6.7 km/s. The lower crust region beneath the ESM is subdivided into two parts. The northern part has a lower crust with P-wave velocities of 6.5 – 6.65 km/s. In contrast to this and in contrast to the results of Ben-Avraham et al. (2002) and Makris et al. (1983) the southern part shows no lower crust with P-wave velocities greater than 6.5 km/s. This division is also implied by the Moho depth which decreases from the southern part (35 km) to the northern part (32 km) of the ESM. These lateral changes are new observations and contribute new information to reveal the crustal structure of the collision zone between the ESM and Cyprus.

(III) North of the ESM

North of the ESM ($\sim 475 - 525$ km offset) the P-wave velocity structure differs significantly compared to the crustal structure beneath the ESM. In the upper crust a northward thickening of low velocities (< 4.8 km/s) can be observed which is connected to a thickening of the sediment layer. The tomographic P-wave velocity model reveals that this low velocity zone has a triangular shape with a northward dipping base down to a depth of ~ 12 km. These observations lead to the interpretation that this low velocity zone represents the accretionary wedge corresponding to the subduction of the crustal fragment of the ESM. This is consistent with the borehole data and interpretations from Robertson (1998b) (Fig. 1.5a) that between the ESM and Cyprus a northern basin exists filled with Pliocene-Quaternary turbidites and sandy sediments.

The accretionary wedge is underlain by a thin 5.5 – 6.5 km/s layer followed by a thick ($\sim 15 - 20$ km) layer with P-wave velocities ranging from 6.5 – 7.0 km/s. The northward continuation of this layer could not be resolved with the tomographic velocity model, but the layered model shows some evidence for a continuation of oceanic or thinned continental crust there.

(IV) Beneath Cyprus

In contrast to previous seismic refraction investigations (Makris et al., 1983) which suggest a 35 km thick continental crust beneath Cyprus which extends to the ESM, this study reveals that the region beneath Cyprus has a significantly different crustal composition compared to the crustal structure of the ESM. Therefore these crustal blocks are disconnected and have to be analyzed and interpreted independently.

The most prominent feature of the area beneath Cyprus is a high velocity zone. Geologically it is interpreted as an ophiolite sequence with weathered gabbros at the surface and peridotite at the bottom of the sequence. This is the first time that the geometry and the P-wave velocity distribution of the ophiolite sequence corresponding to the Troodos complex beneath Cyprus has been mapped in the N-S direction across the centre of the complex.

The P-wave velocities beneath Cyprus connected to the ophiolite complex range from 5.8 km/s at the surface to 7.6 – 8.0 km/s at 10 km depth beneath southern Cyprus. Further to the south, offshore Cyprus, velocities of 7.6 - 8.0 km/s are also encountered at 7 km depth. The initial P-wave velocity model had P-wave velocities of 6.75 km/s (combination of the results from Mackenzie et al., 2006; Smith and Vine, 1989 and Salisbury et al., 1989) at the surface in southern Cyprus corresponding to the Gabbro unit of the ophiolite complex. The final velocity model reveals that the P-wave velocities in this region are 5.8 – 6.5 km/s which can be explained by a weathered lithology. The wide-angle investigation by Mackenzie et al. (2006) estimated that the gabbros have a P-wave velocity of 6.05 – 6.67 km/s which is also below the average P-wave velocity of the gabbros (6.95 km/s) obtained by Smith and Vine (1989) from borehole measurements.

The area below 20 km depth is poorly constrained, but the velocity model indicates P-wave velocities around 7 km/s which would be in contrast to the result of Makris et al. (1983) who suggested a continental crust with a velocity of 6.0 km/s in the upper crust and 6.7 km/s in the lower crust. The high velocities of 7 km/s derived in this study could be a continuation of the lower crust revealed beneath the area north of the ESM.

4.2 Layered Velocity Model

Firstly, six 1-D velocity functions were derived manually for both land shots and for two airgun shots (CSP45 and CSP156) just south of Cyprus (Tab. 4.4). For each shot point a 1-D velocity model to the north and to the south was derived from the data by fitting by eye a linear function to the picked first arrival times. The slope of this function corresponds to the slowness (inverse of the P-wave velocity) within the layer (see Fig. 2.3). As the slope changed constantly a sub-division was made to define discrete layers with different P-wave velocities. The layer thickness can then be calculated with the known intercept time (see Equation 2.8).

TABLE 4.4: Initial 1-D velocity models for the onshore part (Turkey and Cyprus), LT = Layer Thickness, LS = Land Shot, AGS = Airgun Shot

LS 2002 (northern land shot)		LS 2001 (southern land shot)		CSP45 (AGS)		CSP156 (AGS)					
to North		to South		to North		to South		to North		to North	
V_p [km/s]	LT [km]	V_p [km/s]	LT [km]	V_p [km/s]	LT [km]	V_p [km/s]	LT [km]	V_p [km/s]	LT [km]	V_p [km/s]	LT [km]
2.83	3.15	3.53	2.54	5.45	4.36	5.57	13.79	3.57	3.33	3.64	6.07
5.45	7.26	5.49	10.90	6.06	23.19	7.87		5.41	2.70	6.21	3.64
6.67		6.77	33.25	6.88				8.39		8.19	
		8.07									

With these 1-D P-wave velocity models a simple layered starting model for the following ray-tracing procedure was constructed. From geological information on Turkey (Fig. 1.3) and high resolution geological maps the boundary between the sediment unit and the Taurides was derived (at a distance of about 180 - 190 km along the profile, see Fig. 4.13). This information was used to build the initial layered model for the onshore part (Turkey).

A subsequent trial-and-error forward modelling was performed to minimize the difference between observed traveltimes and calculated traveltimes. The comparison was done by eye. The main features which were modified are the P-wave velocity and the geometry of the layer boundaries. All in all 65 different versions of the layered model exists.

Since both types of seismic phases, refracted phases and reflected phases, had to be modeled, an alternating fitting of the data was necessary. The modifications of the P-wave velocity model made based on the refracted phases, also had to fit to the reflected phases and vice versa.

201 traveltimes were picked for the refracted phases (111 for the northern land shot and 90 for the southern land shot). 28 traveltimes were picked for the reflected phases beneath Cyprus (18 for the upper reflector and 10 for the lower reflector) and 56 traveltimes were picked for the reflected phases recorded by the northern land shot.

4.2.1 Results

The final layered P-wave velocity model for the area beneath Turkey, the Cilicia basin and northern Cyprus consists mainly of eight crustal units (Table 4.5). The RMS value for the 201 refracted arrivals for this model is 0.25 s.

TABLE 4.5: Final layered P-wave velocity model. Units are labeled in Fig. 4.13.

layer number	layer name	V_p [km/s]	Thickness [km]
a	Sediments beneath Turkey	2.8 - 3.6	1.5 - 3.0
b	Sediments beneath the Cilicia Basin / N. Cyprus (from gravity)	4.75 - 5.15	
c	5.5 layer	5.5 - 5.8	1.5 - 5.0
d	Upper Crust	6.0 - 6.7	27.0 - 37.0
e	Lower Crust	7.0 - 7.6	6.0 - 15.0
f	Upper Mantle	7.8	
g	Subducting plate	6.8	15.0 - 20.0
h	Lower ophiolite complex	7.5	0 - 4.0

As shown and labeled in Fig. 4.13 the key observations and first geological interpretations of the layered P-wave velocity model are:

- i) An upper and lower crust with large lateral changes in velocity structure and thickness (see Table 4.5 and Fig. 4.13). The highest lateral velocity change is observed within the sedimentary layer beneath the northern land shot (from 2.8 km/s at the northern end up to 3.5 km/s at about 40 km offset). As already seen from the initial 1-D velocity models (Table 4.4) the lateral P-wave velocity change is about 0.7 – 0.8 km/s . The lateral P-wave velocity change in the upper and lower crust generally does not exceed 0.3 km/s .
- ii) The seismic data are compatible with a Moho depth of 38 km at the northern end of the profile which increases southward to 45 km in combination with an upper mantle P-wave velocity of 7.8 km/s .

- iii) A subducting plate has been modeled with two reflected phases recorded by the Cyprus stations (Fig. 4.14b). The dip of the upper boundary is less than the dip of the lower boundary (Moho).

The sediment layer (**a** in Fig. 4.13) thins southwards from 3 to 1.5 *km* thickness. At an offset of 185 *km* the sediment layer disappears. This marks the boundary between the sediment filled basins of central Anatolia (Konya basin, TuzGözü basin, see Fig. 1.3) and the Taurus mountains which extends to the southern coast of Turkey.

The sedimentary layer is underlain by a layer with a predominant P-wave velocity of 5.5 *km/s* ("5.5 layer", **c** in Fig. 4.13). This layer has a thickness of 3 *km* at the northern end of the profile and thins significantly between 100 - 150 *km* offset (1.5 *km* thickness). In addition to the thinning of the layer, an increasing P-wave velocity (5.75 *km/s*) is observed. With the disappearance of the sedimentary layer at an offset of 185 *km* the 5.5 layer is present at the surface in the area of the Taurus mountains to the southern coast of Turkey. Beneath the Taurus mountains this layer has a constant thickness of 5 *km*.

Below the 5.5 layer a layer with a thickness of 27 *km* at the northern end of the profile and dominant P-wave velocities of 6.0 – 6.7 *km/s* is modeled. This layer is interpreted as the upper crust (**d** in Fig. 4.13). As already observed in the 5.5 layer a high velocity zone at an offset between 100 – 150 *km* offset can be observed. The P-wave velocities increase up to 6.3 *km/s* at the upper boundary of the layer and 6.7 *km/s* at the lower boundary of the layer between 100 and 150 *km* offset. Simultaneously the layer thickness increases from 27 *km* to 37 *km*. The geometry of the layer boundary between the upper and lower crust is mainly derived from the reflected phases of the northern land shot. The rapid increase of the depth from 32 *km* to 39 *km* of this boundary is necessary to fit the data in an appropriate way. The significant increase in P-wave velocity in the southernmost part of the upper crust (up to 7.2 *km/s*) is needed to fit the calculated traveltimes of the P_g phase recorded on Cyprus with the picked traveltimes. This area belongs more likely to the lower crust than to the upper crust due to the similar P-wave velocity (7.2 *km/s*).

The lower crust with a dominant P-wave velocity of 7.0 – 7.1 *km/s* has a constant thickness of 6 *km* from the northern end of the profile to the central part of the profile (**e**

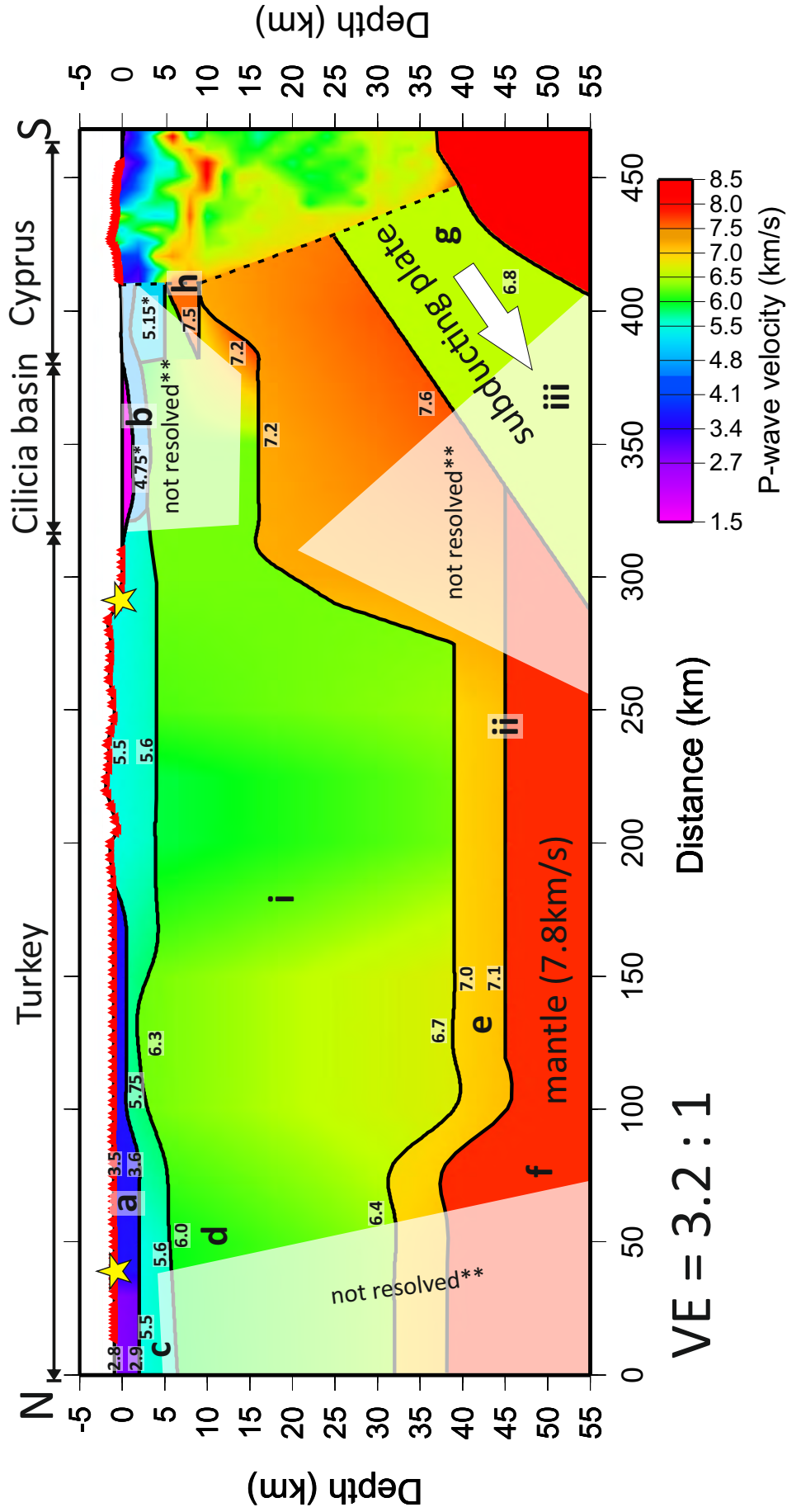


FIGURE 4.13: Final layered velocity model with labeled layers (a-h) and main observations (i-iii, see text). Numbers indicate P-wave velocity (* P-wave velocity corresponds to the density from gravity model), black dashed line shows boundary between layered model and tomographic model, yellow stars indicate locations of land shots. Plot has a vertical exaggeration (VE) of 3.2 : 1, ** = area not resolved by seismic phases, but resolved by gravity modelling.

in Fig. 4.13). In the southern part of the profile, between 275 km and 300 km offset, the thickness of the lower crust rapidly increases (up to $\sim 15 - 20$ km). Within the depth range of 15 – 35 km beneath the Cilicia basin high P-wave velocities of 7.2 – 7.6 km/s are observed. This includes a high velocity block of 7.5 km/s which corresponds to the ophiolite complex beneath Cyprus. This is mainly derived from the refracted and reflected waves of the southern land shot recorded by the Cyprus stations (Fig. 4.14 a and b).

A P_n phase from the northern land shot (Fig. 4.14a) reveals a P-wave velocity of 7.8 km/s for the upper mantle with a Moho at 38 – 45 km depth (f in Fig.4.13). Furthermore the PmP phase confirmed a Moho depth of 45 km beneath the central part of the profile. At the northern end of the profile the Moho shallows to 38 km depth in order to fit the gravity data. The PmP phase is observed and picked at the northern land shot in an offset of 190 - 270 km (Fig. 4.15). The PcP phase is picked at an offset of 130 – 190 km, although the arrivals between 160 and 190 km offset could belong to either the PcP or PmP phase (Fig. 4.15).

Two reflected phases from the southern land shot recorded by the Cyprus stations give evidence for a northward subducting plate (g in Fig. 4.13). The subducting slab has an average P-wave velocity of 6.8 km/s and a thickness of 15 – 20 km, which provides a good agreement between the observed and calculated traveltimes of the later reflected phase (P_{SUB-LO} in Fig. 4.17) and is confirmed by the gravity modelling. The earlier phase is supposed to be the reflected signal from the upper boundary of the subducting plate. Compared to the lower boundary it is shallow dipping. The later phase is interpreted as the Moho reflection from the subducting plate. The dip of the lower boundary (Moho) is significantly different (more steep, compare P_{SUB-LO} and P_{SUB-UP} in Fig. 4.17). These reflected phases, supposed to be the reflections from the upper boundary and the Moho of the subducting plate, are discussed in more detail in the following section 4.2.3.

The first arrivals from the southern land shot recorded by the Cyprus stations constrain the existence of high P-wave velocities (7.2 – 7.5 km/s) beneath the Cilicia basin (below ~ 15 km depth) and northern Cyprus. Considering the high velocity zone beneath southern Cyprus from the tomographic P-wave velocity model, a triangular shaped high

velocity block (**h** in Fig. 4.13) is suggested as the northern end of the lower part of the ophiolite complex beneath Cyprus.

As shown in Fig. 4.14a the P-wave velocity model involves refracted phases from the upper 15 km and a *Pn* phase from the Moho at 38 – 45 km depth. A refracted phase is also observed on the Cyprus stations. The refracted phases mainly constrain the P-wave velocity distribution in the upper 15 km beneath Turkey, the upper mantle velocity and the P-wave velocity of the region beneath the Cilicia basin at 15 km depth.

The intra-crustal reflected phases (Fig. 4.14b) constrain the geometry of the layer boundary between upper and lower crust and the *PmP* phases confirm the geometry of the Moho. The reflected phases recorded by the Cyprus stations constrain the upper boundary and the Moho of the subducting plate.

By perturbing the velocities or the layer boundaries in the model one can obtain a feel for the errors in the various parameters by examining the changes in the traveltime curves. Thus the velocities in the upper 15 km beneath Turkey are probably accurate to within ± 0.1 km/s. The velocities throughout the remainder of the layered model are thought to be accurate to within ± 0.2 km/s while the boundary depths are thought to be accurate to within ± 10 %.

Due to the distribution of the seismic phases, there are three regions where the P-wave velocity model is not resolved by the wide-angle seismic data (Fig. 4.13). However, the subsequent gravity modelling revealed the crustal structure of these regions, especially the area between Turkey and Cyprus.

4.2.2 Picked vs. calculated traveltimes

To compare the observed and picked traveltimes with the calculated traveltimes both were plotted onto the data. Figures 4.15 and 4.16 show the seismic section and the synthetic seismogram section of the northern land shot, respectively, with the picked traveltimes (red dots) and the calculated traveltimes of first arrivals and reflections (green dashed and solid lines) of the final layered P-wave velocity model. Figure 4.17 shows the corresponding seismic section of the southern land shot. From the northern land shot (Fig. 4.15) a *Pg* and *Pn* phase were picked and modeled. The calculated traveltimes of the first arrivals (green solid line in Fig. 4.15) are in good agreement with the picked

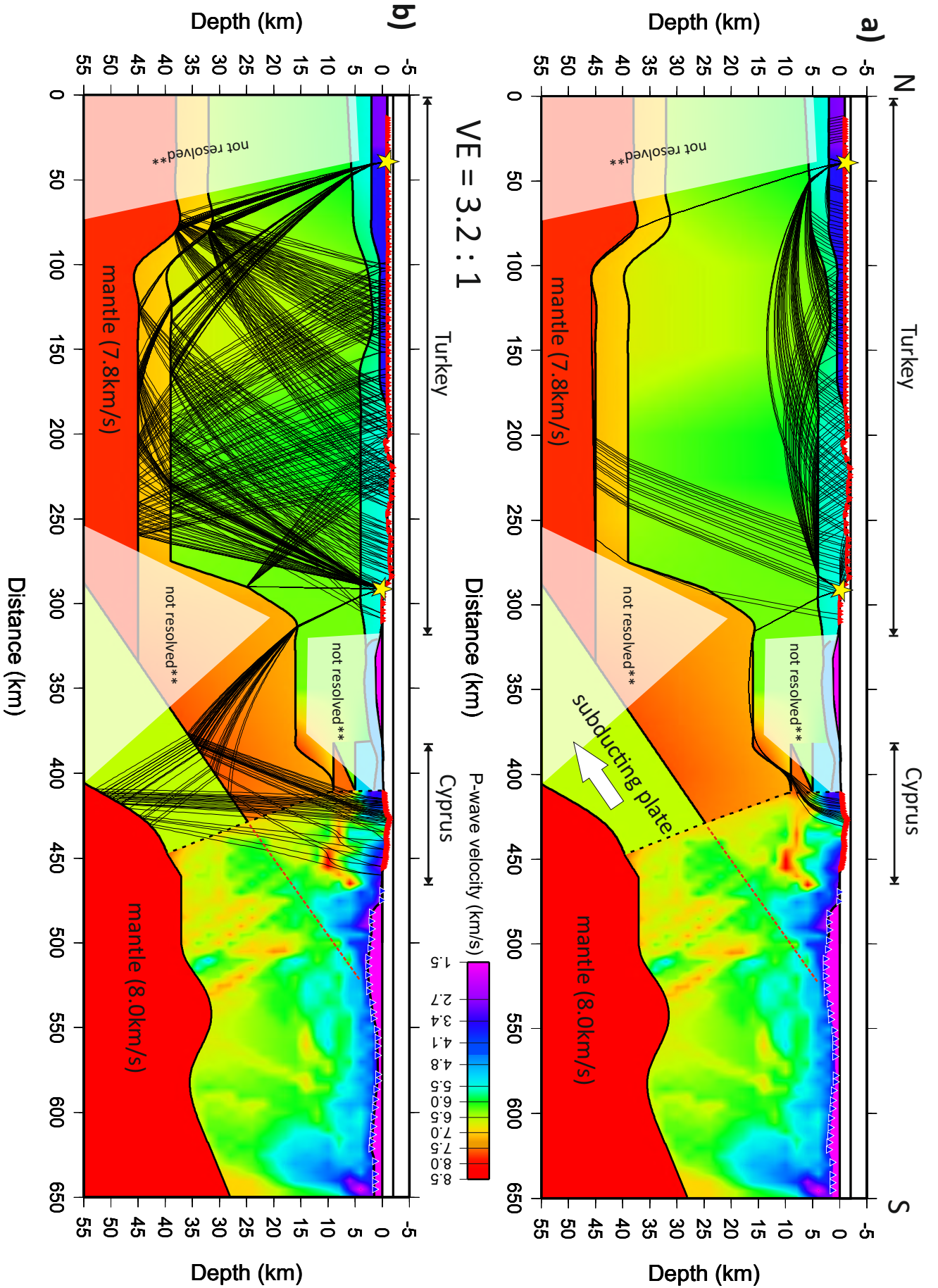


FIGURE 4.14: Final layered velocity model in which modeled refractions (a.) and reflections (b.) are shown. Black dashed line shows boundary between layered model and tomographic model, red dashed line represents the top of the subducting plate in the tomography model and yellow stars indicate locations of land shots. Both cross sections have a vertical exaggregation (VE) of 3.2 : 1.

traveltimes (red dots in Fig. 4.15). Although the final layered P-wave velocity model minimizes the difference between the picked and calculated traveltimes as far as possible, at an offset of about 50 – 70 km a slight difference between both is observed. The rapid change in slope of the picked first arrivals, which is hard to model at all, is caused by a rapid lateral change in velocity structure. The final layered P-wave velocity model (Fig. 4.13) accounts for the rapidly changing slope of these first arrivals by lateral thinning of near-surface low velocity layers and a high-velocity block within the upper crust (see Fig. 4.13 at an offset of about 100 km). These features, already presented in the previous section, contribute to the fitting of picked and calculated first arrivals.

As shown in Fig. 4.15 two reflected phases are modeled. This includes the reflections from the layer boundary between the upper and lower crust (PcP) and the reflections from the crust-mantle boundary (PmP). Due to the signal to noise ratio the reflected phases can be picked at offsets greater than 130 km.

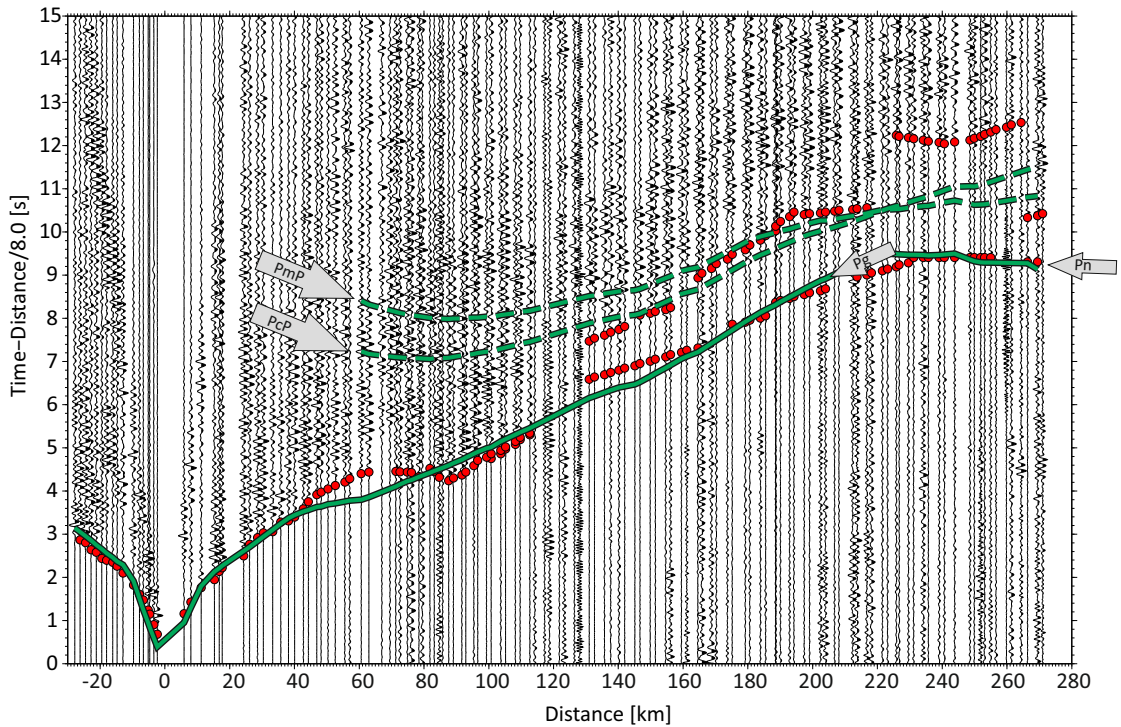


FIGURE 4.15: Seismic section of northern land shot in Turkey (T2002), band-pass filtered from 3 – 9 Hz. Red circles show picked first arrival times and reflected phases. Green solid lines show calculated first arrival times (Pg and Pn) and green dashed lines show calculated traveltimes from reflected phases from the upper / lower crust boundary (PcP) and from the Moho (PmP) based on the final layered P-wave velocity model (Fig. 4.13).

As mentioned in section 3.3 the onset of the reflected phases has a higher signal to noise ratio compared to the first arrivals and is therefore better visible. To analyze and verify

the energy relationship between the first arrivals and the reflected phases, synthetic seismograms based on the final layered P-wave velocity model were calculated for the northern land shot (Fig. 4.16). During a trial-and-error procedure different synthetic seismograms with different velocity gradients and combinations for the upper crust and lower crust were calculated. Based on these results the P-wave velocity of the lower crust is determined to be 7.0 km/s and the vertical P-wave velocity change in the upper crust is determined to be 0.4 km/s ($6.0 - 6.4 \text{ km/s}$ and $6.3 - 6.7 \text{ km/s}$). The velocity contrast between the upper and lower crust is therefore 0.6 km/s in the northern part ($< 100 \text{ km}$ offset) and 0.3 km/s in the central part of the profile ($100 - 250 \text{ km}$ offset, see Fig. 4.13).

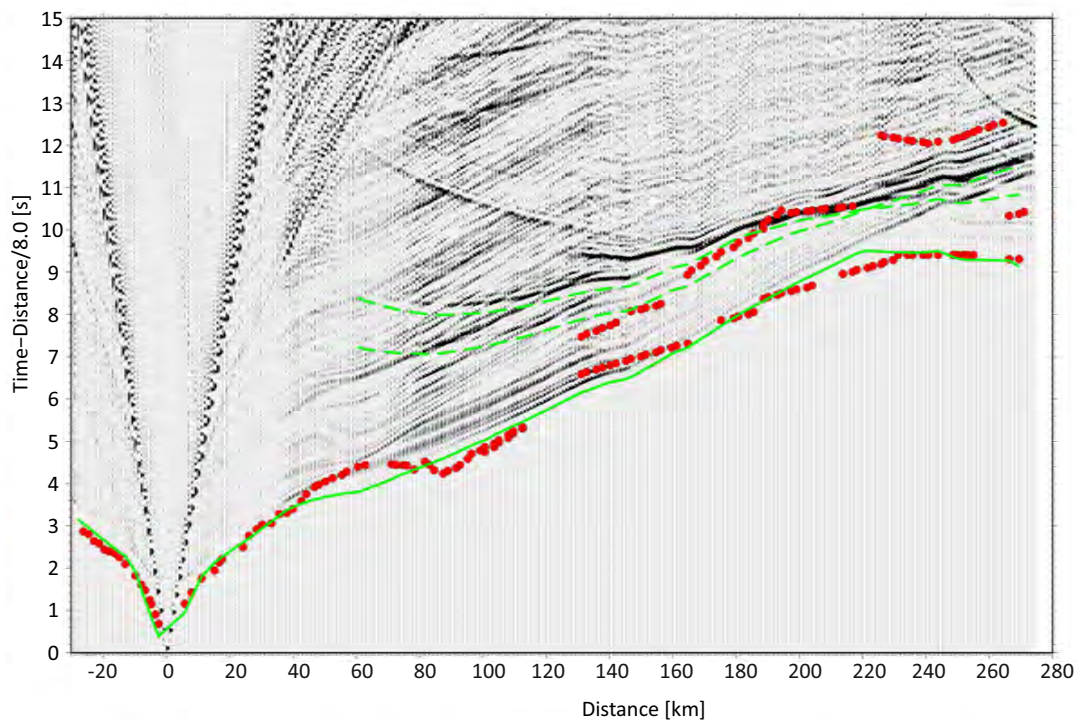


FIGURE 4.16: Synthetic seismogram section of northern land shot in Turkey (T2002). Red circles show picked first arrival times and reflected phases, green solid lines show calculated first arrival times, green dashed lines show calculated traveltimes from reflected phases.

The calculated first arrivals of the southern land shot (green solid line in Fig. 4.17) show a good fitting to the real data and the picked arrival times. To the north of the southern land shot, the calculated traveltimes of the two reflections (PcP and PmP), already observed from the northern land shot, can be observed. In contrast to the northern land shot, here no reflections were picked due to the low signal to noise ratio. The above

mentioned reflections recorded by the Cyprus stations are shown as green dashed lines in Fig. 4.17 (Offset = 120 - 170km). Note the difference in slope of both reflected phases which originates from the different dip angles of the reflectors.

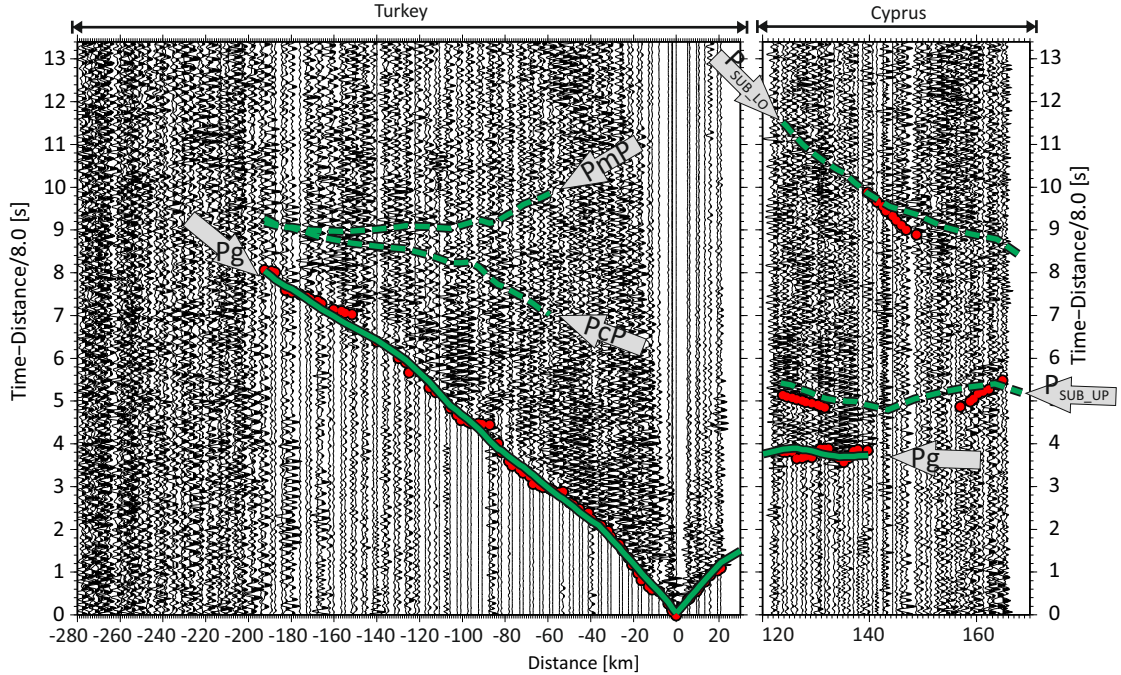


FIGURE 4.17: Seismic section of southern land shot in Turkey (T2001), band-pass filtered from 3-9 Hz. Red circles show picked first arrival times and reflected phases. Green solid lines show calculated first arrival times (Pg) and green dashed lines show calculated traveltimes from reflected phases from the upper / lower crust boundary (PcP), from the Moho (PmP), both not picked, and from the upper boundary (P_{SUB-UP}) and the Moho (P_{SUB-LO}) of the subducting plate, based on the final layered P-wave velocity model (Fig. 4.13),

4.2.3 Discussion

The wide-angle seismic data provide evidence for a lateral, southward change in crustal composition. Based on the change in geometry of the upper / lower crust boundary and the simultaneous change of upper crustal velocity, the crustal unit is divided into two parts (at about 100 km offset). The northern part has an upper crustal thickness of 27 km, upper crustal P-wave velocities of 6.0 – 6.4 km/s and a lower crustal thickness of about 13 km. The southern part has an upper crustal thickness of 37 km, upper crustal P-wave velocities of 6.3 – 6.7 km/s and a lower crustal thickness of about 6 km. Based on geological information (Fig. 1.3) this change in crustal structure is consistent with the boundary between the Central Anatolian Crystalline Complex in the north and the Menderes-Taurus platform in the south (Okay, 2000, 2008; Clark and Robertson,

2002; Görür et al., 1998; Dilek and Sandvol, 2009). These crustal units are divided by the inner Tauride suture which is located at an offset of about 100 km along the profile. The inner Tauride suture not only marks the boundary between the crustal blocks, but also marks the boundary between the TuzGölü basin and the Konya basin (see Fig. 1.3). According to Roberts et al. (1999) the sedimentary unit within the Konya basin is about 500 m thick, whereas the sedimentary unit of the TuzGölü basin is estimated to have 3 km thickness (Gürbüz and Evans, 1991). This significant southward thinning of the sedimentary unit is confirmed by the wide-angle data presented in this study. The crustal structure beneath the northern end of the profile is in good agreement with a basement depth of 2 – 3 km revealed by seismic studies and well data of Gürbüz and Evans (1991), Aydemir and Ates (2006a) and Fernandez-Blanco et al. (2013).

The results of the wide-angle seismic modelling revealed that a Moho depth of 38 km for the northern part of the profile and 45 km for the central part of the profile is compatible with the data as long as the upper mantle P-wave velocity is 7.8 km/s. As soon as a normal mantle velocity of 8 km/s is suggested, the Moho has to be deeper (~ 48 km) with the same crustal velocity distribution.

The Pn velocity distribution from the work of Mutlu and Karabulut (2011) and Gans et al. (2009) reveals a low velocity zone (Pn velocities between 7.75 – 7.9 km/s) in the area between the TuzGölü basin and the southern coast of central Anatolia, coinciding with the Neogene-Quaternary volcanism of the Central Anatolia Volcanic Zone (CAVZ). This is in agreement with the upper mantle velocity of the wide-angle seismic investigation presented here.

Vanacore et al. (2013) suggested Moho depth values varying from 31 to 45 km for the central Anatolian block. Due to the scarcity of seismic stations deployed in this region the values are not well constrained. Other investigations of receiver functions (Tezel et al., 2013) suggest a Moho depth of 36 – 40 km in the area between the TuzGölü basin and the southern coast of central Anatolia, which is confirmed by the results presented in this study at least for the region beneath the TuzGölü basin (northern end of the profile). As mentioned the spatial distribution of the used seismic stations in the area of southern central Anatolia (area between the TuzGölü basin and the southern coast of central Anatolia) is very inappropriate to derive a well constrained Moho depth. Due to this the accurate determination of the Moho depth with wide-angle seismic investigations

such as presented in this study provides an important and significant insight into the crustal structure of southern Turkey and Cyprus.

The results of Pn tomography performed by [Mutlu and Karabulut \(2011\)](#) indicate a thickened crust of up to 40 – 48 km between the TuzGözü basin and the southern coast of central Anatolia. This southward thickening is also observed by the result presented here and can be attributed to the subduction of African lithosphere ([Mutlu and Karabulut, 2011](#)).

Due to the subducting plate beneath Cyprus and the Cilicia basin a southward thinning of the crust of the upper plate from the Anatolian plateau to Cyprus is observed. In addition to the thinning a change in crustal composition is observed. From the wide-angle seismic data no P-wave velocities typical of the upper crust ($\sim 6.0 - 6.7 \text{ km/s}$) are observed anymore (at a depth of 15 – 35 km, see [Fig. 4.13](#)). Instead the existence of a thick high velocity block is derived from the data. The lower boundary of this block marks the boundary to the subducting plate, which is constrained by the data. Based on the P-wave velocities and the geometry of the layer boundaries the high velocity block is interpreted as lower crust. Other authors such as [Ergün et al. \(2005\)](#); [Vanacore et al. \(2013\)](#) and [Koulakov and Sobolev \(2006\)](#) observed in the area of the Cilicia basin and Cyprus a thinned crust with the Moho at 20 – 30 km depth.

[Mackenzie et al. \(2006\)](#) suggested the existence of a deep reflector at $\sim 55 \text{ km}$ depth beneath Cyprus, which could originate from the northward dipping slab. The wide-angle seismic line of [Mackenzie et al. \(2006\)](#) crosses the profile presented in this study at an offset of about $\sim 415 \text{ km}$ (see [Fig. 1.3](#)). Based on the crustal model presented in this study the reflection of [Mackenzie et al. \(2006\)](#) could originate from the Moho of the subducting plate.

To test the hypothesis that the first reflected phase recorded by the Cyprus stations originates from the upper boundary of the subducting plate, a polarity analysis was performed of the first arrivals and first reflection. The subducting plate represents a low velocity zone, and thus the reflections from this upper boundary should show the opposite polarity to that of the first arrivals. To maximize the clarity of the onset the traces were stacked. The analysis shows that the polarity of the onset of the shallow reflection is opposite to the polarity of the first arrivals. Thus it is confirmed that this

reflection comes from the top of a low velocity zone which is consistent with the predicted model of a shallow dipping crust beneath Cyprus.

The average P-wave velocity of 6.8 km/s and the thickness of the subducting slab of $15 - 20 \text{ km}$ supports the hypothesis that the origin of the crust of the subducting slab is different compared to the crustal block of the ESM. Since the ESM is interpreted as a continental block, the northward continuation which subducts beneath Cyprus is interpreted as having more of an oceanic affinity.

At the southern end of the layered P-wave velocity model a block with a velocity of 7.5 km/s occurs. This high velocity block corresponds to the Troodos ophiolite complex, also modeled with the tomography. This block extends to the northern coast of Cyprus and disappears north of the coast. This is interpreted as the northern end of the Troodos ophiolite complex.

4.3 Gravity

To complement the wide-angle seismic investigation and to compare its results with another geophysical method, gravity modelling was performed along the seismic profile.

The gravity data were compiled from [Makris and Wang \(1994\)](#) for areas south of $37^\circ N$, from [Aydemir and Ates \(2006b\)](#) for areas north of $37^\circ N$ and from [Gass and Masson-Smith \(1963\)](#) for Cyprus. These gravity values are the Bouguer gravity anomalies (circles in Fig. 4.19a) north of 460 km offset. Offshore, south of Cyprus free air gravity data, collected during the cruise MSM14/3, were available (circles in Fig. 4.19a) south of 460 km offset. Note that the water between Turkey and Cyprus is replaced by the reference density of 2.67 g/cm^3 , whereas the water south of Cyprus has the standard density of 1 g/cm^3 . At the northern edge of the study area gravity values from [Aydemir and Ates \(2006a\)](#) are available. They proposed densities of 2.4 g/cm^3 for the sedimentary fill and 2.65 g/cm^3 for the metamorphic basement.

To model the gravity data, first the derived P-wave velocities were converted into densities following Birch's law (Eq. 4.1). The densities for the crustal layers are calculated using the empirical relation ([Nafe and Drake, 1957](#); [Birch, 1961](#)):

$$\rho = 0.252 + 0.3788 * V_p \quad (4.1)$$

Table 4.6 shows the P-wave velocities of the different layers and the corresponding density which is used for the gravity modelling process. The P-wave velocities in each of the $5 \times 2 \text{ km}$ cells of the tomography model were also converted to density using the Birch law. Using the Birch law produces typical uncertainties of $\pm 0.02 \text{ g/cm}^3$ (Barton, 1986).

TABLE 4.6: Units of the layered P-wave velocity model and the corresponding density (calculated after Birch's law, Eq. 4.1)

layer number	layer name	V_p [km/s]	density [g/cm ³]
a	sediments beneath Turkey	2.8 - 3.6	1.56
b	sediments beneath the Cilicia basin / N. Cyprus (from gravity)	4.75 - 5.15	2.15 - 2.3
c	5.5 layer	5.5 - 5.8	2.43
d	upper crust	6.0 - 6.7	2.73
e	lower crust	7.0 - 7.6	3.0 - 3.1
f	upper mantle	7.8	3.3
g	upper subducting plate	6.8	2.92
g'	lower subducting plate		3.12
h	lower ophiolite complex	7.5	3.19

With the derived densities, a 2-D polygon model cross-section along the profile, based on the formula of Talwani et al. (1959) with finite-length strike (Cady, 1980), was built. Figure 4.18 shows the involved elements where P is the origin of an xz coordinate system and the polygon also lies in the xz plane.

The vertical component of gravitational attraction V , due to the whole polygon, is given by

$$V = 2G\rho \sum_{i=1}^n Z_i \quad (4.2)$$

where G is the universal constant of gravitation and ρ is the density of the body. The summations are made over the n sides of the polygon. The integral Z_i is expressed by

$$Z_i = a_i \sin\phi_i \cos\phi_i \left[\theta_i - \theta_{i+1} + \tan\phi_i \log_e \frac{\cos\theta_i(\tan\theta_i - \tan\phi_i)}{\cos\theta_{i+1}(\tan\theta_{i+1} - \tan\phi_i)} \right] \quad (4.3)$$

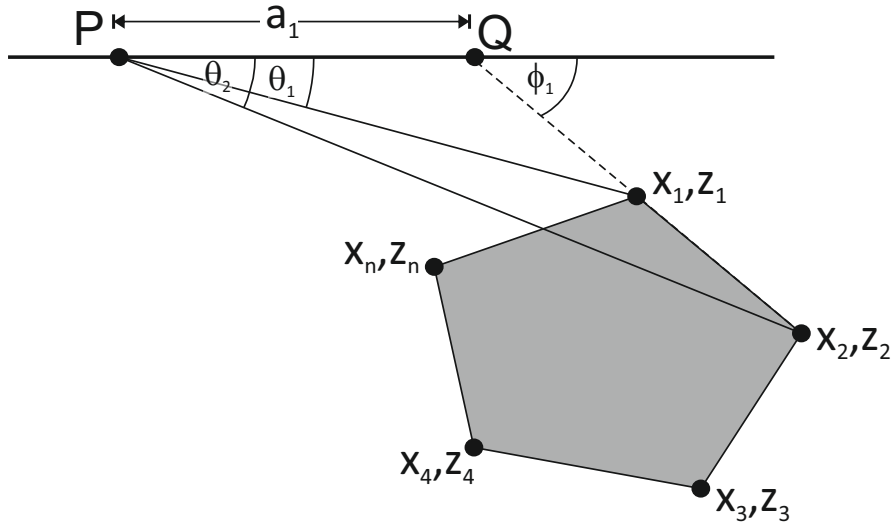


FIGURE 4.18: Geometrical elements involved in the gravitational attraction of an n-sided polygon, modified after [Talwani et al. \(1959\)](#)

where the corners of the polygon are used to obtain $\theta_i, \theta_{i+1}, \phi_i, a_i$

$$\begin{aligned}
 \theta_i &= \tan^{-1} \frac{z_i}{x_i}, \\
 \theta_{i+1} &= \tan^{-1} \frac{z_{i+1}}{x_{i+1}}, \\
 \phi_i &= \tan^{-1} \frac{z_{i+1} - z_i}{x_{i+1} - x_i}, \\
 a_i &= x_{i+1} + z_{i+1} \frac{x_{i+1} - x_i}{z_i - z_{i+1}},
 \end{aligned} \tag{4.4}$$

By systematic variation of the geometry (number and locations of vertices of the polygon) and density of the polygon, the misfit between calculated and observed gravity anomalies can be minimized.

Since the densities used for the gravity modelling correspond to the P-wave velocities derived by the velocity modelling (see Chapter 4.1 and 4.2), the gravity model has to be updated and rerun when the P-wave velocity model has changed and vice versa. Due to this an alternating fitting of both the gravity data and the seismic data leads to a final P-wave velocity model and gravity model which jointly constrain the crustal model.

The resulting gravity anomalies of the final gravity model (Fig. 4.19b) show a good agreement with the observed gravity anomalies (see Fig. 4.19a) along the whole 650 km long profile.

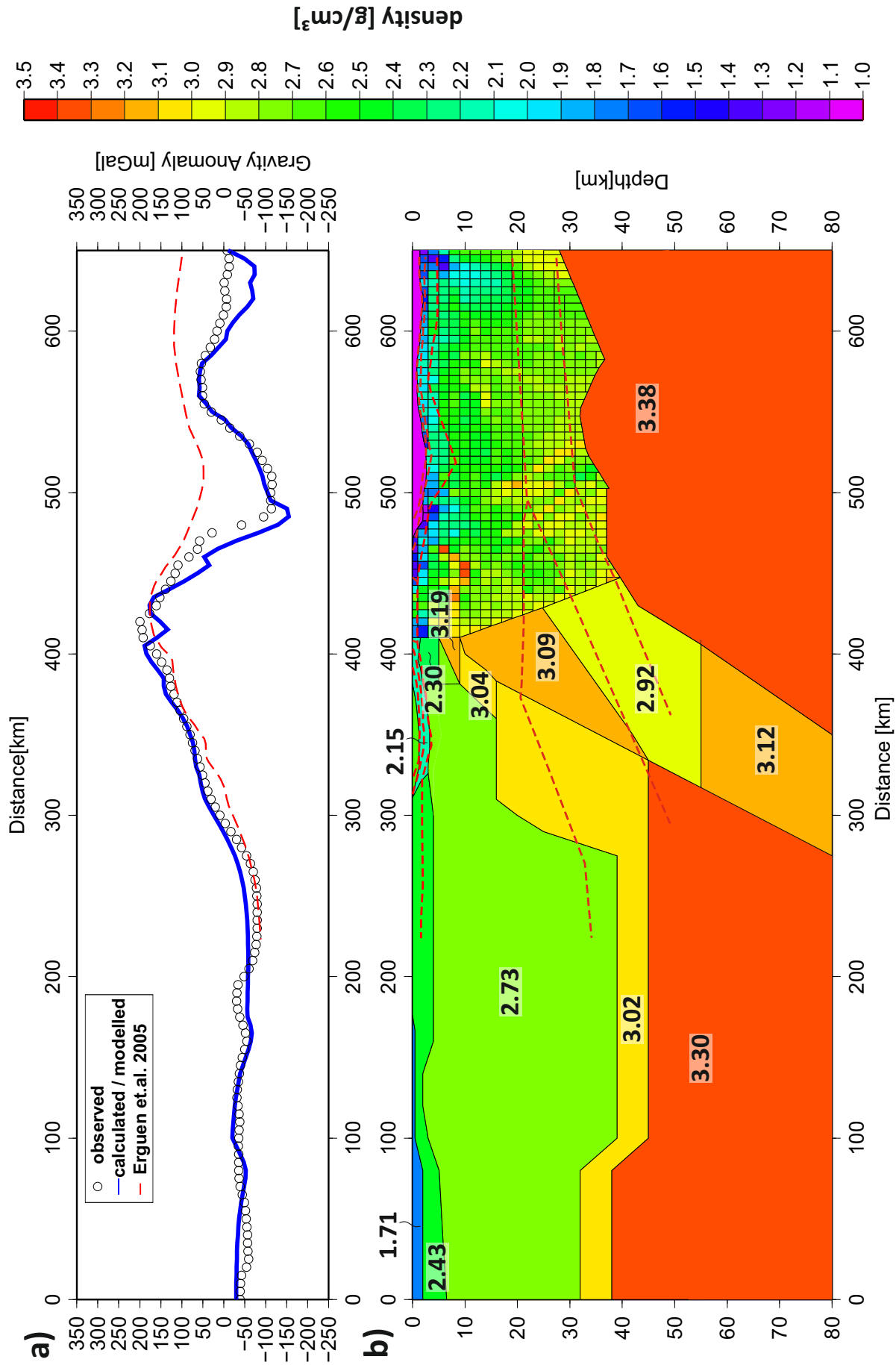


FIGURE 4.19: a) Observed gravity values (circles, from Makris and Wang, 1994; Aydemir and Ates, 2006b and Gass and Masson-Smith, 1963) compared to the calculated gravity values (blue line). Red dashed line shows gravity values from Ergün et al., 2005. b) Final gravity model. Numbers indicate density in g/cm^3 , red dashed lines are the boundaries of the model from Ergün et al., 2005.

To account for the lateral change of P-wave velocities in the upper and lower crust in the layered P-wave velocity model, the corresponding layer within the gravity model is divided into two parts. The southernmost part of the upper crust and the southernmost part of the lower crust are represented by two separate blocks with different densities (labeled with 3.04 g/cm^3 and 3.09 g/cm^3 in Fig. 4.19b).

The shallower part (above 55 km depth) of the subducting slab geometry is mainly defined by the observed reflected phases. The deeper part of the slab (below 55 km depth) is mainly derived from the gravity data. Within the modelling process different slab geometries were considered, of which a northward flat dipping slab with decreasing thickness and increasing dip angle with increasing depth is the most likely one. The misfit between the observed and calculated gravity anomaly is minimized as far as possible with the shown slab geometry (Fig. 4.19b).

4.3.1 Results and Discussion

The gravity low associated with the Taurus mountains and the Anatolian plateau in southern Turkey would be expected for continental crust in an elevated, mountainous area, even with a modest isostatic positive contribution (Ergün et al., 2005).

The decrease in gravity across the Cilicia Basin to Turkey is mainly caused by a thickening crust, reaching 45 km below the Anatolian plateau. In contrast to Vanacore et al. (2013) who suggested an average value of the depth to the Moho of 37 km in this region, the gravity data is not compatible with this value. The gravity data suggest a Moho depth of $\sim 45 \text{ km}$.

The sediment thickness of the Cilicia basin is estimated to comprise 1 km of Pliocene - Quaternary and Messinian sediments and at least 1 km of pre-Messinian sediments (Ergün et al., 2005). In the gravity model (Fig. 4.19b) this is taken into account by a 2 km thick layer with a P-wave velocity of 4.75 m/s and a density of 2.15 g/cm^3 .

The significant increase in gravity of about 150 mgal from 300 km to 400 km offset can be explained by the existence of a dense block in the deeper part beneath the Cilicia basin. The gravity model of Ergün et al. (2005) suggests a Moho at $20 - 30 \text{ km}$ depth in this area (see red dashed line in Fig. 4.19b). This is in contrast to the results of the gravity model based on the wide-angle seismic model presented in this study. As

shown in Fig. 4.19b the increase of the gravity value in this area is mainly caused by the increasing thickness of the lower crust (3.02 g/cm^3) with densities up to 3.09 g/cm^3 .

The most prominent feature of the gravity data is the gravity high (up to 200 mGal) above Cyprus ($400 - 430 \text{ km}$ offset). This is caused by the high densities of the Troodos ophiolite complex beneath Cyprus. The gravity low (-120 mGal) south of Cyprus at about 500 km offset is mainly caused by the low densities of the accretionary wedge.

One challenging question is still the dip angle of the deeper part of the subducting plate. As pointed out during the interpretation of the layered P-wave velocity model, including the reflected phases from the southern land shot, it is concluded that the upper boundary of the subducting plate has a different dip angle compared to the Moho of the slab. Finally the gravity modelling constrains a changing dip angle of the subducting plate where the deeper part (at $45 - 80 \text{ km}$ depth) of the slab dips steeper compared to the upper part (above 45 km depth). The comparison with the gravity model of Ergün et al. (2005) (red dashed lines in Fig. 4.19b) shows a few similarities to the crustal model presented here. For example, the Moho derived by Ergün et al. (2005) is located at about the same depth, starting in the south at 28 km and increasing northwards. Nevertheless, the Moho geometry revealed by the combined analysis of wide-angle seismic and gravity data contains many more details and shows a higher variability. Confirmed by the crustal model presented in this study, the model of Ergün et al. (2005) predicts a shallow subducting plate (above 50 km depth) with a density of 3.0 g/cm^3 . In addition to the results of Ergün et al. (2005), the analysis of the gravity data presented in this study reveals that the dip angle and the density of the subducting slab increases with depth (from 2.92 g/cm^3 to 3.12 g/cm^3).

Due to thinner sediments on the top of the ESM, the continental block of the ESM causes a gravity high at about $550 - 590 \text{ km}$ offset.

Besides confirming the seismic model, the gravity data could contribute new structural information such as the crustal structure of the region beneath the Cilicia basin, which is only poorly resolved by the seismic data. In addition, the gravity modelling gives some evidence for a shallow subducting plate, which still exists beneath south Turkey at a depth of $60 - 80 \text{ km}$, which is greater than the maximum depth that the P-wave velocity model from the wide-angle seismic data could resolve.

4.4 Line Drawing Migration

As introduced in section 2.1 a wide-angle seismic experiment as presented in this study has a different purpose compared to conventional reflection seismic investigations. Nevertheless with some limitations it is possible to use the data achieved from the wide-angle seismic experiment for imaging reflective structures in the upper crust. The limitations are mainly related to the absence of multiple subsurface coverage (multifold seismic data), which makes stacking the data impossible. For this reason, instead of classical seismic stacking, a pre-stack imaging method is applied to the wide-angle seismic data. Due to this methodology no continuous reflective structures in the upper sediments can be expected.

To extend the existing information about the crustal structure of the offshore part south of Cyprus with another geophysical method a newly introduced pre-stack line-drawing migration method was performed (Bauer et al., 2013). This method was developed by adopting the established concept of the Fresnel volume migration (Yoon et al., 2003; Buske et al., 2009), and migrating line segments instead of waveforms. The pre-stack line-drawing migration method provides depth sections with line segments representing reflective structures derived directly from the data instead of full waveform images as delivered by Fresnel volume migration (Bauer et al., 2013).

To extend the already modelled upper crustal reflection further north (Fig. 4.8) and to reveal a detailed subsurface structural image of the accretionary wedge and the top of the subducting plate eight ocean bottom seismometer stations south of Cyprus (nos. 20,21,22,24,25,28,29,30) were chosen for the pre-stack line drawing migration.

The first step of the procedure is the individual preparation of the seismic data. This data processing includes band-pass filtering (Ormsby zero phase, corner frequencies: 2 Hz, 5 Hz, 25 Hz and 30 Hz), deconvolution (traditional Wiener-Levinsons spiking deconvolution, automatic gain control (operator length of 500 ms), 80 ms operator length, time window: 0 – 15000 ms), trace equalization and bottom mute. As an example, the seismic section of station no. 24 is shown in Fig. 4.20 with all applied processing steps as the input data for the further procedure.

In a second step a semblance analysis is performed to detect coherent events and to determine the local slowness of the wavefield. This analysis is only performed between

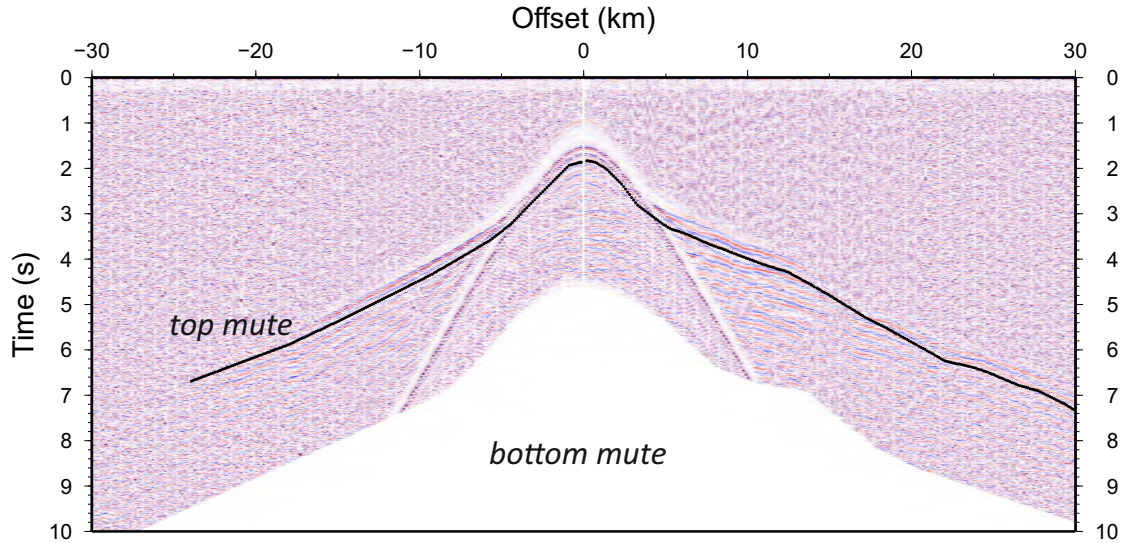


FIGURE 4.20: Example of input data (OBS 24) for pre-stack line-drawing migration. The section has been band-pass filtered (Ormsby zero phase, corner frequencies: 2 Hz, 5 Hz, 25 Hz and 30 Hz), deconvolution (traditional Wiener-Levinson spiking deconvolution, 80 ms operator length) and an automatic gain control (operator length of 500 ms) and trace equalization have been applied. Top and bottom mute have been used during semblance analysis.

the top mute (to exclude the first arrival) and the bottom mute (to exclude multiple phases; see Fig. 4.20).

The final step consists of pre-stack depth migration which is performed for every coherent event and includes:

- i) determination of isochrone (trajectory of potential reflection points),
- ii) ray-tracing from the shot location (using slowness and velocity at shot location) down to the reflection point at the isochrone and
- iii) calculation of the reflector dip

The result of the pre-stack line drawing migration shows reflective structures at 5 – 22 km depth at the northern end of the studied region (at 490 km offset) and reflective structures at 5 – 15 km depth beneath the southern end at 550 km offset. Thus the bottom of the reflective structures in the upper crust (lower red dashed lines in Fig. 4.21) apparently dips northwards. In addition many reflective segments show a northward dip angle, which follows the dip of the suggested upper boundary of the subducting plate (upper red dashed line in Fig. 4.21). Due to the applied bottom mute (see Fig. 4.20) the maximum resolved depth is confined as shown in Fig. 4.21 (not resolved area is masked).

At an offset of 525 – 530 km and a depth of 5 – 10 km the reflective segments show a dip which is parallel to the dip of the already modelled reflection from the wide-angle seismic data (red-white dashed line in Fig. 4.21). Beneath the accretionary wedge reflective structures are observed along the 5.5 km/s isoline which probably defines the boundary between the sedimentary unit and the crystalline basement (grey bar in Fig. 4.21) and therefore constrains the geometry of the accretionary wedge. Thus the results of the pre-stack line drawing migration support the results of the wide-angle seismic modelling by confirming the geometry of the accretionary wedge and the upper crustal reflection. They also provide further evidence for a northward dipping crust beneath the offshore region south of Cyprus. As shown in Fig. 4.21 the northward continuation of the modelled upper crustal reflection and multiple northward dipping reflective structures which are assigned to the northward subducting plate are revealed.

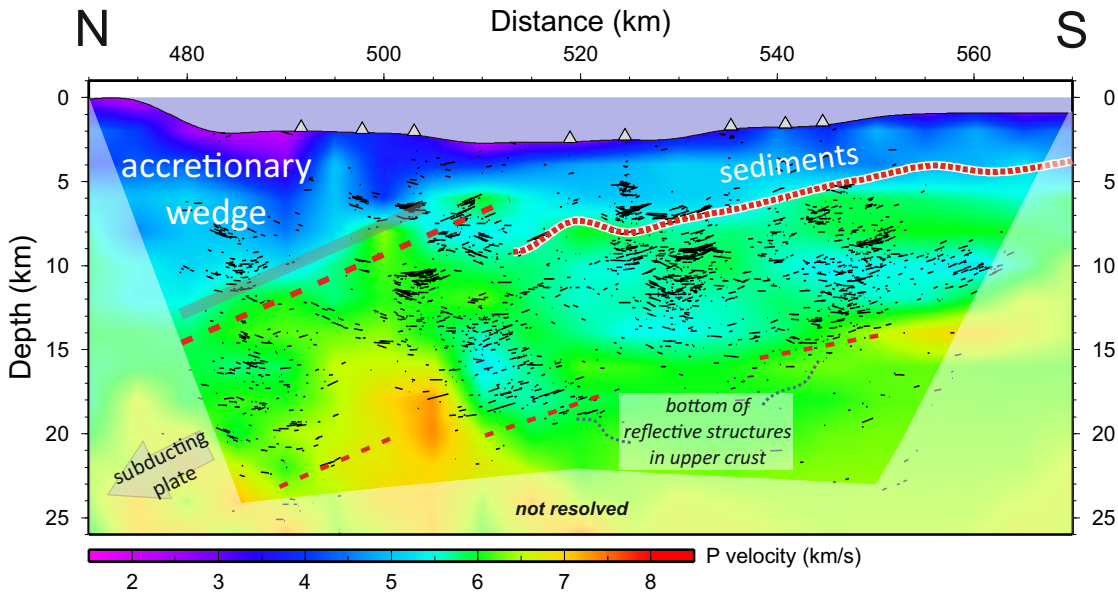


FIGURE 4.21: Result of the pre-stack line-drawing migration for the offshore region south of Cyprus, performed with ocean bottom seismometer nos. 20,21,22,24,25,28,29 and 30 shown by grey triangles. Red-white dashed line shows upper crustal reflection already modelled with secondary phases of the wide-angle seismic data (Fig. 4.8). Upper red dashed line is the suggested upper boundary of the subducting plate (corresponds to red dashed line Fig. in 4.14), grey bar shows the boundary between the accretionary wedge and the crystalline basement. Lower red dashed lines show the bottom of the reflective structures in the upper crust derived by the pre-stack line drawing migration.

Masked area is not resolved by the pre-stack line-drawing migration.

4.5 Integrated Interpretation

The velocity distribution and crustal thickness of the region beneath Turkey constrain a continental type of crust. The crustal thickness of 45 *km* and a low upper mantle P-wave velocity of 7.8 *km/s* is derived from the combined analysis of the wide-angle seismic data and the gravity data. These results are in agreement with previous investigations (Mutlu and Karabulut, 2011; Gans et al., 2009; Vanacore et al., 2013).

The simultaneous thickening of the upper crust, an increasing P-wave velocity in the upper crust, a change in Moho depth from 38 *km* to 45 *km* and the decreasing thickness of the sedimentary cover at 90 – 100 *km* offset implies a lateral change in crustal structure. Combined with the seismicity distribution in this area (from NEIC (USGS), Kandilli Observatory and Earthquake Research Institute and Geological Survey Department Cyprus), which shows high seismically active vertical zones (Fig. 4.22) and geological information (Fig. 1.3), two crustal blocks with different internal properties are defined. The northern crustal unit corresponds to the Central Anatolian Crystalline Complex, overlain by the sedimentary cover of the TuzGözü basin (**TGB** in Fig. 4.22). The inner Tauride suture marks the boundary between the Central Anatolian Crystalline Complex to the north and the Tauride block to the south. The northern part of the Tauride block is overlain by the sediments of the Konya basin (**KB** in Fig. 4.22). From an offset of 185 *km* the Central Taurides mountains define the most southern part of Turkey along the profile.

Due to the lack of seismic rays in the region of the Cilicia basin, the crustal structure is mainly derived by gravity modelling. The gravity data are compatible with 3 *km* thick sediments beneath the Cilicia basin and older (pre-Cilicia basin) sediments beneath northern Cyprus. Beneath the sediments at a depth of 5 – 15 *km*, the southern edge of the upper continental crust is thought to exist, followed by high P-wave velocities (~ 7.2 *km/s*) derived from the wide-angle seismic data. This high velocity block probably is a combination of a high velocity (lower) crust and a serpentized mantle wedge which could potentially have P-wave velocities of about 7.6 *km/s* if the degree of serpentization is about 20% (Hacker et al., 2003; Hacker and Abers, 2004). The precise boundary between the high velocity (lower) crust ($V_p = 7.2$ *km/s*) and the

serpentinized mantle ($V_p = 7.6 \text{ km/s}$) is not resolved. The fluids for the serpentinization of the mantle wedge could have been derived from the subducting plate (see e.g. [Krawczyk et al., 2006](#) and references therein).

The wide-angle seismic data reveal that the ophiolite complex extends from the northern coast of Cyprus to the southern coast of Cyprus (red area in Fig. 4.22) with a maximum thickness of 12 km beneath Cyprus. Based on the tomographic P-wave velocity model the knowledge about the location and geometry of the ophiolite complex beneath Cyprus is substantially improved.

Both parts of the amphibian wide-angle seismic profile, namely the tomographic part and the layered part, show features which indicate a northward subducting plate beneath Cyprus. The tomographic part with the well constrained accretionary wedge provides a first estimation of the dip angle of the subducting plate, which is confirmed by two reflected phases of the southern land shot observed at the stations on Cyprus. The upper and lower parts of the slab geometry (derived from gravity modelling) are also confirmed by the seismicity distribution shown as black (hypocenters from regional networks) and blue (hypocenters from global networks) circles in Fig. 4.22.

The seismicity distribution below 55 km depth (mainly from global catalog, blue circles in Fig. 4.22) shows no well defined Benioff zone. However, the distribution of the earthquake hypocentres indicates a slab which dips at an angle of about 28° which is in good agreement with the slab geometry modelled with the wide-angle seismic and gravity data presented in this study (Fig. 4.22). The uncertainties of these deeper hypocentres are estimated to be 25 km in depth and a few tenths of a degree in the epicentral position ([Sipkin et al., 2000](#)).

The combined analysis of wide-angle seismic and gravity data provides evidence for a flat northward subducting slab with a dip angle of about 13° in the shallower part (above 55 km depth) increasing to about 28° in the deeper part (below 55 km depth), which also has a higher density compared to the upper part (upper part: 2.92 g/cm^3 , lower part: 3.12 g/cm^3).

Based on the tomographic P-wave velocity model, which reveals the velocity structure beneath Cyprus and the ESM, it is possible to define crustal units and boundaries in

these regions with a resolution which was never reached before. The high P-wave velocities beneath the area between Cyprus and the ESM mark the boundary between the continental block of the ESM and a crust with a more oceanic affinity, which is subducted beneath Cyprus (Fig. 4.22).

The amphibian offshore / on-offshore wide-angle seismic data reveal a northward increasing Moho depth, from 28 km south of the ESM to 37 km north of the ESM, and which is variable (32 km - 35 km) beneath the ESM. The topography of the Moho beneath the ESM is a new insight into the crustal structure of the ESM contributed by the wide-angle seismic tomography presented in this study. The area south of the ESM is interpreted as the transition from continental to oceanic crust.

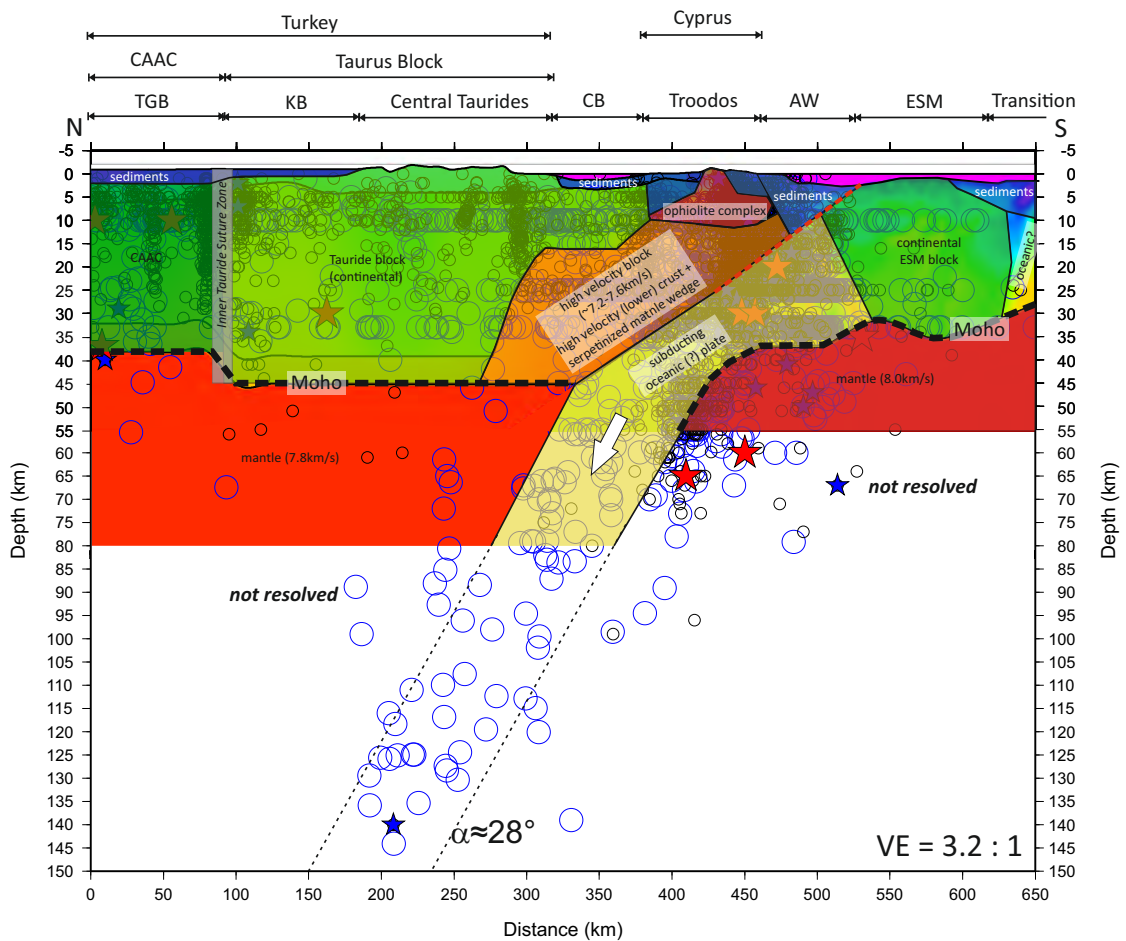


FIGURE 4.22: Final geodynamic interpretation with associated geological units and seismicity distribution (from NEIC (USGS), Kandilli Observatory and Earthquake Research Institute and Geological Survey Department Cyprus). Blue circles show hypocentres from the global PDE catalog. Black circles show seismicity from regional networks (Turkey and Cyprus). Blue stars show earthquakes with magnitudes > 4.5 and red stars show earthquakes with magnitudes > 5.0. KB = Konya basin, TGB = TuzGözü basin, CACC = Central Anatolian Crystalline Complex, CB = Cilicia basin, AW = accretionary wedge, ESM = Eratosthenes Seamount.

The angle of the subduction beneath Cyprus means that the subduction is defined as a flat subduction ($< 30^\circ$). It shows the same slab geometry as the subduction beneath South America and Alaska (Fig. 4.23). Flat subducting slabs are often associated with compressional continental advancing upper plates (Lallemand et al., 2005). The subduction beneath Cyprus would be another example for this hypothesis.

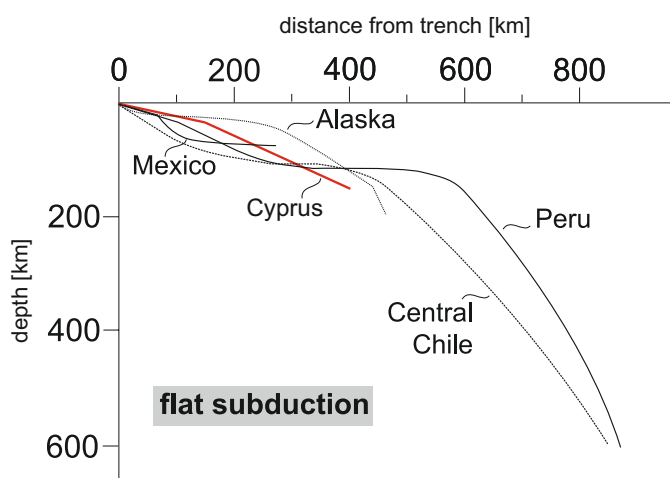


FIGURE 4.23: Comparison of flat subduction settings adapted from Lallemand et al. (2005). Red solid line is flat subducting slab of the crustal model presented in this study.

Comparing the results presented in this study with existing geodynamic models for the ESM - Cyprus - south Turkey region (Schildgen et al., 2014), good correlations were found with the concept of shallow slab break-off after the collision of the Eratosthenes Seamount in the late Pliocene to early Pleistocene, crustal thickening above the subducting African plate, mantle upwelling and rapid uplift of the Central Anatolian Plateau.

The existence of an accretionary wedge is a sign for young deposition of sediments and recent earthquake activity is assigned to a suggested active subduction process. However, in comparison to the Hellenic Arc subduction the Cyprus Arc subduction is much less active in sense of plate motion and seismicity. Thus the state of subduction of the Cyprus Arc is identified to be damped and locked by the collision of the continental block of the Eratosthenes Seamount which is recently entering the subduction zone. This conclusion is in good agreement with the results of Ergün et al. (2005) and Robertson (1998a) which showed that the subduction virtually ceased as the arrival of thicker, low-density crust (the Eratosthenes Seamount) at the northern edge of the African plate results in resistance to further subduction (Ergün et al., 2005).

The most likely explanation for the high velocity block beneath the Troodos ophiolite complex (see Fig. 4.22) is the existence of lower crust and serpentized mantle from a rifted, thinned continental margin. Fig. 4.24 shows the schematic evolution from a continental margin to a subduction setting which explains the existence of the high velocity block beneath Troodos. The basin development south and north of Cyprus and the overthrusting of the Kyrenia range are neglected in this schematic evolution. The shown block model is in agreement with the previous models which conclude that the whole ophiolite complex was obducted and emplaced above the continental margin about 75 million years ago (Blome and Irwin, 1985; Silantyev and Portnyagin, 2005) and that Cyprus has been continuously uplifted since Late Miocene (Harrison et al., 2004).

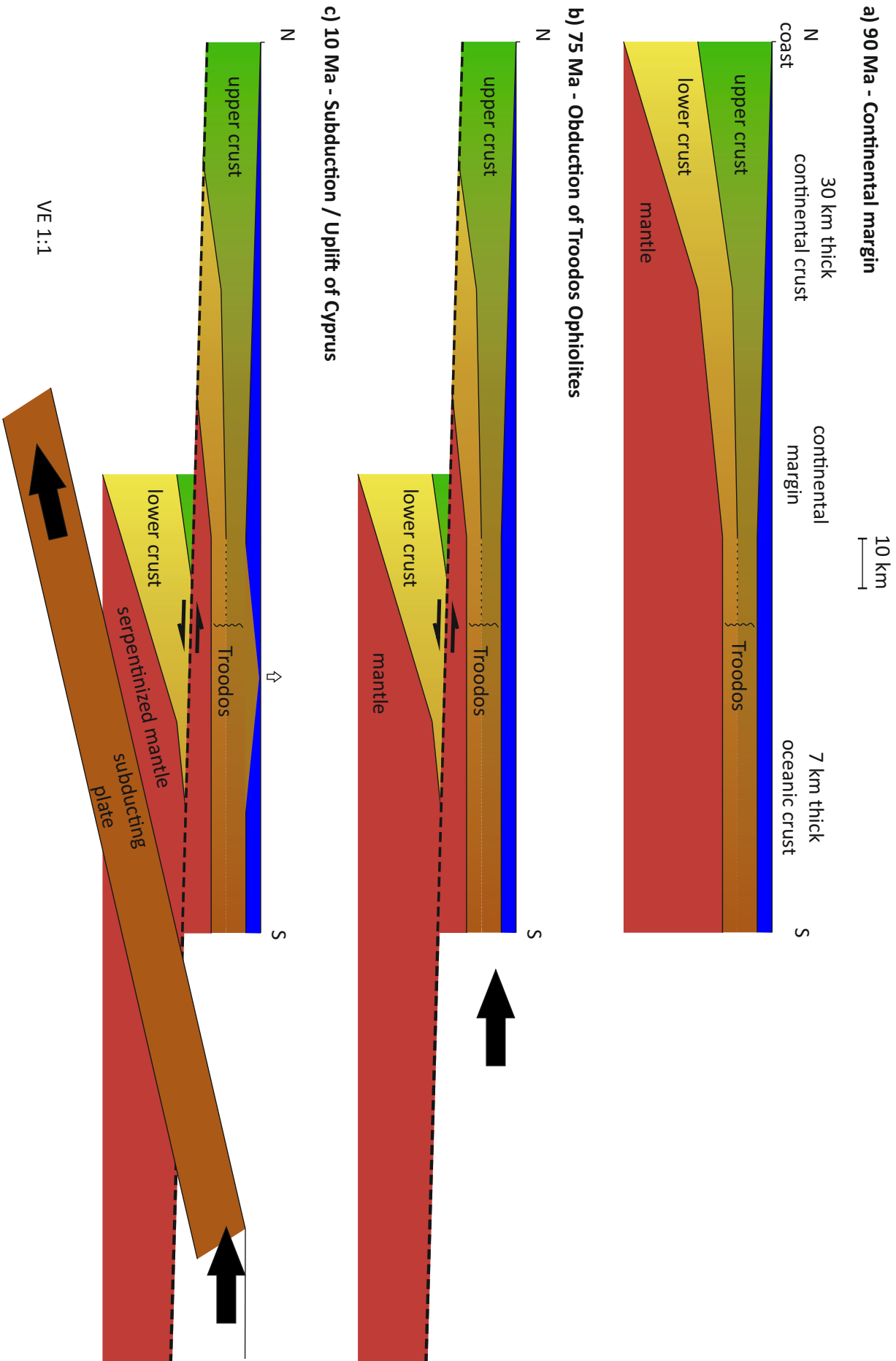


FIGURE 4.24: Schematic block model showing the evolution from a continental margin (a, 90 *Ma*), through the obduction of the Troodos ophiolites (b, 75 *Ma*) to the northward subduction and uplift of Cyprus (c, 10 *Ma*), which explains the existence of lower crust and serpentinized mantle beneath the Troodos ophiolites.

Chapter 5

Conclusions

The velocity structure of an amphibian 650 km long N-S transect crossing the Eratosthenes Seamount, Cyprus and south Turkey was investigated down to the crust-mantle boundary using wide-angle seismic data.

The evaluation of the tomography for the region of the Eratosthenes Seamount and Cyprus reveals lateral variations in Moho depth (28 – 35 km) and P-wave velocities. In general, the P-wave velocities beneath the Eratosthenes Seamount do not exceed 6.5 km/s throughout the whole crust with a thin sedimentary unit on the top. The crust below the Eratosthenes Seamount is identified to be continental with a maximum thickness of 35 km thinning towards the southern end of the profile (28 km thickness), which is attributed to the transition to oceanic crust underlying the Levant basin. In contrast to the crustal structure below the Eratosthenes Seamount, thick sediments (10 – 12 km), interpreted as an accretionary wedge, and higher velocities (6.5 – 7.0 km/s) in the lower crust are observed between the Eratosthenes Seamount and Cyprus. These features are interpreted as the transition zone to a thinner, high velocity crust (15 – 20 km and $V_p = 6.8$ km/s) which is subducted beneath Cyprus.

The analysis of the layered P-wave velocity model for the Anatolian plateau reveals strong lateral variations in crustal and sedimentary thickness. The crust beneath the TuzGözü basin is 38 km thick and thickens southwards to 45 km beneath the central Taurides. The thickened crust beneath the whole Anatolian plateau is attributed to the northward push of the African plate against the Anatolian micro-plate. The lateral change of the crustal structure is assigned to the inner Tauride suture which separates

the Central Anatolian Crystalline Complex in the north and the Taurus block in the south. The upper mantle velocity beneath the Turkish part of the profile is identified to be 7.8 km/s which is attributed to the Neogene-Quaternary volcanism of the Central Anatolia Volcanic Zone. A high P-wave velocity block ($V_p = 7.2 - 7.6 \text{ km/s}$) beneath the region of the Cilicia Basin (at a depth of $15 - 35 \text{ km}$) and Cyprus is derived from the wide-angle seismic and is identified to be the combination of high velocity (lower) crust and serpentinized mantle from a rifted, thinned continental margin.

The accurate determination of the Moho depth and mantle velocity with wide-angle seismic investigations such as presented in this study, provides an important and significant insight into the crustal structure of southern Turkey, Cyprus and the Eratosthenes Seamount. A subsequent gravity modelling along the profile extends and confirms the revealed information about the crustal structure of the Anatolian plateau and Cyprus. The combined analysis of seismic and gravity data provides evidence for a northward dipping slab beneath Cyprus and the Cilicia basin with increasing dip ($13^\circ - 28^\circ$) and increasing density ($2.92 \text{ g/cm}^3 - 3.12 \text{ g/cm}^3$). Based on the average P-wave velocity (6.8 km/s) and crustal thickness ($15 - 20 \text{ km}$) the subducted slab has a more oceanic affinity. The deeper slab geometry (below 55 km depth) is constrained by gravity data and seismological data and is identified to dip with an angle of $\sim 28^\circ$, which is defined as a flat slab subduction.

The results of the crustal structure presented in this study show good agreement with independent previous investigations and existing geodynamic models for the eastern Mediterranean, Cyprus and the Anatolian plateau. For the first time the detailed properties such as P-wave velocity and density as well as the geometry of the crustal structure beneath the Eratosthenes Seamount, Cyprus and the Anatolian plateau were revealed. The existence of a northward subducting plate beneath Cyprus was confirmed and new insight into the geometry is provided. The presented integrated interpretation of seismic data, gravity data and seismological data give a first estimation of the deeper part of the subducting slab. To extend and improve the constraints on the deeper part of the subducted plate further investigations are necessary. To investigate the region beneath Cyprus and the Cilicia basin with higher resolution and to verify the results presented in this study, it would be necessary to deploy seismic stations in the northern part of Cyprus and again in southern Turkey, in combination with OBS stations and airgun

shots in the region between Turkey and Cyprus as the receivers and sources for another wide-angle seismic study.

Appendix A

Station and land shot list

Station no.	station name	type of station	Lat [° N]	Lon [° E]	Elevation [m]	Offset [km]	sample rate [ms /sps]	picked channel [Z / Hydro]	picked Offset to N [km]	to S [km]	comments
1	GSC A	OBS	33.0138	32.5733	-1420.0	640.8	4 / 250	Z	NE ¹ (180)	SE ²	
2	GSC C	OBS	33.0541	32.5874	-1440.0	635.2	4 / 250	Z	175	5	
3	GSC E	OBS	33.0935	32.5973	-1410.0	627.8	4 / 250	Z	170	10	
4	GSC F	OBS	33.1593	32.6107	-1430.0	622.9	4 / 250	Z	160	18	
5	GSC H	OBS	33.2251	32.6291	-2050.0	618.4	4 / 250	Z	25	26	
6	GSC J	OBS	33.2624	32.6376	-1990.0	612.2	4 / 250	Z	45	30	
7	Binky	OBH	33.2980	32.6461	-1860.0	606.9	20 / 50	Hydro	65	30	
8	Jever	OBS	33.3411	32.6560	-1770.0	601.1	5 / 200	Hydro	60	35	
9	Polar	OBS	33.3912	32.6685	-1630.0	596.4	5 / 200	Z	100	30	
10	Ganter	OBS	33.4394	32.6880	-1420.0	591.1	5 / 200	Hydro	50	40	
11	Keo	OBS	33.4828	32.6906	-1360.0	585.5	5 / 200	Z	55	50	
12	Krieg	OBH	33.5341	32.7041	-1190.0	581.6	20 / 50	Hydro	40	50	
13	Astra	OBS	33.5777	32.7161	-830.0	574.8	5 / 200	Hydro	80	40	
14	GSC K	OBS	33.6130	32.7237	-840.0	569.2	4 / 250	Z	115	65	
15		?						-	-	-	no data
16	GSC N	OBS	33.7102	32.7457	-930.0	565.4	4 / 250	Hydro	30	80	
17	GSC P	OBS	33.7615	32.7593	-910.0	559.2	4 / 250	Z	65	85	
18	DAL A	OBS	33.8020	32.7687	-950.0	553.9	4 / 250	Hydro	80	60	
19	DAL B	OBS	33.8485	32.7802	-1120.0	549.3	4 / 250	Hydro	45	65	
20	DAL C	OBS	33.9037	32.7935	-1650.0	543.5	4 / 250	Hydro	40	100	
21	OBS Becks	OBS	33.9372	32.8014	-1760.0	532.5	5 / 200	Hydro	40	60	
22	OBS Rathaus	OBS	33.9860	32.8155	-1890.0	528.6	5 / 200	Hydro	45	40	
23	OBH Pest	OBH	34.0471	32.8276	-2510.0	523.6	20 / 50	Hydro	40	35	
24	OBS Karl-squell	OBS	34.0813	32.8386	-2510.0	517.8	5 / 200	Hydro	30	40	
25	OBS Duff	OBS	34.1312	32.8481	-2640.0	513.0	5 / 200	Z	40	125	
26	OBH Tod	OBH	34.1776	32.8613	-2660.0	507.4	5 / 200	Hydro			
27	OBH Hunger	OBH	34.2194	32.8689	-2690.0	501.7	20 / 50	Hydro	25	50	

...

¹ Northern End of the profile
² Southern End of the profile

TABLE A.1: Stationlist (Continuation)

Station no.	station name	type of station	Lat [°N]	Lon [°E]	Elevation [m]	Offset [km]	sample rate [ms /sps]	picked channel [Z / Hydro]	picked Offset to N [km]	to S [km]	comments
28	OBS Espes- cial	OBS	34.2709	32.8805	-2230.0	496.9	5 / 200	Hydro	25	40	
29	DAL D	OBS	34.3179	32.8924	-2090.0	492.9	4 / 250	Z	30	150	
30	DAL E	OBS	34.3723	32.9060	-1990.0	488.7	4 / 250	Z	25	150	
31	DAL F	OBS	34.4121	32.9138	-2050.0	481.2	4 / 250	Hydro	20	20	
32	DAL I	OBS	34.4562	32.9240	-1970.0	473.8	4 / 250	Z	20	160	
33	DAL K	OBS	34.5317	32.8746	-180.0	469.3	4 / 250	Z	10	170	
34	DAL N	OBS	34.5877	32.8390	-120.0	465.3	4 / 250	Z	5	175	
C201		EDL + 3ch (e3229)	34.6953	32.9035	106.2	456.0	10 / 100	Z	NE	33	
C202		CUBE + 1ch (c0054)	34.7015	32.8963	170.0	455.4	10 / 100	Z	NE	46	
C203		EDL + 3ch (e3221)	34.7085	32.8919	241.6	454.6	10 / 100	Z	NE	36	
C204		CUBE + 1ch (c0057)	34.7185	32.8923	297.0	453.6	10 / 100	Z	NE	54	with gaps
C205		EDL + 3ch (e3181)	34.7241	32.8900	334.4	453.0	10 / 100	Z	NE	SE	with gaps
C206		CUBE + 1ch (c0103)	34.7341	32.8865	400.0	451.9	10 / 100	Z	NE	SE	with gaps
C207		EDL + 3ch (e3222)	34.7426	32.8791	465.9	451.0	10 / 100	Z	NE	SE	
C208		CUBE + 1ch (c0097)	34.7505	32.8689	531.0	450.3	10 / 100	Z	NE	SE	
C209		EDL + 3ch (e3170)	34.7565	32.8563	564.7	449.7	10 / 100	Z	NE	SE	gap between 52 km - 105 km
C210		CUBE + 1ch (c0045)	34.7652	32.8413	559.0	448.9	10 / 100	Z	NE	SE	
C211		EDL + 3ch (e3220)	34.7742	32.8317	539.6	448.0	10 / 100	Z	NE	SE	gap between 45 km - 106 km
C212		CUBE + 1ch (c0094)	34.7816	32.8281	534.0	447.2	10 / 100	Z	NE	SE	
C213		EDL + 3ch (e3207)	34.7900	32.8281	569.7	446.3	10 / 100	Z	NE	SE	gap between 51 km - 111 km
C214		CUBE + 1ch (c0096)	34.7983	32.8248	626.0	445.4	10 / 100	Z	NE	SE	
C215		EDL + 3ch (e3212)	34.8065	32.8223	701.8	444.5	10 / 100	Z	NE	SE	
C216		CUBE + 1ch (c0014)	34.8138	32.8245	759.0	443.7	10 / 100	Z	NE	SE	
C217		EDL + 3ch (e3228)	34.8239	32.8373	799.7	442.4	10 / 100	Z	NE	SE	
C218		CUBE + 1ch (c0030)	34.8303	32.8500	755.0	441.6	10 / 100	Z	NE	SE	
C219		EDL + 3ch (e3217)	34.8401	32.8595	771.6	440.4	10 / 100	Z	NE	SE	

...

TABLE A.1: Stationlist (Continuation)

Station no.	station name	type of station	Lat [°N]	Lon [°E]	Elevation [m]	Offset [km]	sample rate [ms /sps]	picked channel [Z / Hy-dro]	picked Offset to N [km]	to S [km]	comments
C220		CUBE + 1ch (c0092)	34.8470	32.8686	685.0	439.6	10 / 100	Z	NE	SE	
C221		EDL + 3ch (e3176)	34.8559	32.8713	747.2	438.6	10 / 100	-	-	-	no data
C222		CUBE + 1ch (c0093)	34.8635	32.9130	606.0	437.4	10 / 100	-	-	-	noisy
C223		EDL + 3ch (e3215)	34.8717	32.9182	664.4	436.4	10 / 100	Z	NE	SE	
C224		CUBE + 1ch (c0085)	34.8802	32.9252	709.0	435.4	10 / 100	Z	NE	SE	with gaps
C225		EDL + 3ch (e3173)	34.8865	32.9320	744.8	434.7	10 / 100	Z	NE	SE	
C226		CUBE + 1ch (c0080)	34.8977	32.9363	850.0	433.4	10 / 100	Z	NE	54	
C227		EDL + 3ch (e3209)	34.9027	32.9423	869.0	432.8	10 / 100	Z	NE	SE	
C228		CUBE + 1ch (c0102)	34.9133	32.9412	928.0	431.6	10 / 100	Z	NE	SE	
C229		EDL + 3ch (e3169)	34.9205	32.9346	988.4	430.9	10 / 100	Z	NE	SE	
C230		CUBE + 1ch (c0090)	34.9290	32.9353	1057.0	430.0	10 / 100	Z	NE	SE	with 2 big gaps
C231		EDL + 3ch (e3213)	34.9370	32.9320	1139.9	429.1	10 / 100	Z	NE	58	
C232		CUBE + 1ch (c0084)	34.9451	32.9404	1183.0	428.1	10 / 100	Z	40	56	bad S/N ratio
C233		EDL + 3ch (e3171)	34.9531	32.9619	1341.7	427.1	10 / 100	Z	NE	SE	
C234		CUBE + 1ch (c0086)	34.9610	32.9620	1224.0	426.2	10 / 100	Z	NE	SE	
C235		EDL + 3ch (e3216)	34.9698	32.9630	1137.0	425.2	10 / 100	Z	NE	SE	
C236		CUBE + 1ch (c0101)	34.9782	32.9704	918.0	424.2	10 / 100	Z	NE	186	bad S/N ratio
C237		EDL + 3ch (e3203)	34.9864	32.9800	737.3	423.2	10 / 100	Z	NE	SE	bad S/N ratio
C238		CUBE + 1ch (c0098)	34.9964	32.9899	660.0	422.0	10 / 100	Z	NE	61	bad S/N ratio
C239		EDL + 3ch (e3218)	35.0027	32.9978	591.3	421.3	10 / 100	Z	NE	SE	
C240		CUBE + 1ch (c0081)	35.0103	33.0037	500.0	420.4	10 / 100	Z	NE	SE	
C241		EDL + 3ch (e3168)	35.0149	33.0056	526.0	419.8	10 / 100	Z	-	-	noisy
C242		CUBE + 1ch (c0099)	35.0254	33.0105	519.0	418.6	10 / 100	Z	NE	SE	with gaps
C243		EDL + 3ch (e3219)	35.0359	33.0188	456.0	417.4	10 / 100	Z	NE	SE	with big gap
C244		CUBE + 1ch (c0083)	35.0425	33.0230	390.0	416.6	10 / 100	Z	NE	SE	with gaps
C245		EDL + 3ch (e3202)	35.0521	33.0269	342.9	415.5	10 / 100	Z	NE	SE	with big gap
C246		CUBE + 1ch (c0088)	35.0594	33.0272	314.0	414.7	10 / 100	Z	NE	SE	with big gap
C247		EDL + 3ch (e3210)	35.0681	33.0190	298.2	413.8	10 / 100	Z	NE	SE	with big gap
C248		CUBE + 1ch (c0089)	35.0747	33.0166	307.0	413.1	10 / 100	Z	NE	SE	with big gap
C249		EDL + 3ch (e3205)	35.0839	33.0154	323.6	412.1	10 / 100	Z	NE	SE	with big gap

...

TABLE A.1: Stationlist (Continuation)

Station no.	station name	type of station	Lat [°N]	Lon [°E]	Elevation [m]	Offset [km]	sample rate [ms /sps]	picked channel [Z / Hy-dro]	picked Offset to N [km]	to S [km]	comments
C250	C250	CUBE + 1ch (c0091)	35.0908	33.0154	252.0	411.4	10 / 100	Z	NE	SE	with big gap
T1	T1	EDL + 3ch (e3152)	36.0245	32.8030	15.5	310.2	10 / 100	Z			
T2	T2	CUBE + 1ch (c0077)	36.0386	32.8053	8.0	308.6	10 / 100	Z			
T3	T3	t3030	36.0504	32.8182	5.0	-	-	-			
T4	T4	EDL + 3ch (e3160)	36.0643	32.8277	3.3	305.6	10 / 100	Z			
T5	T5	CUBE + 1ch (c0079)	36.0800	32.8501	7.0	303.7	10 / 100	Z			
T6	T6	t3037	36.0936	32.8462	44.0	-	-	-			
T7	T7	EDL + 3ch (e3155)	36.1072	32.8527	11.7	300.6	10 / 100	Z			
T8	T8	CUBE + 1ch (c0063)	36.1215	32.8492	31.0	299.1	10 / 100	Z			
T9	T9	t3027	36.1354	32.8634	77.0	-	-	-			
T10	T10	EDL + 3ch (e3163)	36.1492	32.8650	66.4	295.9	10 / 100	Z			
T11	T11	CUBE + 1ch (c0066)	36.1643	32.8647	125.0	294.2	10 / 100	Z			
T12	T12	t3041	36.1697	32.8825	134.0	-	-	-			
T13	T13	CUBE + 1ch (c0065)	36.1876	32.9160	180.0	291.2	10 / 100	Z			
T14	T14	EDL + 3ch (e3156)	36.1779	32.9014	119.0	292.4	10 / 100	Z			
T15	T15	t3035	36.1916	32.9260	335.0	-	-	-			
T16	T16	EDL + 3ch (e3158)	36.2054	32.9185	393.2	289.2	10 / 100	Z			
T17	T17	CUBE + 1ch (c0062)	36.2188	32.9020	958.0	287.9	10 / 100	Z			
T18	T18	t3031	36.2333	32.9111	1343.0	-	-	-			
T19	T19	EDL + 3ch (e3153)	36.2476	32.9110	1573.8	284.6	10 / 100	Z			
T20	T20	CUBE + 1ch (c0067)	36.2606	32.9138	1661.0	283.2	10 / 100	Z			
T21	T21	t3029	36.2757	32.9163	1687.0	-	-	-			
T22	T22	EDL + 3ch (e3161)	36.2897	32.9098	1540.4	280.0	10 / 100	Z			
T23	T23	CUBE + 1ch (c0072)	36.3031	32.9241	1412.0	278.4	10 / 100	Z			
T24	T24	t3032	36.3136	32.9359	1410.0	-	-	-			
T25	T25	EDL + 3ch (e3157)	36.3311	32.9528	1330.9	275.0	10 / 100	Z			
T26	T26	CUBE + 1ch (c0078)	36.3450	32.9544	1319.0	273.5	10 / 100	Z			
T27	T27	t3040	36.3598	32.9541	1329.0	-	-	-			
T28	T28	EDL + 3ch (e3167)	36.3732	32.9425	1369.2	270.5	10 / 100	Z			
T29	T29	CUBE + 1ch (c0069)	36.3875	32.9432	1363.0	268.9	10 / 100	Z			

...

TABLE A.1: Stationlist (*Continuation*)

Station no.	station name	type of station	Lat [°N]	Lon [°E]	Elevation [m]	Offset [km]	sample rate [ms /sps]	picked channel [Z / Hy-dro]	picked Offset to N [km]	to S [km]	comments
T30	T30	t3038	36.3996	32.9359	1348.0	-	-	-			
T31	T31	EDL + 3ch (e3150)	36.4148	32.9275	1387.7	266.0	10 / 100	Z			
T32	T32	CUBE + 1ch (c0074)	36.4262	32.8889	1514.0	265.1	10 / 100	Z			
T33	T33	t3033	36.4411	32.8572	1507.0	-	-	-			
T34	T34	EDL + 3ch (e3159)	36.4560	32.8416	1479.5	262.2	10 / 100	Z			
T35	T35	CUBE + 1ch (c0071)	36.4701	32.8440	1460.0	260.7	10 / 100	Z			
T36	T36	t3034	36.4844	32.8459	1433.0	-	-	-			
T37	T37	EDL + 3ch (e3154)	36.4997	32.8567	1206.2	257.3	10 / 100	Z			
T38	T38	CUBE + 1ch (c0073)	36.5123	32.8585	1119.0	255.9	10 / 100	Z			
T39	T39	t3039	36.5268	32.9051	940.0	-	-	-			
T40	T40	EDL + 3ch (e3162)	36.5403	32.8541	1068.3	252.8	10 / 100	Z			
T41	T41	CUBE + 1ch (c0075)	36.5541	32.8432	1087.0	251.4	10 / 100	Z			
T42	T42	t3028	36.5684	32.9556	677.0	-	-	-			
T43	T43	EDL + 3ch (e3151)	36.5827	32.9358	897.5	247.4	10 / 100	Z			
T44	T44	CUBE + 1ch (c0076)	36.5959	32.9259	1028.0	246.1	10 / 100	Z			
T45	T45	t3036	36.6095	32.9219	1182.0	-	-	-			
T46	T46	EDL + 3ch (e3164)	36.6219	32.9209	1289.9	243.2	10 / 100	Z			
T47	T47	CUBE + 1ch (c0070)	36.6374	32.9027	1317.0	241.7	10 / 100	Z			
T48	T48	t1168	36.6509	32.9323	1512.0	-	-	-			
T49	T49	EDL + 3ch (e3110)	36.6654	32.9321	1573.4	238.3	10 / 100	Z			
T50	T50	EDL + 3ch (e3129)	36.6797	32.9388	1710.4	236.7	10 / 100	Z			
T51	T51	t1173	36.6939	32.9474	1678.0	-	-	-			
T52	T52	EDL + 3ch (e3227)	36.7079	32.9461	1517.2	233.5	10 / 100	Z			
T53	T53	CUBE + 1ch (c0049)	36.7216	32.9300	1535.0	232.1	10 / 100	Z			
T54	T54	t1166	36.7346	32.9140	1614.0	-	-	-			
T55	T55	EDL + 3ch (e3225)	36.7496	32.9073	1610.7	229.2	10 / 100	Z			
T56	T56	EDL + 3ch (e3083)	36.7631	32.9040	1591.9	227.8	10 / 100	Z			
T57	T57	t0973	36.7775	32.8890	1642.0	-	-	-			
T58	T58	EDL + 3ch (e3112)	36.7906	32.9124	1799.3	224.7	10 / 100	Z			
T59	T59	CUBE + 1ch (c0059)	36.8046	32.9174	1798.0	223.1	10 / 100	Z			

...

TABLE A.1: Stationlist (Continuation)

Station no.	station name	type of station	Lat [°N]	Lon [°E]	Elevation [m]	Offset [km]	sample rate [ms / sps]	picked channel [Z / Hy-dro]	picked Offset to N [km]	to S [km]	comments
T60	T60	t1163	36.8185	32.9272	1915.0	-	-	-			
T61	T61	EDL + 3ch (e3084)	36.8329	32.9331	1875.1	219.8	10 / 100	Z			
T62	T62	EDL + 3ch (e3127)	36.8472	32.9178	1664.0	218.4	10 / 100	Z			
T63	T63	t1170	36.8610	32.9490	1471.0	-	-	-			
T64	T64	EDL + 3ch (e3068)	36.8750	33.0121	1348.4	214.5	10 / 100	Z			
T65	T65	CUBE + 1ch (c0053)	36.8888	33.0074	1152.0	213.0	10 / 100	Z			
T66	T66	t3070	36.9032	33.0207	1126.0	-	-	-			
T67	T67	EDL + 3ch (e3137)	36.9165	33.0536	852.7	209.5	10 / 100	Z			
T68	T68	CUBE + 1ch (c0008)	36.9306	33.0480	769.0	208.0	10 / 100	Z			
T69	T69	t1167	36.9454	33.0341	450.0	-	-	-			
T70	T70	EDL + 3ch (e3134)	36.9583	33.0290	472.9	205.1	10 / 100	Z			
T71	T71	CUBE + 1ch (c0006)	36.9698	33.0277	755.0	203.9	10 / 100	Z			
T72	T72	t1176	36.9860	33.0322	1152.0	-	-	-			
T73	T73	EDL + 3ch (e3144)	37.0003	33.0343	1312.1	200.5	10 / 100	Z			
T74	T74	EDL + 3ch (e3117)	37.0139	33.0541	1368.2	198.8	10 / 100	Z			
T75	T75	t1174	37.0287	33.0622	1331.0	-	-	-			
T76	T76	EDL + 3ch (e3145)	37.0427	33.0805	1344.7	195.4	10 / 100	Z			
T77	T77	CUBE + 1ch (c0007)	37.0562	33.0823	1348.0	193.9	10 / 100	Z			
T78	T78	t1171	37.0699	33.0865	1356.0	-	-	-			
T79	T79	EDL + 3ch (e3071)	37.0844	33.0940	1268.8	190.7	10 / 100	Z			
T80	T80	CUBE + 1ch (c0011)	37.0980	33.1115	1162.0	189.0	10 / 100	Z			
T81	T81	t0937	37.1091	33.1120	1078.0	-	-	-			
T82	T82	EDL + 3ch (e3116)	37.1257	33.1305	1082.3	185.8	10 / 100	Z			
T83	T83	CUBE + 1ch (c0012)	37.1394	33.1449	1073.0	184.1	10 / 100	Z			
T84	T84	t3044	37.1535	33.1483	1062.0	-	-	-			
T85	T85	EDL + 3ch (e3091)	37.1676	33.1555	1038.6	180.9	10 / 100	Z			
T86	T86	EDL + 3ch (e3148)	37.1835	33.1577	1031.2	179.1	10 / 100	Z			
T87	T87	t0968	37.1972	33.1745	1024.0	-	-	-			
T88	T88	EDL + 3ch (e3118)	37.2060	33.1864	1017.5	176.4	10 / 100	Z			
T89	T89	CUBE + 1ch (c0027)	37.2234	33.1813	1016.0	174.5	10 / 100	Z			

...

TABLE A.1: Stationlist (*Continuation*)

Station no.	station name	type of station	Lat [°N]	Lon [°E]	Elevation [m]	Offset [km]	sample rate [ms /sps]	picked channel [Z / Hy-dro]	picked Offset to N [km]	to S [km]	comments
T90		t1164	37.2371	33.1850	1012.0	-	-	-			
T91		EDL + 3ch (e3079)	37.2510	33.1945	1009.1	171.4	10 / 100	Z			
T92		CUBE + 1ch (c0022)	37.2658	33.1931	1002.0	169.7	10 / 100	Z			
T93		t0954	37.2792	33.1912	1010.0	-	-	-			
T94		EDL + 3ch (e3113)	37.2926	33.1899	1004.6	166.8	10 / 100	Z			
T95		CUBE + 1ch (c0019)	37.3069	33.1872	1006.0	165.3	10 / 100	Z			
T96		t3069	37.3213	33.1870	1011.0	-	-	-			
T97		EDL + 3ch (e3065)	37.3351	33.2044	1006.7	162.0	10 / 100	Z			
T98		EDL + 3ch (e3128)	37.3490	33.2205	1007.6	160.3	10 / 100	Z			
T99		t3057	37.3640	33.2299	1010.0	-	-	-			
T100		EDL + 3ch (e3149)	37.3767	33.2387	1005.1	157.1	10 / 100	Z			
T101		CUBE + 1ch (c0032)	37.3905	33.2469	1010.0	155.5	10 / 100	Z			
T102		t4231	37.4047	33.2547	1016.0	-	-	-			
T103		EDL + 3ch (e3101)	37.4184	33.2628	1007.1	152.3	10 / 100	Z			
T104		CUBE + 1ch (c0034)	37.4324	33.2702	1003.0	150.7	10 / 100	Z			
T105		t3025	37.4466	33.2777	1018.0	-	-	-			
T106		EDL + 3ch (e3135)	37.4603	33.2855	1007.9	147.4	10 / 100	Z			
T107		CUBE + 1ch (c0031)	37.4741	33.2940	1011.0	145.8	10 / 100	Z			
T108		t3063	37.4876	33.3039	1000.0	-	-	-			
T109		EDL + 3ch (e3099)	37.5023	33.3087	1003.0	142.6	10 / 100	Z			
T110		EDL + 3ch (e3138)	37.5162	33.3150	1005.6	141.0	10 / 100	Z			
T111		t3058	37.5308	33.3250	1011.0	-	-	-			
T112		EDL + 3ch (e3088)	37.5442	33.3277	1010.3	137.8	10 / 100	Z			
T113		CUBE + 1ch (c0036)	37.5580	33.3373	1015.0	136.2	10 / 100	Z			
T114		t3072	37.5705	33.3504	1006.0	-	-	-			
T115		EDL + 3ch (e3096)	37.5861	33.3687	999.5	132.8	10 / 100	Z			
T116		CUBE + 1ch (c0038)	37.5997	33.3891	1004.0	131.1	10 / 100	Z			
T117		t3059	37.6165	33.4065	1012.0	-	-	-			
T118		EDL + 3ch (e3143)	37.6273	33.4215	1005.6	127.8	10 / 100	Z			
T119		CUBE + 1ch (c0026)	37.6411	33.4353	1002.0	126.1	10 / 100	Z			
											...

TABLE A.1: Stationlist (Continuation)

Station no.	station name	type of station	Lat [°N]	Lon [°E]	Elevation [m]	Offset [km]	sample rate [ms /sps]	picked channel [Z / Hy-dro]	picked Offset to N [km]	to S [km]	comments
T120	T120	t3065	37.6549	33.4469	1033.0	-	-	-	-	-	
T121	T121	EDL + 3ch (e3106)	37.6690	33.4537	1022.0	122.9	10 / 100	Z			
T122	T122	EDL + 3ch (e3119)	37.6834	33.4595	1021.8	121.2	10 / 100	Z			
T123	T123	t3060	37.6978	33.4654	1021.0	-	-	-			
T124	T124	EDL + 3ch (e3147)	37.7115	33.4638	1028.2	118.1	10 / 100	Z			
T125	T125	CUBE + 1ch (c0041)	37.7247	33.5510	998.0	115.8	10 / 100	Z			
T126	T126	t3062	37.7380	33.5532	987.0	-	-	-			
T127	T127	EDL + 3ch (e3104)	37.7521	33.5583	985.6	112.8	10 / 100	Z			
T128	T128	CUBE + 1ch (c0039)	37.7664	33.5625	987.0	111.1	10 / 100	Z			
T129	T129	t3066	37.7799	33.5668	992.0	-	-	-			
T130	T130	EDL + 3ch (e3130)	37.7938	33.5749	991.4	108.0	10 / 100	Z			
T131	T131	CUBE + 1ch (c0040)	37.8076	33.5844	990.0	106.4	10 / 100	Z			
T132	T132	t4230	37.8209	33.5934	993.0	-	-	-			
T133	T133	EDL + 3ch (e3074)	37.8355	33.5971	990.5	103.2	10 / 100	Z			
T134	T134	EDL + 3ch (e3132)	37.8496	33.6003	991.2	101.6	10 / 100	Z			
T135	T135	t4176	37.8638	33.6065	991.0	-	-	-			
T136	T136	EDL + 3ch (e3108)	37.8782	33.6123	994.4	98.3	10 / 100	Z			
T137	T137	CUBE + 1ch (c0001)	37.8910	33.6105	1022.0	96.9	10 / 100	Z			
T138	T138	t3046	37.9063	33.6242	1008.0	-	-	-			
T139	T139	EDL + 3ch (e3109)	37.9185	33.6283	1006.9	93.8	10 / 100	Z			
T140	T140	CUBE + 1ch (c0004)	37.9339	33.6057	1049.0	92.3	10 / 100	Z			
T141	T141	t3074	37.9472	33.5903	1072.0	-	-	-			
T142	T142	EDL + 3ch (e3140)	37.9613	33.5750	1073.9	89.5	10 / 100	Z			
T143	T143	CUBE + 1ch (c0003)	37.9780	33.5579	1060.0	87.8	10 / 100	Z			
T144	T144	t3049	37.9891	33.5500	1037.0	-	-	-			
T145	T145	EDL + 3ch (e3073)	38.0077	33.5418	1026.1	84.7	10 / 100	Z			
T146	T146	EDL + 3ch (e3136)	38.0211	33.5365	1022.3	83.3	10 / 100	Z			
T147	T147	t3056	38.0305	33.5299	1029.0	-	-	-			
T148	T148	EDL + 3ch (e3226)	38.0458	33.5228	1021.3	80.7	10 / 100	Z			
T149	T149	CUBE + 1ch (c0056)	38.0592	33.5018	1015.0	79.4	10 / 100	Z			

...

TABLE A.1: Stationlist (Continuation)

Station no.	station name	type of station	Lat [°N]	Lon [°E]	Elevation [m]	Offset [km]	sample rate [ms /sps]	picked channel [Z / Hy-dro]	picked Offset to N [km]	to S [km]	comments
T150	T150	t3061	38.0731	33.5100	1031.0	-	-	-	-	-	
T151	T151	EDL + 3ch (e3094)	38.0868	33.5109	1028.7	76.3	10 / 100	Z			
T152	T152	CUBE + 1ch (c0028)	38.1002	33.5091	1019.0	74.8	10 / 100	Z			
T153	T153	t3050	38.1151	33.5110	1004.0	-	-	-			
T154	T154	EDL + 3ch (e3120)	38.1289	33.5089	987.2	71.6	10 / 100	Z			
T155	T155	CUBE + 1ch (c0018)	38.1429	33.5029	982.0	70.1	10 / 100	Z			
T156	T156	t3045	38.1588	33.5019	980.0	-	-	-			
T157	T157	EDL + 3ch (e3100)	38.1710	33.4976	977.6	67.1	10 / 100	Z			
T158	T158	EDL + 3ch (e3105)	38.1875	33.4889	993.5	65.3	10 / 100	Z			
T159	T159	t3042	38.1984	33.4867	1003.0	-	-	-			
T160	T160	EDL + 3ch (e3067)	38.2124	33.4833	970.1	62.7	10 / 100	Z			
T161	T161	CUBE + 1ch (c0010)	38.2265	33.4602	964.0	61.3	10 / 100	Z			
T162	T162	t3048	38.2411	33.4547	967.0	-	-	-			
T163	T163	EDL + 3ch (e3072)	38.2539	33.4489	972.4	58.4	10 / 100	Z			
T164	T164	CUBE + 1ch (c0015)	38.2690	33.4391	965.0	56.8	10 / 100	Z			
T165	T165	t3054	38.2827	33.4374	948.0	-	-	-			
T166	T166	EDL + 3ch (e3131)	38.2971	33.4330	951.9	53.8	10 / 100	Z			
T167	T167	CUBE + 1ch (c0017)	38.3103	33.4199	936.0	52.4	10 / 100	Z			
T168	T168	t1134	38.3245	33.3622	956.0	-	-	-			
T169	T169	EDL + 3ch (e3111)	38.3381	33.3503	950.7	50.0	10 / 100	Z			
T170	T170	EDL + 3ch (e3141)	38.3532	33.3531	951.2	48.3	10 / 100	Z			
T171	T171	t3055	38.3668	33.3584	951.0	-	-	-			
T172	T172	EDL + 3ch (e3133)	38.3809	33.3554	945.3	45.2	10 / 100	Z			
T173	T173	CUBE + 1ch (c0002)	38.3953	33.3124	949.0	44.0	10 / 100	Z			
T174	T174	t3053	38.4100	33.2999	945.0	-	-	-			
T175	T175	EDL + 3ch (e3066)	38.4214	33.2883	942.6	41.3	10 / 100	Z			
T176	T176	CUBE + 1ch (c0005)	38.4368	33.2682	938.0	39.8	10 / 100	Z			
T177	T177	t3051	38.4534	33.2645	942.0	-	-	-			
T178	T178	EDL + 3ch (e3115)	38.4676	33.2483	937.8	36.6	10 / 100	Z			
T179	T179	CUBE + 1ch (c0013)	38.4588	33.2231	941.0	37.8	10 / 100	Z			
											...

TABLE A.1: Stationlist (Continuation)

Station no.	station name	type of station	Lat [°N]	Lon [°E]	Elevation [m]	Offset [km]	sample rate [ms /sps]	picked channel [Z / Hy-dro]	picked Offset to N [km]	to S [km]	comments
T180		t3052	38.4478	33.2013	933.0	-	-	-			
T181		EDL + 3ch (e3086)	38.4762	33.2129	936.3	36.0	10 / 100	Z			
T182		EDL + 3ch (e3139)	38.4928	33.2075	935.0	34.2	10 / 100	Z			
T183		CUBE + 1ch (c0052)	38.5067	33.1998	936.0	32.7	10 / 100	Z			
T184		EDL + 3ch (e3076)	38.5173	33.2082	928.5	31.5	10 / 100	Z			
T185		CUBE + 1ch (c0042)	38.5339	33.2067	918.0	29.6	10 / 100	Z			
T187		CUBE + 1ch (c0048)	38.5631	33.2117	914.0	26.4	10 / 100	Z			
T188		CUBE + 1ch (c0046)	38.5788	33.1878	919.0	24.9	10 / 100	Z			
T189		CUBE + 1ch (c0009)	38.5908	33.1826	911.0	23.6	10 / 100	Z			
T190		EDL + 3ch (e3114)	38.6064	33.1685	907.8	22.0	10 / 100	Z			
T191		CUBE + 1ch (c0061)	38.6177	33.1523	914.0	20.9	10 / 100	Z			
T192		CUBE + 1ch (c0043)	38.6317	33.1426	918.0	19.4	10 / 100	Z			
T193		EDL + 3ch (e3087)	38.6458	33.1365	915.0	17.9	10 / 100	Z			
T194		CUBE + 1ch (c0060)	38.6596	33.1275	913.0	16.5	10 / 100	Z			
T195		CUBE + 1ch (c0023)	38.6740	33.1209	919.0	14.9	10 / 100	Z			
T196		CUBE + 1ch (c0044)	38.6877	33.1150	915.0	13.5	10 / 100	Z			
T256		CUBE + 1ch ()	36.7631	32.9040	1591.9	227.8	10 / 100	Z			
T2001		SOUTHERN SHOT ON TURKEY	36.1878	32.9163	190.0	291.2			200	170 (Cyprus)	
T2002		NORTHERN SHOT ON TURKEY	38.4466	33.2017	950.0	39.3			NE (30)	SE (270)	

TABLE A.1: Station list

Appendix B

Legend of Geological Map of Cyprus

Geological map of Cyprus is shown in Fig. [4.4](#).

Mamonia Terrane

- metavolcanics, metacherts & marbles, Ayia Varvara Form., U. Cretaceous
- sediments, Ayios Photios Group, M. Triassic – M. Cretaceous
- sediments & volcanics, Dhiarizos Group, M. Triassic – M. Cretaceous

Kyrenia Terrane

- sediments, Kythrea Form., M. Miocene
- sediments, Lapithos Form., U. Cretaceous – Eocene
- sediments & rhyolites, Lapithos Form., U. Cretaceous – Eocene
- limestones, Hilarion Form., Jurassic – L. Cretaceous
- dolomitic limestones, Sykhari Form., U. Triassic
- marbles & phyllites, Dhikomo Form., L. – M. Triassic

Circum Troodos Sedimentary Succession

- alluvium–colluvium, Holocene
- terrace deposits, Pleistocene
- fanglomerate, Pleistocene
- sediments, Apalos–Athalassa Kakkaristra Form., Pleistocene
- sediments, Nicosia Form., Pliocene
- gypsum, marls & chalks, Kalavastos Form., U. Miocene
- limestones, Koronia member, Pakhna Form., Miocene
- chalks & marls, Pakhna Form., Miocene
- chalks, marls & cherts, Lefkara Form., Palaeocene – Oligocene
- debrites, Kathikas Form., U. Cretaceous
- melange, Moni Form., U. Cretaceous
- clays & sandstones, Kannaviou Form., U. Cretaceous

Troodos Terrane (Ophiolite) – Olympos (Axis) Sequence – U. Cretaceous

- umbers, shales & mudstones, Perapedhi Form.
- upper pillow lavas
- lower pillow lavas
- basal volcanic group
- sheeted dykes (diabase)
- plagiogranite
- gabbro
- pyroxenite
- wehrlite
- dunite
- harzburgite
- serpentinite

Troodos Terrane (Ophiolite) – Arakapas (Transform) Sequence

- pillow breccia
- volcanogenic sediments – sandstones, grits & silts
- volcanogenic sediments – breccias
- pillow lavas, hyaloclastites & sheet lava flows & dykes
- vitrophyric pillow lavas
- gabbros & norites
- (plagioclase) wehrlites

Faults

- ▲▲ Thrust fault
- Fault (unspecified type)
- - Inferred fault

Bibliography

- Adiyaman, Ö. and Chorowicz, J. (2002). Late cenozoic tectonics and volcanism in the northwestern corner of the arabian plate: a consequence of the strike-slip dead sea fault zone and the lateral escape of anatolia. *Journal of Volcanology and geothermal Research*, 117(3):327–345.
- Aksu, A., Calon, T., Hall, J., Mansfield, S., and Yaşar, D. (2005). The cilicia–adana basin complex, eastern mediterranean: Neogene evolution of an active fore-arc basin in an obliquely convergent margin. *Marine Geology*, 221(1):121–159.
- Anderson, D. L. and Dziewonski, A. M. (1984). Seismic tomography. *Scientific American*, 251:60–68.
- Angelier, J., Lyberis, N., Le Pichon, X., Barrier, E., and Huchon, P. (1982). The tectonic development of the hellenic arc and the sea of crete: a synthesis. *Tectonophysics*, 86(1):159–196.
- Ates, A., Tufan, S., et al. (1999). New gravity and magnetic anomaly maps of turkey. *Geophysical Journal International*, 136(2):499–502.
- Aydemir, A. (2009). Tectonic investigation of central anatolia, turkey, using geophysical data. *Journal of Applied Geophysics*, 68(3):321–334.
- Aydemir, A. and Ateş, A. (2005). Preliminary evaluation of central anatolian basins in turkey by using the gravity & magnetic data. *Journal of the Balkan Geophysical Society*, 8(1):7–19.
- Aydemir, A. and Ates, A. (2006a). Interpretation of suluklu-cihanbeyli-goloren magnetic anomaly, central anatolia, turkey: an integration of geophysical data. *Physics of the Earth and Planetary Interiors*, 159(3):167–182.

- Aydemir, A. and Ates, A. (2006b). Structural interpretation of the tuzgolu and haymana basins, central anatolia, turkey, using seismic, gravity and aeromagnetic data. *Earth Planets and Space*, 58(8):951.
- Barka, A. and Reilinger, R. (1997). Active tectonics of the eastern mediterranean region: deduced from gps, neotectonic and seismicity data. *Annali di Geofisica*, 11(3).
- Barton, P. (1986). The relationship between seismic velocity and density in the continental crust - a useful constraint? *Geophysical Journal International*, 87(1):195–208.
- Bates, R. L., Jackson, J. A., et al. (1984). *Dictionary of geological terms*, volume 584. Random House LLC.
- Bauer, K., Ryberg, T., Fuis, G. S., and Lüth, S. (2013). Seismic imaging of the waltham canyon fault, california: Comparison of ray-theoretical and fresnel volume prestack depth migration. *Bulletin of the Seismological Society of America*, 103(1):340–352.
- Ben-Avraham, Z. and Ginzburg, A. (1990). Displaced terranes and crustal evolution of the levant and the eastern mediterranean. *Tectonics*, 9(4):613–622.
- Ben-Avraham, Z., Ginzburg, A., Makris, J., and Eppelbaum, L. (2002). Crustal structure of the levant basin, eastern mediterranean. *Tectonophysics*, 346:23 – 43. <ce:title>Tectonics of Sedimentary Basins: from Crustal Structure to Basin Fill</ce:title>.
- Ben-Avraham, Z., Kempler, D., and Ginzburg, A. (1988). Plate convergence in the cyprean arc. *Tectonophysics*, 146:231 – 240. <ce:title>The Origin and Evolution of Arcs </ce:title>.
- Ben-Avraham, Z., Shoham, Y., and Ginzburg, A. (1976). Magnetic anomalies in the eastern mediterranean and the tectonic setting of the eratosthenes seamount. *Geophysical Journal International*, 45(1):105–123.
- Berk Biryol, C., Beck, S. L., Zandt, G., and Ozacar, A. A. (2011). Segmented african lithosphere beneath the anatolian region inferred from teleseismic p-wave tomography. *Geophysical Journal International*.
- Birch, F. (1961). The velocity of compressional waves in rocks to 10 kilobars: 2. *Journal of Geophysical Research*, 66(7):2199–2224.

- Birch, F. (1964). Density and composition of mantle and core. *Journal of geophysical research*, 69(20):4377–4388.
- Birch, F. (1966). Section 7: Compressibility; elastic constants. *Geological Society of America Memoirs*, 97:97–174.
- Blome, C. D. and Irwin, W. P. (1985). Equivalent radiolarian ages from ophiolitic terranes of cyprus and oman. *Geology*, 13(6):401–404.
- Bourbié, T., Coussy, O., and Zinszner, B. (1987). Acoustics of porous media: Editions technip. *Paris, France*.
- Buske, S., Gutjahr, S., and Sick, C. (2009). Fresnel volume migration of single-component seismic data. *Geophysics*, 74(6):WCA47–WCA55.
- Cadet, J.-P., Kobayashi, K., Aubouin, J., Boulègue, J., Deplus, C., Dubois, J., von Huene, R., Jolivet, L., Kanazawa, T., Kasahara, J., et al. (1987). The japan trench and its juncture with the kuril trench: cruise results of the kaiko project, leg 3. *Earth and Planetary Science Letters*, 83(1):267–284.
- Cady, J. W. (1980). Calculation of gravity and magnetic anomalies of finite-length right polygonal prisms. *Geophysics*, 45(10):1507–1512.
- Çakır, Ö. and Erduran, M. (2011). On the p and s receiver functions used for inverting the one-dimensional upper mantle shear-wave velocities. *Surveys in geophysics*, 32(1):71–98.
- Červený, V., Molotkov, I. A., Molotkov, I. A., and Pšenčík, I. (1977). *Ray method in seismology*. Univerzita Karlova.
- Cervený, V. and Psencik, I. (1981). Program seis81: 2-dimensional ray package. *Res. Rep., Int. Geophysics. Charles University, Prague*.
- Christensen, N. I. (1966). Elasticity of ultrabasic rocks. *Journal of Geophysical Research*, 71(24):5921–5931.
- Christensen, N. I. and Mooney, W. D. (1995). Seismic velocity structure and composition of the continental crust: A global view. *Journal of Geophysical Research: Solid Earth*, 100(B6):9761–9788.

- Clark, M. and Robertson, A. (2002). The role of the early tertiary ulukisla basin, southern turkey, in suturing of the mesozoic tethys ocean. *Journal of the Geological Society*, 159(6):673–690.
- Clube, T. and Robertson, A. (1986). The palaeorotation of the troodos microplate, cyprus, in the late mesozoic-early cenozoic plate tectonic framework of the eastern mediterranean. *Surveys in Geophysics*, 8(4):375–437.
- Coleman, R. (1971). Plate tectonic emplacement of upper mantle peridotites along continental edges. *Journal of Geophysical Research*, 76(5):1212–1222.
- Cosentino, D., Schildgen, T. F., Cipollari, P., Faranda, C., Gliozzi, E., Hudáčková, N., Lucifora, S., and Strecker, M. R. (2012). Late miocene surface uplift of the southern margin of the central anatolian plateau, central taurides, turkey. *Geological Society of America Bulletin*, 124(1-2):133–145.
- De Ridder, N. (1965). Sediments of the konya basin, central anatolia, turkey. *Palaeogeography, Palaeoclimatology, Palaeoecology*, 1:225–254.
- Di Luccio, F. and Pasyanos, M. E. (2007). Crustal and upper-mantle structure in the eastern mediterranean from the analysis of surface wave dispersion curves. *Geophysical Journal International*, 169(3):1139–1152.
- Dilek, Y. and Altunkaynak, Ş. (2009). Geochemical and temporal evolution of cenozoic magmatism in western turkey: mantle response to collision, slab break-off, and lithospheric tearing in an orogenic belt. *Geological Society, London, Special Publications*, 311(1):213–233.
- Dilek, Y. and Moores, E. (1987). Regional tectonics of the eastern mediterranean ophiolites. In *Ophiolites, oceanic crustal analogues, proceedings of the symposium Troodos*, volume 1990, pages 295–309.
- Dilek, Y. and Sandvol, E. (2009). Seismic structure, crustal architecture and tectonic evolution of the anatolian-african plate boundary and the cenozoic orogenic belts in the eastern mediterranean region. *Geological Society, London, Special Publications*, 327(1):127–160.
- Dupont, J. (1985). Effect of subduction of the louisville ridge on the structure and morphology of the tonga arc.

- Dziewonski, A. M. and Anderson, D. L. (1984). Seismic tomography of the earth's interior: The first three-dimensional models of the earth's structure promise to answer some basic questions of geodynamics and signify a revolution in earth science. *American Scientist*, 72(5):483–494.
- Eaton, S. and Robertson, A. (1993). The miocene pakhna formation, southern cyprus and its relationship to the neogene tectonic evolution of the eastern mediterranean. *Sedimentary Geology*, 86(3):273–296.
- Ediger, V., Evans, G., and Ergin, M. (1997). Recent surficial shelf sediments of the cilician basin (turkey), northeastern mediterranean. *Continental Shelf Research*, 17(13):1659–1677.
- Emeis, K., Robertson, A., Richter, C., et al. (1996). Proceedings of the ocean drilling program, initial reports. 160.
- Emeis, K.-C., Sakamoto, T., Wehausen, R., and Brumsack, H.-J. (2000). The sapropel record of the eastern mediterranean sea - results of ocean drilling program leg 160. *Palaeogeography, Palaeoclimatology, Palaeoecology*, 158(3):371–395.
- Ergün, M., Okay, S., Sari, C., Oral, E. Z., Ash, M., Hall, J., and Miller, H. (2005). Gravity anomalies of the cyprus arc and their tectonic implications. *Marine Geology*, 221:349 – 358. <ce:title>Miocene to Recent tectonic evolution of the Eastern Mediterranean</ce:title>.
- Fernandez-Blanco, D., Bertotti, G., and Ciner, T. A. (2013). Cenozoic tectonics of the tuz gölü basin (central anatolian plateau, turkey). *Turkish Journal of Earth Sciences*, 22(5).
- Finetti, I. and Morelli, C. (1973). *Geophysical exploration of the Mediterranean Sea*. Osservatorio geofisico sperimentale.
- Fryer, G. J. (1980). A slowness approach to the reflectivity method of seismogram synthesis. *Geophysical Journal International*, 63(3):747–758.
- Fryer, P. and Smoot, N. C. (1985). Processes of seamount subduction in the mariana and izu-bonin trenches. *Marine Geology*, 64(1):77–90.
- Fuchs, K. (1968). The reflection of spherical waves from transition zones with arbitrary depth-dependent elastic moduli and density. *Journal of Physics of the Earth*, 16:27–41.

- Fuchs, K. and Müller, G. (1971). Computation of synthetic seismograms with the reflectivity method and comparison with observations. *Geophysical Journal International*, 23(4):417–433.
- Gans, C. R., Beck, S. L., Zandt, G., Biryol, C. B., and Ozacar, A. A. (2009). Detecting the limit of slab break-off in central turkey: new high-resolution pn tomography results. *Geophysical Journal International*, 179(3):1566–1572.
- Gardosh, M. A. and Druckman, Y. (2006). Seismic stratigraphy, structure and tectonic evolution of the levantine basin, offshore israel. *Geological Society, London, Special Publications*, 260(1):201–227.
- Garfunkel, Z. (1981). Internal structure of the dead sea leaky transform (rift) in relation to plate kinematics. *Tectonophysics*, 80(1):81–108.
- Garfunkel, Z. (1998). Constrains on the origin and history of the eastern mediterranean basin. *Tectonophysics*, 298(1):5–35.
- Garfunkel, Z. (2004). Origin of the eastern mediterranean basin: a reevaluation. *Tectonophysics*, 391(1):11–34.
- Garfunkel, Z. and Derin, B. (1984). Permian-early mesozoic tectonism and continental margin formation in israel and its implications for the history of the eastern mediterranean. *Geological Society, London, Special Publications*, 17(1):187–201.
- Gass, I. G. and Masson-Smith, D. (1963). The geology and gravity anomalies of the troodos massif, cyprus. *Philosophical Transactions for the Royal Society of London. Series A, Mathematical and Physical Sciences*, pages 417–467.
- Geological Survey Department, C. (1995). Geological map of cyprus.
- Ghose, N. C., Nilanjan, C., and Fareeduddin (2014). *A Petrographic Atlas of Ophiolite: An example from the eastern India-Asia collision zone*. Springer India.
- Giermann, G. (1969). The eastern mediterranean ridge. *Rapp. Comm. Int. Mer Medit*, 19:605–607.
- Gökten, E. (1993). Geology of the southern boundary of the sivas basin in the east of ulaş (sivas–central anatolia): Tectonic development related to the closure of inner tauride ocean. *Turk. Assoc. Pet. Geol. Bull*, 5(1):35–55.

- Göncüoğlu, M. C., Dirik, K., and Kozlu, H. (1997). General characteristics of pre-alpine and alpine terranes in turkey: explanatory notes to the terrane map of turkey. In *Annales Geologique de Pays Hellenique*, volume 37, pages 515–536.
- Görür, N., Tüysüz, O., and Celal Şengör, A. (1998). Tectonic evolution of the central anatolian basins. *International Geology Review*, 40(9):831–850.
- Graf, D. F. (2010). *The Oxford Encyclopedia of Ancient Greece and Rome*, volume 1. Oxford University Press.
- Gürbüz, C. and Evans, J. (1991). A seismic refraction study of the western tuz gölü basin, central turkey. *Geophysical journal international*, 106(1):239–251.
- Hacker, B. R. and Abers, G. A. (2004). Subduction factory 3: An excel worksheet and macro for calculating the densities, seismic wave speeds, and h₂o contents of minerals and rocks at pressure and temperature. *Geochemistry, Geophysics, Geosystems*, 5(1).
- Hacker, B. R., Abers, G. A., and Peacock, S. M. (2003). Subduction factory 1. theoretical mineralogy, densities, seismic wave speeds, and h₂o contents. *Journal of Geophysical Research: Solid Earth (1978–2012)*, 108(B1).
- Harrison, R., Newell, W., Batıhanlı, H., Panayides, I., McGeehin, J., Mahan, S., Özhür, A., Tsiolakis, E., and Necdet, M. (2004). Tectonic framework and late cenozoic tectonic history of the northern part of cyprus: implications for earthquake hazards and regional tectonics. *Journal of Asian Earth Sciences*, 23(2):191–210.
- Hübscher, C. (2012). Maria s. merian-berichte eratosthenes seamount / eastern mediterranean sea cruise no. msm14/3. Technical report, DFG-Senatskommission für Ozeanographie / MARUM - Zentrum für Marine Umweltwissenschaften der Universität Bremen.
- Hobro, J. W., Singh, S. C., and Minshull, T. A. (2003). Three-dimensional tomographic inversion of combined reflection and refraction seismic travelttime data. *Geophysical Journal International*, 152(1):79–93.
- Hole, J., Clowes, R., and Ellis, R. (1992). Interface inversion using broadside seismic refraction data and three-dimensional travel time calculations. *Journal of Geophysical Research: Solid Earth (1978–2012)*, 97(B3):3417–3429.

- Hole, J. and Zelt, B. (1995). 3-d finite-difference reflection traveltimes. *Geophysical Journal International*, 121(2):427–434.
- Hsü, K. J. (1978). Tectonic evolution of the mediterranean basins. In *The ocean basins and margins*, pages 29–75. Springer.
- Improta, L., Zollo, A., Herrero, A., Frattini, R., Virieux, J., and Dell'Aversana, P. (2002). Seismic imaging of complex structures by non-linear traveltime inversion of dense wide-angle data: application to a thrust belt. *Geophysical Journal International*, 151(1):264–278.
- Jowitt, S. (2007). The geology of cyprus.
- Kadioglu, Y. K. and Dilek, Y. (2010). Structure and geochemistry of the adakitic horoz granitoid, bolkar mountains, south-central turkey, and its tectonomagmatic evolution. *International Geology Review*, 52(4-6):505–535.
- Kadioglu, Y. K., Dilek, Y., and Foland, K. A. (2006). Slab break-off and syncollisional origin of the late cretaceous magmatism in the central anatolian crystalline complex, turkey. *SPECIAL PAPERS-GEOLOGICAL SOCIETY OF AMERICA*, 409:381.
- Kalyoncuoğlu, Ü. Y., Elitok, Ö., Dolmaz, M. N., and Anadolu, N. C. (2011). Geophysical and geological imprints of southern neotethyan subduction between cyprus and the isparta angle, sw turkey. *Journal of Geodynamics*, 52(1):70–82.
- Kelly, K., Ward, R., Treitel, S., and Alford, R. (1976). Synthetic seismograms: a finite-difference approach. *Geophysics*, 41(1):2–27.
- Kempler, D. (1994). *Tectonic patterns in the Eastern Mediterranean*. PhD thesis, Hebrew Univ., Jerusalem.
- Kempler, D. (1998). 53. eratosthenes seamount: The possible spearhead of incipient continental collision in the eastern mediterranean1. *Proceedings of the Ocean Drilling Program, Scientific Results*, 160.
- Kempler, D. and Ben-Avraham, Z. (1987). The tectonic evolution of the cyprean arc. In *Annales Tectonicae*, volume 1, pages 58–71.
- Kennett, B. (1974). Reflections, rays, and reverberations. *Bulletin of the Seismological Society of America*, 64(6):1685–1696.

- Kennett, B. (1979). Theoretical reflection seismograms for elastic media. *Geophysical Prospecting*, 27(2):301–321.
- Kennett, B. (1980). Seismic waves in a stratified half space—ii. theoretical seismograms. *Geophysical Journal International*, 61(1):1–10.
- Kennett, B. (1983). Seismic wave propagation in stratified media. *Cambridge University Press*.
- Khair, K. and Tsokas, G. N. (1999). Nature of the levantine (eastern mediterranean) crust from multiple-source werner deconvolution of bouguer gravity anomalies. *Journal of Geophysical Research: Solid Earth (1978–2012)*, 104(B11):25469–25478.
- Kind, R. (1976). Computation of reflection coefficients for layered media. *JOURNAL OF GEOPHYSICS-ZEITSCHRIFT FUR GEOPHYSIK*, 42(3):191–200.
- Kissel, C., Laj, C., Poisson, A., and Görür, N. (2003). Paleomagnetic reconstruction of the cenozoic evolution of the eastern mediterranean. *Tectonophysics*, 362(1):199–217.
- Koketsu, K. et al. (2000). Finite difference travelttime calculation for head waves travelling along an irregular interface. *Geophysical Journal International*, 143(3):729–734.
- Koulakov, I. and Sobolev, S. V. (2006). Moho depth and three-dimensional p and s structure of the crust and uppermost mantle in the eastern mediterranean and middle east derived from tomographic inversion of local isc data. *Geophysical Journal International*, 164(1):218–235.
- Krashennnikov, V. A. (1994). *Geological structure of the Northeastern Mediterranean:(Cruise 5 of the Research Vessel Akademik Nikolaj Strakhov)*. Historical Productions-Hall Ltd.
- Krawczyk, C. M., Mechie, J., Lüth, S., Tašárová, Z., Wigger, P., Stiller, M., Brasse, H., Echtler, H. P., Araneda, M., and Bataille, K. (2006). Geophysical signatures and active tectonics at the south-central chilean margin. In *The Andes*, pages 171–192. Springer.
- Lallemand, S., Heuret, A., and Boutelier, D. (2005). On the relationships between slab dip, back-arc stress, upper plate absolute motion, and crustal nature in subduction zones. *Geochemistry, Geophysics, Geosystems*, 6(9):n/a–n/a.

- Laub, C. and Kuhl, T. L. (2004). How bad is good? a critical look at the fitting of reflectivity models using the reduced chi-square statistic.
- Lay, T. and Wallace, T. C. (1995). *Modern global seismology*, volume 58. Academic press.
- Lee, W. and Pereyra, V. (1993). Mathematical introduction to seismic tomography. *Seismic tomography: theory and practice*, pages 9–22.
- Levander, A., Zelt, C., and Symes, W. (2010). Crust and lithospheric structure – active source studies of crust and lithospheric structure. In Romanowicz, B. and Dziewonski, A., editors, *Seismology and Structure of the Earth: Treatise on Geophysics*, volume 1, chapter 1.08, pages 247–288. Elsevier.
- Limonov, A., Woodside, J., and Ivanov, M. (1994). *Mud Volcanism in the Mediterranean and Black Seas and Shallow Structure of the Eratosthenes Seamount: Initial Results of the Geological and Geophysical Investigations During the Third UNESCO-ESF "Training-through-Research" Cruise of RV Gelendzhik (June-July 1993)*. Unesco.
- Ludwig, W. J., Nafe, J. E., and Drake, C. L. (1970). Seismic refraction. *The sea*, 4(Part 1):53–84.
- Mackenzie, G. D., Maguire, P. K. H., Coogan, L. A., Khan, M. A., Eaton, M., and Petrides, G. (2006). Geophysical constraints on the crustal architecture of the troodos ophiolite: results from the iangass project. *Geophysical Journal International*, 167(3):1385–1401.
- Makris, J. (1976). A dynamic model of the hellenic arc deduced from geophysical data. *Tectonophysics*, 36(4):339–346.
- Makris, J., Abraham, Z. B., Behle, A., Ginzburg, A., Giese, P., Steinmetz, L., Whitmarsh, R. B., and Eleftheriou, S. (1983). Seismic refraction profiles between cyprus and israel and their interpretation. *Geophysical Journal of the Royal Astronomical Society*, 75(3):575–591.
- Makris, J. and Stobbe, C. (1984). Physical properties and state of the crust and upper mantle of the eastern mediterranean sea deduced from geophysical data. *Marine Geology*, 55:347 – 363. *Geological and Geodynamical Aspects on the Mediterranean*.

- Makris, J. and Wang, J. (1994). Bouguer gravity anomalies of the eastern mediterranean sea. *Geological structure of the Northeastern Mediterranean. Jerusalem*, pages 87–98.
- Makropoulos, K. C. and Burton, P. W. (1984). Greek tectonics and seismicity. *Tectonophysics*, 106(3):275–304.
- Mallick, S. and Frazer, L. N. (1987). Practical aspects of reflectivity modeling. *Geophysics*, 52(10):1355–1364.
- Malpas, J. (1990). Crustal accretionary processes in the troodos ophiolite, cyprus: Evidence from field mapping and deep crustal drilling. *Ophiolites, oceanic crustal analogues. Geol Surv Dept, Nicosia, Cyprus*, pages 65–74.
- Marco, S. (2009). Introduction - the dead sea fault. *Field guide of The Department of Geophysics and Planetary Sciences, Tel Aviv University*.
- Marone, F., Van Der Meijde, M., Van Der Lee, S., and Giardini, D. (2003). Joint inversion of local, regional and teleseismic data for crustal thickness in the eurasia–africa plate boundary region. *Geophysical Journal International*, 154(2):499–514.
- Mascle, J., Benkhelil, J., Bellaiche, G., Zitter, T., Woodside, J., and Loncke, L. (2000). Marine geologic evidence for a levantine-sinai plate, a new piece of the mediterranean puzzle. *Geology*, 28(9):779–782.
- Mavko, G., Mukerji, T., and Dvorkin, J. (2009). *The rock physics handbook: Tools for seismic analysis of porous media*. Cambridge University Press.
- McCallum, J. and Robertson, A. (1990). Pulsed uplift of the troodos massif—evidence from the plio-pleistocene mesaoria basin. *Troodos '87, ophiolite and oceanic lithosphere. Cyprus Geological Survey Department*, pages 217–230.
- McClusky, S., Balassanian, S., Barka, A., Demir, C., Ergintav, S., Georgiev, I., Gurkan, O., Hamburger, M., Hurst, K., Kahle, H., et al. (2000). Global positioning system constraints on plate kinematics and dynamics in the eastern mediterranean and caucasus. *Journal of Geophysical Research*, 105(B3):5695–5719.
- McClusky, S., Reilinger, R., Mahmoud, S., Ben Sari, D., and Tealeb, A. (2003). Gps constraints on africa (nubia) and arabia plate motions. *Geophysical Journal International*, 155(1):126–138.

- McKenzie, D. (1972). Active tectonics of the mediterranean region. *Geophysical Journal of the Royal Astronomical Society*, 30(2):109–185.
- Mechie, J., Abu-Ayyash, K., Ben-Avraham, Z., El-Kelani, R., Qabbani, I., and Weber, M. (2009). Crustal structure of the southern dead sea basin derived from project desire wide-angle seismic data. *Geophysical Journal International*, 178(1):457–478.
- Meier, T., Dietrich, K., Stöckhert, B., and Harjes, H.-P. (2004). One-dimensional models of shear wave velocity for the eastern mediterranean obtained from the inversion of rayleigh wave phase velocities and tectonic implications. *Geophysical Journal International*, 156(1):45–58.
- Müller, G. (1985). The reflectivity method-a tutorial. *Journal of Geophysics*, 58(1-3):153–174.
- Montadert, L., Letouzey, J., and Mauffret, A. (1978). Messinian event: seismic evidence. *Initial reports of the deep sea drilling project*, 42(Part 1):1037–1050.
- Mutlu, A. K. and Karabulut, H. (2011). Anisotropic pn tomography of turkey and adjacent regions. *Geophysical Journal International*, 187(3):1743–1758.
- Nafe, J. E. and Drake, C. L. (1957). Variation with depth in shallow and deep water marine sediments of porosity, density and the velocities of compressional and shear waves. *Geophysics*, 22(3):523–552.
- Netzeband, G., Gohl, K., Hübscher, C., Ben-Avraham, Z., Dehghani, G., Gajewski, D., and Liersch, P. (2006). The levantine basin - crustal structure and origin. *Tectonophysics*, 418(3):167–188.
- Nowack, R. and Braile, L. (1993). Refraction and wide-angle reflection tomography: theory and results. *Seismic Tomography: Theory and Practice*, pages 733–763.
- Okay, A. I. (1984). Distribution and characteristics of the north-west turkish blueschists. *Geological Society, London, Special Publications*, 17(1):455–466.
- Okay, A. İ. (2000). Was the late triassic orogeny in turkey caused by the collision of an oceanic plateau? *Geological Society, London, Special Publications*, 173(1):25–41.
- Okay, A. I. (2008). Geology of turkey: a synopsis. *Anschnitt*, 21:19–42.

- Okay, A. I. and Tüysüz, O. (1999). Tethyan sutures of northern turkey. *Geological Society, London, Special Publications*, 156(1):475–515.
- Ozel, E., Ulug, A., and Pekcetinoz, B. (2007). Neotectonic aspects of the northern margin of the adana-cilicia submarine basin, ne mediterranean. *Journal of Earth System Science*, 116(2):113–124.
- Papazachos, B. C. and Papaioannou, C. A. (1999). Lithospheric boundaries and plate motions in the cyprus area. *Tectonophysics*, 308(1):193–204.
- Parkes, G. and Hatton, L. (1986). *The marine seismic source*, volume 4. Springer.
- Pichon, X. L. and Angelier, J. (1979). The hellenic arc and trench system: a key to the neotectonic evolution of the eastern mediterranean area. *Tectonophysics*, 60(1):1–42.
- Pilidou, S., Priestley, K., Jackson, J., and Maggi, A. (2004). The 1996 cyprus earthquake: a large, deep event in the cyprean arc. *Geophysical Journal International*, 158(1):85–97.
- Piper, J., Gürsoy, H., Tatar, O., Beck, M., Rao, A., Koçbulut, F., and Mesci, B. (2010). Distributed neotectonic deformation in the anatolides of turkey: A palaeomagnetic analysis. *Tectonophysics*, 488(1):31–50.
- Podvin, P. and Lecomte, I. (1991). Finite difference computation of traveltimes in very contrasted velocity models: a massively parallel approach and its associated tools. *Geophysical Journal International*, 105(1):271–284.
- Poole, A. and Robertson, A. (1991). Quaternary uplift and sea-level change at an active plate boundary, cyprus. *Journal of the Geological Society*, 148(5):909–921.
- Pourteau, A., Candan, O., and Oberhänsli, R. (2010). High-pressure metasediments in central turkey: Constraints on the neotethyan closure history. *Tectonics*, 29(5).
- Pratt, R., Song, Z.-M., Williamson, P., and Warner, M. (1996). Two-dimensional velocity models from wide-angle seismic data by wavefield inversion. *Geophysical Journal International*, 124(2):323–340.
- Ravaut, C., Operto, S., Improta, L., Virieux, J., Herrero, A., and Dell’Aversana, P. (2004). Multiscale imaging of complex structures from multifold wide-aperture seismic data by frequency-domain full-waveform tomography: application to a thrust belt. *Geophysical Journal International*, 159(3):1032–1056.

- Rawlinson, N. (2000). *Inversion of Seismic Data for Layered Crustal Structure*. PhD thesis, Monash University.
- Rawlinson, N., Pozgay, S., and Fishwick, S. (2010). Seismic tomography: A window into deep earth. *Physics of the Earth and Planetary Interiors*, 178(3):101–135.
- Rawlinson, N. and Sambridge, M. (2003). Seismic travelttime tomography of the crust and lithosphere. *Advances in Geophysics*, 46:81–198.
- Reilinger, R., McClusky, S., Vernant, P., Lawrence, S., Ergintav, S., Cakmak, R., Ozener, H., Kadirov, F., Guliev, I., Stepanyan, R., Nadariya, M., Hahubia, G., Mahmoud, S., Sakr, K., ArRajehi, A., Paradissis, D., Al-Aydrus, A., Prilepin, M., Guseva, T., Evren, E., Dmitrotsa, A., Filikov, S. V., Gomez, F., Al-Ghazzi, R., and Karam, G. (2006). Gps constraints on continental deformation in the africa-arabia-eurasia continental collision zone and implications for the dynamics of plate interactions. *Journal of Geophysical Research: Solid Earth*, 111(B5):n/a–n/a.
- Roberts, N., Black, S., Boyer, P., Eastwood, W. J., Griffiths, H., Lamb, H., Leng, M., Parish, R., Reed, J., Twigg, D., et al. (1999). Chronology and stratigraphy of late quaternary sediments in the konya basin, turkey: results from the kopal project. *Quaternary Science Reviews*, 18(4):611–630.
- Robertson, A. (1977). Tertiary uplift history of the troodos massif, cyprus. *Geological Society of America Bulletin*, 88(12):1763–1772.
- Robertson, A. (1990). Tectonic evolution of cyprus. *Ophiolites and Oceanic Lithosphere*, pages 235–250.
- Robertson, A. and Comas, M. (1998). Collision-related processes in the mediterranean region - introduction. *Tectonophysics*, 298(1):1–4.
- Robertson, A., Eaton, S., Follows, E., and Payne, A. (1995a). Sedimentology and depositional processes of miocene evaporites from cyprus. *Terra Nova*, 7:233–254.
- Robertson, A., Kidd, R., Ivanov, M., Limonov, A., Woodside, J., Galindo-Zaldivar, J., and Nieto, L. (1995b). Eratosthenes seamount: collisional processes in the easternmost mediterranean in relation to the plio-quaternary uplift of southern cyprus. *Terra Nova*, 7(2):254–264.

- Robertson, A., Parlak, O., and Ünlügenç, U. C. (2013a). Editorial introduction to geological development of anatolia and the easternmost mediterranean region. *Geological Society, London, Special Publications*, 372(1):1–7.
- Robertson, A. and Woodcock, N. (1979). Tectonic setting of the troodos massif in the east mediterranean. In *Proceedings International Ophiolite Symposium. Cyprus, Cyprus Geological Survey Department*, pages 36–49.
- Robertson, A. H. (1998a). Mesozoic-tertiary tectonic evolution of the easternmost mediterranean area: integration of marine and land evidence. *Proceedings of the Ocean Drilling Program, Scientific Results, Vol. 160; Chapter 54*.
- Robertson, A. H. (1998b). Tectonic significance of the eratosthenes seamount: a continental fragment in the process of collision with a subduction zone in the eastern mediterranean (ocean drilling program leg 160). *Tectonophysics*, 298:63 – 82.
- Robertson, A. H. (2000). Mesozoic-tertiary tectonic-sedimentary evolution of a south tethyan oceanic basin and its margins in southern turkey. *Geological Society, London, Special Publications*, 173(1):97–138.
- Robertson, A. H. (2002). Overview of the genesis and emplacement of mesozoic ophiolites in the eastern mediterranean tethyan region. *Lithos*, 65(1):1–67.
- Robertson, A. H. and Dixon, J. (1984). Introduction: aspects of the geological evolution of the eastern mediterranean. *Geological Society, London, Special Publications*, 17(1):1–74.
- Robertson, A. H., Parlak, O., and Ustaömer, T. (2012). Overview of the palaeozoic–neogene evolution of neotethys in the eastern mediterranean region (southern turkey, cyprus, syria). *Petroleum Geoscience*, 18(4):381–404.
- Robertson, A. H., Parlak, O., and Ustaömer, T. (2013b). Late palaeozoic–early cenozoic tectonic development of southern turkey and the easternmost mediterranean region: evidence from the inter-relations of continental and oceanic units. *Geological Society, London, Special Publications*, 372(1):9–48.
- Ryberg, T., Tittgemeyer, M., and Wenzel, F. (2000). Finite difference modelling of p-wave scattering in the upper mantle. *Geophysical Journal International*, 141(3):787–800.

- Ryberg, T., Tittgemeyer, M., and Wenzel, F. (2006). Finite difference modelling of seismic wave phenomena with the earth's upper mantle. In *High Performance Computing in Science and Engineering '06*. Wolfgang Nagel and Willi Jäger.
- Salisbury, M., Christensen, N., Vine, F., Smith, G., and Eleftheriou, S. (1989). Geophysical structure of the Troodos ophiolite from downhole logging. *Cyprus crustal study project: initial report*, pages 331–349.
- Sandwell, D., Garcia, E., Soofi, K., Wessel, P., Chandler, M., and Smith, W. H. (2013). Toward 1-mgal accuracy in global marine gravity from Cryosat-2, Envisat, and Jason-1. *The Leading Edge*, 32(8):892–899.
- Sandwell, D. T. and Smith, W. H. (2009). Global marine gravity from retracked Geosat and ERS-1 altimetry: Ridge segmentation versus spreading rate. *Journal of Geophysical Research: Solid Earth (1978–2012)*, 114(B1).
- Schattner, U. (2010). What triggered the early-to-mid pleistocene tectonic transition across the entire eastern Mediterranean? *Earth and Planetary Science Letters*, 289:539–548.
- Schildgen, T., Cosentino, D., Bookhagen, B., Niedermann, S., Yildirim, C., Echtler, H., Wittmann, H., and Strecker, M. (2012a). Multi-phased uplift of the southern margin of the central Anatolian plateau, Turkey: A record of tectonic and upper mantle processes. *Earth and Planetary Science Letters*, 317:85–95.
- Schildgen, T., Cosentino, D., Caruso, A., Buchwaldt, R., Yildirim, C., Bowring, S., Roy, B., Echtler, H., and Strecker, M. (2012b). Surface expression of eastern Mediterranean slab dynamics: Neogene topographic and structural evolution of the southwest margin of the central Anatolian plateau, Turkey. *Tectonics*, 31(2):TC2005.
- Schildgen, T., Yildirim, C., Cosentino, D., and Strecker, M. (2014). Linking slab break-off, Hellenic trench retreat, and uplift of the central and eastern Anatolian plateaus. *Earth-Science Reviews*, 128:147–168.
- Schneider, W., Ranzinger, K. A., Balch, A., and Kruse, C. (1992). A dynamic programming approach to first arrival traveltime computation in media with arbitrarily distributed velocities. *Geophysics*, 57(1):39–50.

- Shelton, A. (1993). Troodos revisited: the mount olympus gravity anomaly. *Geological Society, London, Special Publications*, 76(1):197–212.
- Sheriff, R. E. (1975). Factors affecting seismic amplitudes. *Geophysical Prospecting*, 23(1):125–138.
- Sheriff, R. E. and Geldart, L. P. (1982). *Exploration seismology*, volume 1995. Cambridge university press Cambridge.
- Silantyev, S. A. and Portnyagin, M. V. (2005). The troodos ophiolite complex (structural para-autochthon). In Krasheninnikov, V. A. and Hall, J. K., editors, *GEOLOGICAL FRAMEWORK of the LEVANT*, volume 1. Historical Productions-Hall.
- Simm, R. and Bacon, M. (2014). *Seismic Amplitude: An Interpreter's Handbook*. Cambridge University Press.
- Sipkin, S. A., Person, W. J., and Presgrave, B. W. (2000). Earthquake bulletins and catalogs at the usgs national earthquake information center. *U.S. Geological Survey National Earthquake Information Center*.
- Smith, G. and Vine, F. (1989). The physical properties of diabases, gabbros and ultramafic rocks from ccsp drill hole cy-4 at palekhor, cyprus. *Cyprus Crustal Study Project: Initial report, holes CY*, 4:295–314.
- Sonnenfeld, P. and Finetti, I. (1985). Messinian evaporites in the mediterranean: a model of continuous inflow and outflow. In *Geological evolution of the Mediterranean Basin*, pages 347–353. Springer.
- Stride, A. H., Belderson, R., and Kenyon, N. (1977). Evolving miogeanticlines of the east mediterranean (hellenic, calabrian and cyprus outer ridges). *Philosophical Transactions for the Royal Society of London. Series A, Mathematical and Physical Sciences*, pages 255–285.
- Talwani, M., Worzel, J. L., and Landisman, M. (1959). Rapid gravity computations for two-dimensional bodies with application to the mendocino submarine fracture zone. *Journal of Geophysical Research*, 64(1):49–59.
- Tarantola, A. (1984). Inversion of seismic reflection data in the acoustic approximation. *Geophysics*, 49(8):1259–1266.

- Telford, W., Geldart, L., and Sheriff, R. (1990). Applied geophysics, 1990. *Cambridge University Press*, 770p. doi, 10:0926–9851.
- Tezel, T., Shibutani, T., and Kaypak, B. (2013). Crustal thickness of turkey determined by receiver function. *Journal of Asian Earth Sciences*, 75:36–45.
- Tikhotsky, S. and Achauer, U. (2008). Inversion of controlled-source seismic tomography and gravity data with the self-adaptive wavelet parametrization of velocities and interfaces. *Geophysical Journal International*, 172(2):619–630.
- van Trier, J. and Symes, W. W. (1991). Upwind finite-difference calculation of travel-times. *Geophysics*, 56(6):812–821.
- Vanacore, E., Taymaz, T., and Saygin, E. (2013). Moho structure of the anatolian plate from receiver function analysis. *Geophysical Journal International*, 193(1):329–337.
- Vidale, J. (1988). Finite-difference calculation of travel times. *Bulletin of the Seismological Society of America*, 78(6):2062–2076.
- Vidale, J. E. (1990). Finite-difference calculation of traveltimes in three dimensions. *Geophysics*, 55(5):521–526.
- Wdowinski, S., Ben-Avraham, Z., Arvidsson, R., and Ekström, G. (2006). Seismotectonics of the cyprian arc. *Geophysical Journal International*, 164(1):176–181.
- West, I. (2013). Geology of the salt lake and coast of the akrotiri peninsula, cyprus. Version: 14th December 2013.
- White, D. (1989). Two-dimensional seismic refraction tomography. *Geophysical Journal International*, 97(2):223–245.
- Woodside, J. (1977). Tectonic elements and crust of the eastern mediterranean sea. *Marine Geophysical Researches*, 3(3):317–354.
- Yongwang Ma, Luiz Loures, G. F. M. (2004). Seismic modelling with the reflectivity method. *CREWES Research Report*, 16.
- Yoon, M., Buske, S., Lüth, S., Schulze, A., Shapiro, S., Stiller, M., and Wigger, P. (2003). Along-strike variations of crustal reflectivity related to the andean subduction process. *Geophysical research letters*, 30(4).

- Zak, I. and Freund, R. (1981). Asymmetry and basin migration in the dead sea rift. *Tectonophysics*, 80(1):27–38.
- Zelt, C. A. (1999). Modelling strategies and model assessment for wide-angle seismic traveltimes data. *Geophysical Journal International*, 139(1):183–204.
- Zelt, C. A. and Barton, P. J. (1998). Three-dimensional seismic refraction tomography: A comparison of two methods applied to data from the faeroe basin. *Journal of Geophysical Research: Solid Earth (1978–2012)*, 103(B4):7187–7210.
- Zelt, C. A., Sain, K., Naumenko, J. V., and Sawyer, D. S. (2003). Assessment of crustal velocity models using seismic refraction and reflection tomography. *Geophysical Journal International*, 153(3):609–626.
- Zelt, C. A. and Smith, R. B. (1992). Seismic traveltimes inversion for 2-d crustal velocity structure. *Geophysical Journal International*, 108(1):16–34.
- Zverev, S. (2010). *Blocks and faults of Earth crust on the Levant Basin: DSS results of ccruise of RAS r/v 'Akademik Boris Petrov' and 'Akademik Nikolai Strakhov'*. Institute of Physics of Earth RAS.-M: Svetoch Plus.
- Zverev, S. M. (2005). Peculiarities of sediments and basement structure in the frontal zone of the cyprean arc (based on seismic refraction data). *GEOLOGICAL FRAMEWORK OF THE LEVANT (VOL II), Historical Productions-Hall*, 2:113 – 126.
- Zverev, S. M. and Ilinsky, D. A. (2005). The deep structure of eratosthenes seamount from seismic refraction data. *GEOLOGICAL FRAMEWORK OF THE LEVANT (VOL II), Historical Productions-Hall*, 2:73–112.

Erklärung zur Dissertation

Name/Anschrift
Christian Feld
Königstr. 23
12105 Berlin

Ehrenwörtliche Erklärung zu meiner Dissertation mit dem Titel:

**Crustal structure of the Eratosthenes Seamount, Cyprus and
S. Turkey from an amphibian wide-angle seismic profile**

Sehr geehrte Damen und Herren,

hiermit erkläre ich, dass ich die beigelegte Dissertation selbstständig verfasst und keine anderen als die angegebenen Hilfsmittel genutzt habe. Alle wörtlich oder inhaltlich übernommenen Stellen habe ich als solche gekennzeichnet.

Ich versichere außerdem, dass ich die beigelegte Dissertation nur in diesem und keinem anderen Promotionsverfahren eingereicht habe.

Ort, Datum

Unterschrift